technische universität
dortmund

Nuclear-Electron Spin Interaction in Low-Dimensional Semiconductors

Dissertation

submitted in partial fulfillment of the requirements
for the degree of Dr. rer. nat.

Eiko Evers

Dortmund, December 2021
Department of Physics, TU Dortmund University

Accepted by the Department of Physics, TU Dortmund University, Germany.

Date of the oral examination: 6 December 2021

Examination Board:
PD Dr. Alex Greilich
Prof. Dr. Frithjof Anders
Dr. Christian Sternemann
Prof. Dr. Heinrich Päs

External Reviewer:
Prof. Dr. Tobias Korn (University of Rostock)

Abstract

The nuclear spins in semiconductors can serve as a quantum mechanical system with minutes long spin relaxation times, enhanced by the decoupling from the surrounding matter in strained nanostructures and the absence of interaction with light. In order to manipulate the nuclear spin system optically, resident electrons confined in the nanostructure are introduced as a mediator. The electron localization leads to an efficient coupling of the electron spin to the nuclear spins via Fermi contact hyperfine interaction. This allows one to polarize the nuclear spins and to detect their dynamics. In this work, the nuclear spin dynamics in a cadmium telluride (CdTe) quantum well is characterized, assisted by nuclear magnetic resonance radio frequency pulses. The independent dynamics of the isotope spins turns out to be harmonized. In the enhanced localization in negatively doped indium gallium arsenide (InGaAs) quantum dots, two nuclear spin polarization protocols are assessed. Firstly, the developed extended pump-probe setup allows to investigate the established nuclei-induced frequency focusing by tracing the electron spin precession with improved spectral resolution. Secondly, a novel technique based on the pulsed excitation with $1\,\mathrm{GHz}$ pulse repetition frequency is introduced, which allows to establish a substantial nuclear spin polarization in a transverse field while also reducing the fluctuations of the unordered nuclear spins.

Zusammenfassung

Die Kernspins in Halbleitern bilden durch die fehlende Wechselwirkung mit Licht ein quantenmechanisches System mit langen Spin-Relaxationszeiten, die durch die Entkopplung vom umgebenden Festkörper in verspannten Nanostrukturen noch verlängert werden. Residente Elektronen in der Nanostruktur erlauben es, die Polarisation des Lichts auf das Kernspinsystem zu übertragen und optisch zugänglich zu machen, weil die Elektronenlokalisierung für eine effiziente Kopplung des Elektronenspins mit den Kernspins über die Fermikontakt-Hyperfeinwechselwirkung sorgt. In dieser Arbeit wird zum einen die isotopenaufgelöste Kernspindynamik in einem Cadmiumtellurid-Quantentopf mit Hilfe von Kernspinresonanzpulsen charakterisiert und eine Angleichung der Dynamik der eigentlich unabhängigen Isotopenspins beobachtet. Für die stärkere Lokalisierung in negativ dotierten Indiumgalliumarsenid-Quantenpunkten werden zum anderen zwei Kernspinpolarisationsprotokolle untersucht. Erstens erlaubt die verbesserte Präzessionsfrequenzauflösung des im Umfeld der Arbeit entwickelten, erweiterten Pump-Probe-Aufbaus die detaillierte Untersuchung der bekannten kerninduzierten Frequenzfokussierung. Zweitens wird die optische Anregung mit einer Pulsfrequenz von 1 GHz beschrieben. Dadurch wird eine signifikante Kernspinpolarisation in einem transversalen Magnetfeld induziert und gleichzeitig die Fluktuation der ungeordneten Kernspins reduziert.

Contents

Contents

1 Motivation

Although the digital integration has evolved rapidly by necessity due to the Coronavirus pandemic, a major hurdle for a fully digital integration remains the lack of physically secure communication as information and identity can be stolen and altered unnoticed during their transmission. The exchange of quantum information, protected by the laws of quantum mechanics as quantum key distribution (QKD), would resolve these issues [BB84; Eke91] and requires the purely quantum connection of two quantum agents over a noisy channel [Sca09]. Each quantum agent is represented by interacting quantum states (a collection of qubits in a quantum computer) [Loo20], but the operation of such a device is challenging. While a classical system can be observed without a fundamental perturbation of the studied system, the interaction of a quantum system with a classical measurement system leads to the rapid but continuous focusing of the quantum superposition of states (qubits) to the classical system with discrete states (classical bits), called decoherence or loss of coherence [Zur03]. This interaction resembles the opening of the box in the Schrödinger's cat thought experiment [Sch35; Har98].

In recent years, the control over the interaction of a quantum system with the classical system has been improved and scaled to the point, that a quantum processor is claimed to outperform classical computers in certain tasks [Aru19]. Today, quantum computers simulate simple quantum systems [Heb17], solve traffic flow optimization tasks [Neu17], predict the luminescence of organic molecules [Gao21], and model a small system of interacting neutrinos [Hal21], among other applications. Consequently, the purely quantum connection of local quantum computation devices in a quantum internet [Kim08; Pro21] presents itself as the next step, with an optical transmission as preferred mode of connection [WEH18].

QKD over a large distance on noisy channels poses an inherent challenge. While it relies on the fact that a quantum state can not be cloned [WZ82], this also prohibits the use of a classical repeater scheme [DM10] – read an optical stream and replicate it. This asks for quantum repeaters which instead of amplifying signals initiate and mediate the entanglement of separated quantum agents [Bri98; Dua01]. The key criteria for a quantum repeater are therefore comprised of a high photon absorption and emission quantum efficiency, a satisfyingly large coherence time in order to keep the entanglement over the whole repeater chain, and a sufficiently high manipulation rate [San11; Loo20]. For that purpose, several physical platforms are currently discussed, such as vacancies in diamonds [Roz19; Ngu19], trapped ions [DM10; Cas15] and atoms [San11; Mor19], and rare-earth ions in silicates [Zho15] together with different operating schemes [GT07; Luo16; Loo20].

One of these platforms is the electron-nuclear spin system (ENSS) in a singly charged semiconductor quantum dot (QD), where the single electron is localized on 10^5 nuclei. Such a QD system offers a large light-matter interaction [Shi07] and, due to favorable optical selection rules, the spin state of a resident electron can be efficiently initialized with a single photon [YFI10]. This results in a high overall state preparation fidelity [Ata06]. Moreover, the operation rate of electron spins (ESs) in QDs is the highest among the presented alternatives [Loo20], but the coherence time of a single ES is in the orders of µs [Gre06b], significantly shorter than in the other mentioned systems [Loo20]. One major decoherence channel is given by the enhanced hyperfine interaction with randomly oriented nuclear spins (NSs) due to the electron localization [Urb13]. This strong localization, however, allows one to shape the nuclear spin system (NSS) either to a major NS orientation [Urb07] or to a collective NS state (magnon) with fixed phase relation between NSs [Éth17]. In the latter state, it has been shown that the ES orientation can be confidently transferred to the NSS by the flip of a single NS state and vice versa [Gan19]. This provides the ES coherent access to a local quantum memory with a lifetime of hours [Gre07], which can be used to elongate the coherence time from several ms [Wüs16] to hundreds of ms by using radio frequency (RF) protocols [Wae19] and renders the QD ENSS an even more prospective platform for a quantum repeaters.

With that in mind, this work focuses on the manipulation and characterization of the nuclear spin polarization (NSP) in semiconductor nanostructures, namely cadmium telluride (CdTe) quantum wells (QWs) and an ensemble of indium gallium arsenide (InGaAs) QDs, by dynamical nuclear polarization (DNP). While a detailed analysis of the ENSS in the ensemble of QDs needs to take into account the quadrupole interaction of NSs with strain induced electric field gradients and the size and composition inhomogeneity [Urb13], the ENSS of the QWs is rather homogeneous [Zhu07], barely strained [Waa93] and the NSs do not possess a quadrupole moment [Hay12]. The characterization of the NS dynamics by optically detected nuclear magnetic resonance (NMR), in the footsteps of similar investigations for gallium arsenide (GaAs) QWs by Sanada et al. [San06], therefore serves as an attractive model experiment. As a next step, the novel extended pump probe (EPP) technique is used to investigate the known nuclei-induced frequency focusing (NIFF) in an InGaAs QD ensemble [Gre07] with improved ES precession frequency resolution to determine the NSP achieved. Subsequently, it is found that the orientation of the ESs with a laser pulse repetition frequency (PRF) of 1 GHz induces a collective precession of ESs within the inhomogeneous ensemble, which alleviates the need for an extensive QD binning and an advanced optical setup for the investigation of a QD sample. The 1 GHz PRF also decreases the random nuclear spin fluctuation (NSF). Finally, a novel NS polarization protocol in transversal magnetic field is developed, which builds up to a NSP acting as Overhauser field (OF) on the electron spin polarization (ESP) multiple times larger than the required external field variation in a majority of inhomogeneous QDs simultaneously.

2 Physical Background

The optical investigation of the ENSS in semiconductor nanostructures requires to outline the interaction of the mediating electrons with light. To that end, based on the band structure and energy levels in bulk semiconductors in Sec. 2.1.1, the peculiarities of the energy states in nanostructures is elucidated in Sec. 2.1.2. Subsequently, the quantum mechanical spin, as an intrinsic angular momentum, is introduced in Sec. 2.2. In Sec. 2.2.1, the optical orientation of ESs beyond the thermal equilibrium is explained, which allows for the initialization of a defined spin-state with its dynamics detailed in Sec. 2.2.2. The NS is introduced is Sec. 2.3 and the defining ES-NS interaction for systems of localized electrons described in Sec. 2.4. The dephasing of the total ESP as an ensemble effect is detailed in Sec. 2.5. The illumination with a train of laser pulses leads to resonant spin amplification (RSA) and the in-phase precession of an ensemble of ESs on equally spaced modes causes ES mode locking as described in Sec. 2.5.1. This facilitates the polarization of NSs as displayed in Sec. 2.5.2.

2.1 Electron Energy Levels of Semiconductor Structures

The interaction of charge carriers with light is defined by the electron level structure of a semiconductor crystal and therefore poses the starting point for any optical manipulation. The following brief introduction to the energy band structures is based on Ref. [Kli07].

2.1.1 Band Structure of Bulk Semiconductor Crystals

The compound materials of the low-dimensional semiconductors studied in this work are fabricated off intrinsic semiconductor crystals in their bulk form: GaAs, indium arsenide (InAs), and CdTe. The large number of periodically ordered atoms leads to the emergence of energy bands out of the energy levels of the compound atoms. The kinetic energy of the electronic state on a band depends on their momentum and is described by the dispersion relation. For a free electron, the dispersion relation is given by $E \sim \mathbf{k}^2/m_e$ with the wave vector $\mathbf{k}$ and the electron mass m_e. The crystal structure and the lattice constant both influences the band position in energy and the dispersion relation of the band. All studied semiconductors crystallize in zinc blende structure, a highly symmetric crystal structure consisting of two face-centered

cubic (fcc) Bravais lattices. The structure of GaAs is given as an example on Fig. 2.1. It differs only in the size of the atomic radii as well as in the lattice parameter a from the other semiconductor crystals mentioned above[1].

Figure 2.1: GaAs crystal with constituent gallium (Ga) (red) and arsenic (As) (black) atoms and nearest neighbor bonds. The crystal consists of two face-centered cubic (fcc) unit cells, one for gallium (Ga) and one for arsenic (As) which is shifted by $(^1/_4, ^1/_4, ^1/_4)a$ relative to the Ga unit cell. a is the lattice parameter and equal for both unit cells. The visualization of the crystal structure is achieved using VESTA3 [MI11] based on the data provided in Ref. [Wyc63, pp. 108–110] as listed in the Crystallography Open Database [Gra09].
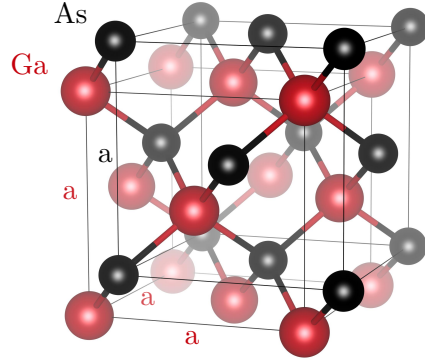
Due to the Pauli exclusion principle, the energy bands are filled with the electrons provided by the constituent atoms. The number of available electrons and the density of states in the crystal is therefore given by the constituent atoms and their ratio in the compound[2]. For a temperature of $T = 0\,\text{K}$, the available electrons define the Fermi energy E_F as the maximal energy up to which the bands are occupied in the ground state[3]. In intrinsic semiconductors, the Fermi energy is located in between two bands. The highest occupied band is the valence band (VB) and the lowest unoccupied band is denoted as conduction band (CB) separated by the band gap energy E_g (see Fig. 2.2).

The highest point of the VB does not need to require the same crystal momentum as the lowest point of the CB. If the momentum differs, the semiconductor is called an indirect semiconductor of which notable examples are germanium and silicon (Si). In an indirect semiconductor, the absorption and emission of light has to be assisted by a momentum transfer, typically enabled by changing the vibration state of the crystal lattice (phonon assisted), which lowers the optical transition probability. All semiconductor structures studied in this work consist of direct semiconductors. This is not a coincidence, as the direct transition allows for strong light-matter interaction. Moreover, the band gap energy falls in the vicinity of light emitted by

---

[1]Notably, the lattice parameters at standard laboratory conditions for GaAs $a = 5.65$ Å [Mad96, p. 104] and for InAs $a = 6.06$ Å [Mad96, p. 136] differ, which will lead to mechanical strain at a GaAs-InAs interface.

[2]As an example, the ratio amounts 1:1 for GaAs as one Ga atom comes to one As atom in the primitive cell.

[3]The semiconductor nanostructures in this work are studied at a temperature of $T = 6$ K, which puts only a negligible fraction of electrons in a higher energy state than the Fermi energy in thermodynamic equilibrium.

widely available laser sources and the smallest energy gap between VB and CB is located at the $\mathbf{k} = 0$ point, which enables to approximate the dispersion near the band gap by the quadratic dispersion for free electrons $E \sim \mathbf{k}^2/m^*$ with the reduced mass m^*. This is depicted in Fig. 2.2(a), which illustrates the bands close to the band gap around $\mathbf{k} = 0$.

The shown splitting of the bands close to the band gap is determined by their angular momentum quantum numbers. The total angular momentum of each band (state) $\mathbf{J}$ is given by the vectorial addition $\mathbf{J} = \mathbf{L} + \mathbf{S}$ of the orbital angular momentum $\mathbf{L}$ and the spin $\mathbf{S}$. The eigenstate to the orbital angular momentum $\mathbf{L}$ with its quantum number L in an atom describes the orbitals known as s, p, d, ... orbitals[4]. The amplitude of the spin is given by $S = 1/2$. The spin is discussed further in Sec. 2.2. The bands described by the total angular momentum can be denoted by their total angular momentum quantum number J, which remains a good quantum number in the semiconductor crystal. As a vector, $\mathbf{J}$ can be oriented along a given axis depending on the direction of $\mathbf{L}$ and $\mathbf{S}$. As $\mathbf{J}$ is quantized, J can only take a total of $2J + 1$ orientations. The different orientations are evaluated on the nano structure growth axis z and are therefore denoted J_z.

If the CB is s like it has an orbital momentum $L = 0$. Together with the spin quantum number $S = 1/2$, the amplitude of the total angular momentum amounts to $J = 1/2$, with two orientations $J_z = \pm 1/2$, which equally describe the spin orientation S_z. For the considered semiconductors, the VB is p like with $J = 1/2$ and $J = 3/2$[5]. The band with $J = 1/2$ is split off to lower energies due to the larger spin orbit (SO) interaction of the $J = 3/2$ band. The SO interaction results from the effective magnetic field experienced by a moving electron about an electric field, most notably the positively charged nucleus[6]. The motion is given by the orbital angular momentum $\mathbf{L}$ and the effective field is oriented parallel to it [Dya17, p. 4]. The SO splitting Δ_{SO} reaches $\Delta_{\mathrm{SO}} = 0.341\,\mathrm{eV}$ for GaAs [Mad96, p. 101], $\Delta_{\mathrm{SO}} = 0.38\,\mathrm{eV}$ for InAs [Mad96, p. 134], and $\Delta_{\mathrm{SO}} = 0.8\,\mathrm{eV}$ for CdTe [Mad96, p. 186]. This splitting is on the order of the band gap itself and the SO band can therefore be neglected here. While the $J_z = \pm 3/2$ and $J_z = \pm 1/2$ bands are degenerate at $\mathbf{k} = 0$ in zinc blende structures, the curvature of the parabolic bands is different, as illustrated in Fig. 2.2(a). The curvature is related to the effective mass m^* as second derivative of the dispersion relation and the $J_z = \pm 3/2$ band with the higher effective mass is called heavy hole (HH) band. Consequently, the $J_z = \pm 1/2$ band is denoted as light hole (LH) band.

---

[4] An s orbital is defined by $L = 0$, a p orbital by $L = 1$ and so on.

[5] The vectorial addition of $\mathbf{L}$ and $\mathbf{S}$ leads to both $\mathbf{J}$ amplitudes in the band.

[6] The deformation of the lattice in semiconductor nanostructures also leads to an electric field.

(a)

E

CB

(b)

E

$J_z = \pm 1/2$

$J = 1/2$

E_g

E_g

k

VB

k

$J_z = \pm 3/2$

$\Delta_{\mathrm{HH\text{-}LH}}$

$J = 3/2$

Δ_{SO}

HH

$J_z = \pm 1/2$

Δ_{SO}

HH

LH

LH

$J_z = \pm 1/2$

SO

$J = 1/2$

SO
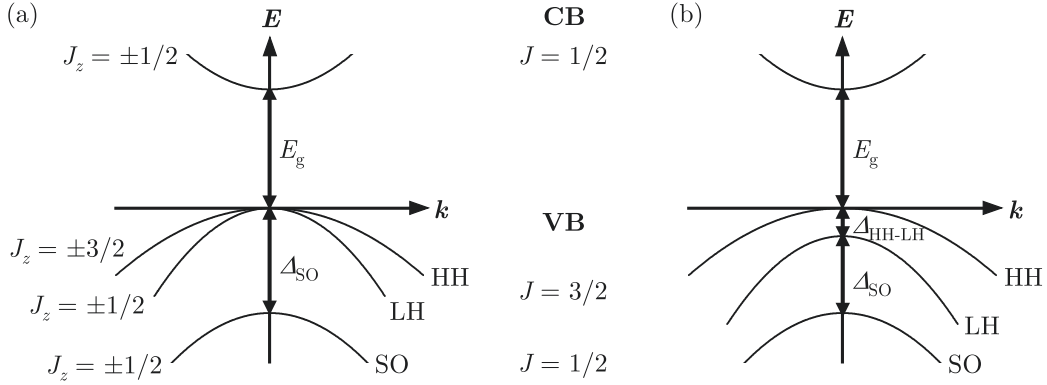
Figure 2.2: Simplified band structure of bulk and low-dimensional semiconductors around the center of the Brillouin zone $\mathbf{k} = 0$ near the VB-CB band gap. (a) The dispersion relation for the bulk semiconductors GaAs, InAs, CdTe [Kli07, p. 198]. The total angular momentum $J = {}^3/_2$ bands form the HH and LH bands, while the $J = {}^1/_2$ band is split off by Δ_{SO} as a result of the SO interaction. (b) The disperison relation for low-dimensional semiconductors as studied in this work. The degeneracy of HH and LH at $k = 0$ is lifted due to intrinsic strain and electron confinement. This leads to the HH-LH splitting $\Delta_{\mathrm{HH\text{-}LH}}$, which facilitates the ES polarization by circularly polarized light. The figure is adapted from Ref. [GKB10b, p. 40]

2.1.2 Low-Dimensional Semiconductor Nanostructures

In low-dimensional semiconductors, an electron is confined within an electric potential of a size comparable to the de Broglie wavelength in one or more dimensions. In the nanostructures studied here, a semiconductor material with a band gap energy smaller than the surrounding material serves as an electron trap. In the case of QDs, the (In,Ga)As compound is embedded within GaAs and for the QW structure, CdTe is embedded within a CdMgTe compound. The admixture of magnesium (Mg) raises the band gap energy. As the two semiconductor materials in a nanostructure usually also have different lattice constants, mechanical strain is introduced, which deforms the bulk crystal band structure. Together with the confinement, the degeneracy of HH and LH bands at $\mathbf{k} = 0$ is lifted, as has been shown for CdTe QW [Kuh93] and (In,Ga)As/GaAs QDs [Bay95]. The resulting band structure is depicted in Fig. 2.2(b). The splitting $\Delta_{\mathrm{HH\text{-}LH}}$ is in the range of ten meV and therefore considerably larger than the full width at half maximum (FWHM) of a picosecond laser with a FWHM of 1.5 meV[7].

The optical excitation of a direct semiconductors lifts an electron in the VB close to the CB and leaves an unoccupied hole. Consequently, the hole has a positive electric charge and forms a Coulomb bound exciton with the excited electron (exciton (X^0)).

---

[7]However, the intrinsic strain and local deformation at the material interface is assumed to be responsible for a significant HH-LH mixing [Kou04], but can be neglected at this point.

The exciton binding energy lowers the photon energy necessary for the electron excitation and is on the order of 4 meV for bulk GaAs [Mad96, p. 101], but rises up to 10 meV in 5 nm high GaAs QWs [Tar84]. However, the exciton recombines rapidly, caused by the direct transition within ps [Got98; Zhu07]. Note that the above considerations describe the ground states. The studied QDs, as an example, confine the electrons and excitons such that the states are indeed hydrogen like energy states [Bay02].

When doping the semiconductor nanostructure with excess electrons, a resident electron binds together with the photo generated exciton to form a negative trion X^-. Again, this lowers the necessary photon energy to excite the trion in the studied structures [Zhu07; Buh95]. After the trion recombination, the resident electron remains in the structure in the CB and can thus preserve an eventual spin polarization by light. This facilitates the efficient polarization of ESs in semiconductor nanostructures as shown in the next section.

2.2 Electron Spins in Semiconductors

The spin is a property of a particle and is classically described as an intrinsic angular momentum [UG25]. For a charged particle, any angular momentum can be understood as a magnetic dipole with a magnetic moment and therefore couples to a magnetic field **B**. As elucidated in the last section, the total angular momentum of an electron in the CB is defined by the spin $S = 1/2$. Moreover, the main interaction of nuclei with an external field is also by its spin and will be discussed in Sec. 2.3.

The interaction of the ES with the external field is given by the Zeeman interaction [Zee97] with the Hamiltonian [Ivc05, p. 238]

$$H_{\mathrm{Z}} = g_{\mathrm{e}} \mu_{\mathrm{B}} \mathbf{B} \cdot \mathbf{S} \tag{2.1}$$

with the Bohr magneton μ_{B}, the reduced Planck constant $\hbar$, and the electron g factor g_{e}. The g factor is specific in each material and electron state. Due to the scalar product, one has to take into account the orientation of the spin relative to the field, here oriented along x. This describes the Voigt configuration where the external field points perpendicular to the light propagation. As the spin is quantized it can be oriented in two eigenstates: $|S_x\rangle_+ = |\uparrow\rangle$ and $|S_x\rangle_- = |\downarrow\rangle$. In polar coordinates it reads

$$|\Psi\rangle = \cos\left(\frac{\theta}{2}\right) |\uparrow\rangle + \mathrm{e}^{i\varphi} \sin\left(\frac{\theta}{2}\right) |\downarrow\rangle$$

and forms a sphere called Bloch sphere by superposition of the two eigenstates. It is shown in Fig. 2.3. The angle θ is the polar angle and gives the tilting of the superposition spin state (proportion of $|\uparrow\rangle$ to $|\downarrow\rangle$) while φ is the azimuth angle

Figure 2.3: Visualization of a spin state $|\Psi\rangle$ on a Bloch sphere. The polar angle θ and the azimuth angle ϕ are given for the spherical coordinate system. The $|\uparrow\rangle$ and $|\downarrow\rangle$ states lie along the quantization axis of an external field in x direction and form the superposition states $|\rightarrow\rangle$ and $|\leftarrow\rangle$, as defined in Eq. (2.3) along the sample growth axis. The spatial coordinate system illustrates the orientation of the experiments in this work.
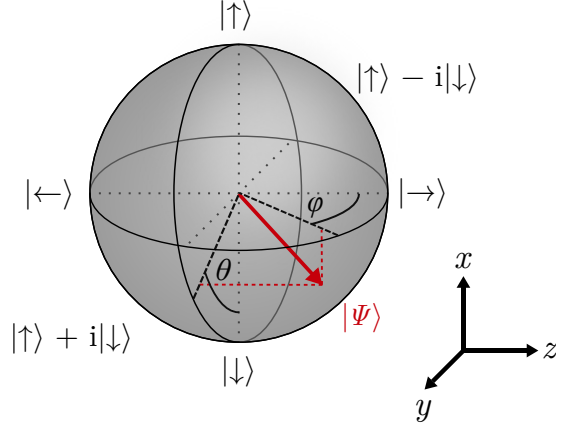
and gives the rotation of the spin state around the field axis. The eigenstates are separated in energy by the Zeeman splitting resulting from Eq. (2.1)

$$\Delta E_{\mathrm{Z,e}} = \hbar\omega_{\mathrm{L}} = g_{\mathrm{e}}\mu_{\mathrm{B}}B_x \tag{2.2}$$

which can be expressed by the Larmor frequency ω_{L}.

The z axis as nanostructure growth axis is of utmost importance as the strongest confinement of the electron is along this axis. The short ES notation along the z axis

$$|\rightarrow\rangle = \frac{|\uparrow\rangle + |\downarrow\rangle}{\sqrt{2}} \quad \text{and} \quad |\leftarrow\rangle = \frac{|\uparrow\rangle - |\downarrow\rangle}{\sqrt{2}} \tag{2.3}$$

is introduced as a superposition of the ES states along the external field B_x. A rotation along φ, between the $|\rightarrow\rangle$ and $|\leftarrow\rangle$ states, does not require an energy transfer into the spin system, as the states are orthogonal to the external field. The transfer between $|\uparrow\rangle$ and $|\downarrow\rangle$, however, requires the transfer of energy.

2.2.1 Spin Polarization by Circularly Polarized Laser Pulses

The optical selection rules in semiconductor nanostructures result from the band structure depicted in Fig. 2.2(b) and the angular momentum conservation. The latter dictates that the excitation with a circularly polarized photon can only lead to transitions with $\Delta J_z = \pm 1$ [HW04, p. 219] and only transitions along the lines given in Fig. 2.4 are allowed. When the spectral width of a laser pulse does not exceed the HH-LH splitting $\Delta_{\mathrm{HH\text{-}LH}}$, an excitation with σ^- polarized light only enables the transition from the VB HH state $J_z = +3/2$ to the CB $J_z = +1/2$ ($|\rightarrow\rangle$) state by forming an electron-hole pair. The electron-hole pair can only bind to a trion (X^-) with the resident electron if the latter is in the CB $J_z = -1/2$ ($|\leftarrow\rangle$) state (Pauli exclusion principle [Pau25]).
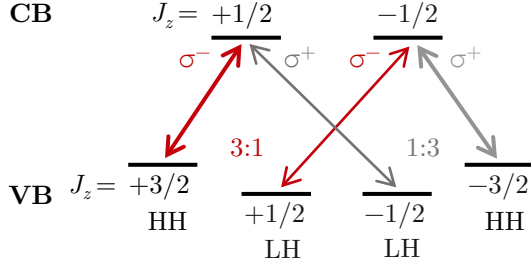
Figure 2.4: Optical selection rules for circularly polarized ($\sigma^\pm$) light in a low-dimensional semiconductor (GaAs, InAs, CdTe). The VB with HH-LH splitting [War13; Kuh93] as well as the CB is shown with their respective total angular momentum orientation J_z. The optical transitions are given with their amplitude ratio. Figure according to Ref. [DP84, p. 28] in electron representation[8] with the inclusion of HH-LH splitting.

The excitation with a circularly polarized laser pulse induces Rabi oscillations in the two level system of the $|{\leftarrow}\rangle$ and the trion $|{\Leftarrow}{\rightarrow}{\leftarrow}\rangle$ state, and the state of the whole system $|\psi\rangle_{\sigma^-}$ is given by [YB17, p. 182]

$$|\psi\rangle_{\sigma^-} = \alpha \, |{\rightarrow}\rangle + \beta \cos\left(\frac{\Theta}{2}\right) \, |{\leftarrow}\rangle + \mathrm{i}\beta \sin\left(\frac{\Theta}{2}\right) \, |{\Leftarrow}{\rightarrow}{\leftarrow}\rangle \quad . \tag{2.4}$$

The state of the system depends on the pulse area Θ of the laser pulse. The pulse area

$$\Theta \propto \int \, dE_{\sigma^\pm}(t)\mathrm{d}t \tag{2.5}$$

depends on the duration of the pulse, the amplitude of the light field $E_{\sigma^\pm}(t)$, and the effective transition dipole moment d [Yug09]. The two level system can be depicted in a Bloch sphere with the radius given by the fraction of the ES component β in the $|{\leftarrow}\rangle$ state at the moment of the pulse incidence (see Fig. 2.5). In the case of a $\Theta = \pi$ pulse, the whole $|{\leftarrow}\rangle$ component resident ESs is bound in a trion, while the fraction α in the $|{\rightarrow}\rangle$ state remains undisturbed. This leaves a net ESP after the application of a circularly polarized pulse.
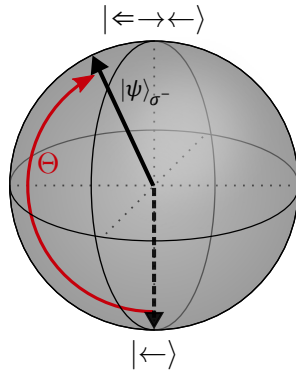
Figure 2.5: Coherent excitation of a resident electron to a trion visualized in a Bloch sphere. The pulse area Θ of a laser pulse is the polar angle. The excitation with $\Theta = \pi$ leads to a maximal trion excitation and consequently to a maximal ESP [Yug09].

---

[8] The difference between the electron representation and the mixed electron-hole representation is clearly illustrated in Ref. [SGR20].

2.2.2 Electron Spin Dynamics

The dynamics of the ES expectation value $\langle \mathbf{S}(t) \rangle$ follows the Bloch equations [Blo46]. A solution to it is given by [Var14b, p. 11]

$$\langle \mathbf{S}(t) \rangle = \frac{\hbar}{2} \begin{pmatrix} \cos \varphi \sin \theta \\ \sin \varphi \sin \theta \cos (\omega_{\mathrm{L}} t) - \cos \theta \sin (\omega_{\mathrm{L}} t) \\ \sin \varphi \sin \theta \sin (\omega_{\mathrm{L}} t) + \cos \theta \cos (\omega_{\mathrm{L}} t) \end{pmatrix}$$

and the ES therefore performs a precession about the external field axis x with the above mentioned Larmor frequency

$$\omega_{\mathrm{L}} = \frac{\mu_{\mathrm{B}} |g_{\mathrm{e}}|}{\hbar} B_x \quad . \tag{2.6}$$

This holds true if the polarization of the ES is conserved. This is obviously not the case in a real system. The decay of the ESP can be described in three timescales: (i) The depolarization or longitudinal relaxation (tilting along θ) is connected with an energy transfer and takes place on the time scale $T_{1,\mathrm{e}}$. It is commonly described by an exponential decay [Gla18c, p. 25]. (ii) The decoherence or transversal relaxation (rotation along φ) describes the loss of the phase relation between the two eigenstates[9] on the timescale $T_{2,\mathrm{e}}$. The loss of coherence is also generally assumed to be exponential [GKB10a, p. 6], but can resembles a power law for the hyperfine interaction with unordered NSs in QDs [KLG02]. (iii) The third timescale only applies for an ensemble of ESs and characterizes the loss of the total ESP due to a dephasing of the single ESs to each other. It happens within the time $T_{2,\mathrm{e}}^*$ following a Gaussian decay [MER02]. The dephasing of an ES ensemble will be discussed in Sec. 2.5. The main mechanisms responsible for the single ES relaxation (i) and (ii) are discussed below and in the following sections.

The ES relaxation is mediated by several mechanisms in bulk semiconductors [Dya17, pp. 22, 23][10]:

Elliott-Yafet Mechanism
The scattering of an electron at a charged impurity or the electric field of lattice vibrations (phonons) leads to an effective magnetic field, which changes the spin polarization by SO interaction [Ell54; Yaf63]. For low temperatures, as in this work, the scattering with phonons is negligible, which leaves the charged impurities as main relaxation channel for this mechanism proportional on the impurity concentration.

Dyakonov-Perel Mechanism
The energy splitting by SO coupling in non inversion symmetric crystals like zinc blende leads to an effective field between the two spin eigenstates. As the

---

[9]One could also say that the eigenstates lose the ability to form a coherent superposition.

[10]For resident electrons, the spin relaxation is not limited by the radiative lifetime as for photo excited electrons.

splitting depends on the electron momentum, the effective splitting changes with each scattering process at impurities. In between the scattering processes, the ES precesses undisturbed and the spin relaxation is therefore the more efficient the longer the time between scattering events is [DP71; DDP76]. The Dyakonov-Perel mechanism is, therefore, most effective for low impurity concentrations and is dominant over the Elliot-Yafet mechanism in the studied semiconductors in their bulk form [KRW04].

Bir-Aronov-Pikus Mechanism
The ES relaxation can take place by scattering with holes in semiconductors via electron-hole exchange interaction. This is a dominant relaxation channel in p doped semiconductors [BAP75], but is negligible in the n doped structures investigated in this work.

Admixture Mechanism
The SO interaction with the electric field resulting from the deformed lattice in semiconductor nanostructures leads to the admixture of opposing spin states to the initially single spin orientation sublevels. The spin independent phonon scattering then allows for an effective ES relaxation [KN01]. For large magnetic fields in QDs, this is the dominant relaxation channel [Gla18a, p. 168], as the unordered NSS develops a majority orientation in a directed external field and the energy mismatch between electron and nuclear Zeeman energies becomes significant, which renders the hyperfine interaction with unordered NSs less efficient.

As most of the relaxation mechanisms described above rely either on a considerable electron momentum (movement) or the presence of holes, the localization of the electron in nanostructures or on shallow donors blocks these relaxation channels and leads to a prolonged ES polarization out of thermal equilibrium [KN01]. The localization, however, strongly enhances the hyperfine interaction between ES and NS and opens up additional relaxation paths. The hyperfine interaction is therefore detailed in Sec. 2.4 after a brief introduction to the NSS in the next section.

2.3 Nuclear Spins in Semiconductors

Just as for the ES, the Zeeman interaction describes the coupling of the NS **I** to an external field **B** [Abr83c, p. 22]

$$H_\mathrm{Z} = -\hbar\gamma\mathbf{B}\cdot\mathbf{I}$$

with the gyromagnetic ratio $\gamma = {}^{g_\mathrm{N}\mu_\mathrm{N}}\!/\!_\hbar$. Here, g_N gives the nuclear g factor and μ_N the nuclear magneton. The resulting Zeeman splitting is consequently given by

$$\Delta E_\mathrm{Z,n} = \hbar\omega_\mathrm{L} = \hbar\gamma B_x \tag{2.7}$$

with the Larmor frequency $\omega_{\mathrm{L}} = \gamma B_x$.

An oriented NSS is also subject to depolarization to the lattice temperature (thermal equilibrium), although in the order of minutes or hours in semiconductors at cryogenic temperatures [Gla18c, p. 30]. The main depolarization mechanisms, without the important ES-NS hyperfine interaction fleshed out in the following section, are:

Nuclear Quadrupole Interaction
An electric quadrupole only interacts with an inhomogeneous electric field, but the cubic symmetric crystal geometry in bulk GaAs, InAs, and CdTe leads to a homogeneous electric field at the position of the nuclei and therefore prohibits quadrupole coupling [Urb13]. However, the crystal is deformed in semiconductor heterostructures as studied in this work due to the lattice mismatch between the two compounds. This introduces directed mechanical strain and a directed electric field gradient perpendicular to the interface, which enables the coupling of nuclear quadrupole moments [SPH61]. The quadrupole interaction introduces an additional relaxation channel due to the introduction of a local field gradient by a charged exciton [PAK08] and leads to the modification of the Zeeman splittings in strained nanostructures [Urb13].

Nuclear Dipole-Dipole Interaction
A NS establishes an effective field at the position of its neighbors, leading to the nuclear dipole-dipole interaction [Abr83a, p. 97]. The dipole-dipole interaction is efficient between neighboring NSs with differences in Zeeman splittings smaller than the local field exerted by one NS on the next [Kal17, p. 393], and is therefore hindered between different nuclear species (isotopes) or when the splitting is modified by strain, as in self-assembled QDs and narrow QWs. This interaction leads to the diffusion of NSP within the NSS, but the diffusion out of semiconductor nanostructures is limited [Urb13; Che15].

Direct Nuclear Spin-Phonon Coupling, Lattice Relaxation
Due to vibrations of the lattice (phonons) consisting of charged nuclei, the electric and effective magnetic field at a given nucleus position is not constant. While the magnetic interaction is negligible, the electric field couples to quadrupole moments of nuclei with spin $I > 1$ or in strained nanostructures [Abr83e, p. 401]. This ultimately leads to the dissipation of the NSP within the lattice.

They lead to depolarization timescales as for the ES. The dephasing time $T_{2,\mathrm{n}}^*$ of the total NSP due to a precession frequency spread results from different quadrupole splittings in strained, GaAs based structures and differing Knight fields stemming from the hyperfine interaction with ESs (see Sec. 2.4 for details). The NS dynamics beyond the dephasing are discussed by the introduction of a NS temperature [Abr83d, p. 133] in contrast to the lattice temperature (sample temperature). The timescale $T_{2,\mathrm{n}}$ then describes the timescale on which a NS reaches the NS temperature by NS diffusion (also given as decoherence). This is mainly mediated by the dipole-dipole

interaction on a typical timescale of 10^{-4} s [Kal17, p. 425]. Finally, the equalization of NS and lattice temperature occurs on the timescale $T_{1,\mathrm{n}}$ due to direct NS-phonon coupling and interaction with the electron, either with its charge or with its spin[11]. The latter contribution is characterized by the rate $1/T_{1,\mathrm{ne}}$, which also describes the timescale of the DNP by directing the hyperfine interaction detailed in the next section.

2.4 Hyperfine Interaction of Electron and Nuclear Spins

As foreshadowed, the hyperfine interaction between the ES and the (effective) NS magnetic moments (magnetic dipole interaction) drives their mutual relaxation in nanostructures. The hyperfine interaction coherently transfers the ESP to the NSS and vice versa.

The collinear hyperfine interaction in the studied nanostructures is mediated by the Fermi contact coupling, which depends on the overlap of carrier and nuclei wave functions. The interaction Hamiltonian is given by [MER02]

$$H_{\mathrm{HF}} = \sum_{\mathrm{n}} A_{\mathrm{n}}(\mathbf{I}_{\mathrm{n}} \cdot \mathbf{S}) \tag{2.8}$$

with the hyperfine coupling constant A_{n}. The sum runs over all nuclei n in a QD. In the studied semiconductors (zinc blende lattice), the orbital wave function of the electron can be described by a separation of the Bloch amplitude $\mathcal{S}(\mathbf{r})$, as the electron wave function inside the primitive cell of a given material, and the electron wave function envelope $\xi(\mathbf{r})$ over the nanostructure consisting of many primitive cells [Gla18b, p. 64]. The hyperfine coupling constant A_{n} will depend on the envelope amplitude at the position of a nucleus, detailed below. The collinear hyperfine interaction is, therefore, efficient for electrons in the s like CB but does not couple HH in the p like VB to the NS[12]. It contains a dynamic part, expressed in ES-NS flip-flop processes, where a single NS flips simultaneously with the ES, and a static part which is responsible for the effective field exerted by the NS on the ES and vice versa [FLS17, p. 442].

The effective magnetic field acting on ESs is described by the OF B_{N} [MER02]

$$B_{\mathrm{N}} = \frac{1}{g_{\mathrm{e}}\mu_{\mathrm{B}}} \left\langle \sum_{\mathrm{n}} A_{\mathrm{n}}\mathbf{I}_{\mathrm{n}} \right\rangle_{N} \quad , \tag{2.9}$$

---

[11] The NS temperature of the surrounding NSS is equalized with the lattice temperature and the diffusion out of the QD resembles a depolarization described by the timescale $T_{1,\mathrm{n}}$. As the NSS of a QD is decoupled from its surrounding NSS by differing NS level splittings, which effectively block the dipole-dipole interaction, $T_{1,\mathrm{n}}$ in QDs reaches up to hours [Gre07].

[12] The hyperfine interaction can, however, affect hole spins in the case of HH-LH mixing in strained QDs [Kou04]. Additionally, the HH spins in the p type valence states couple by dipole-dipole interaction to the NS. The dipole-dipole interaction is an order of magnitude smaller than the Fermi contact interaction [Gla18c, p. 18].

with the index n running over all nuclei covered by the envelope, which leads to a modification of the ES levels and the ES precession frequency in an external field. The OF is averaged over the contributing nuclei N. Conversely, the hyperfine interaction acting on a NS is described by the (time-averaged) Knight field $\mathbf{B}_K$ for a localized electron [Kal17, p. 392]

$$B_K = -F \frac{\hbar A_n}{\gamma_n} \mathbf{S} \tag{2.10}$$

with the filling factor F quantifying the relative occupation time of the electron at the nucleus.

In order to connect the the hyperfine coupling constant A_n to experimental parameters, one can expressed it as

$$A_n = v_0 A |\xi(\mathbf{R}_n)|^2 \quad .$$

The envelope $\xi(\mathbf{R}_n)$ is evaluated at the position of the n-th nucleus. The envelope can be considered constant within the primitive cell volume v_0. Note that the sum over all $|\xi(\mathbf{R}_n)|^2$ is approximately normalized to unity, when multiplied with v_0. This renders the (isotropic) hyperfine constant A a material constant[13].

Figure 2.6: An scanning tunneling microscope (STM) image of a self-assembled InAs/GaAs QD before capping with GaAs and annealing. The samples used are n doped and the single ES (black arrow) is localized in a NS bath of 10^5 NSs (red arrows). The molecular-beam epitaxy (MBE) growth is from bottom to top. STM image from [Eis08].
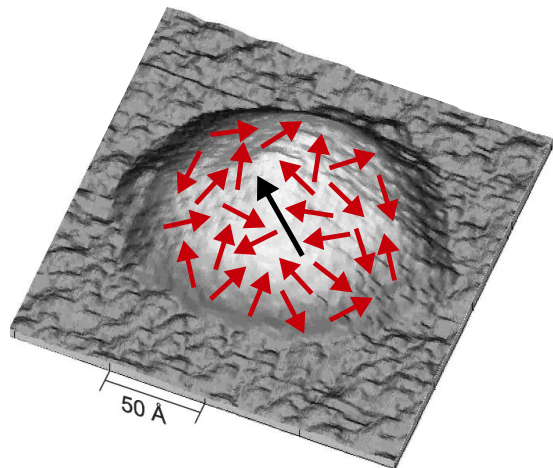
In bulk semiconductors, electrons are not bound to a single nucleus. This limits the interaction with a single NS, corresponding to the time the electron wave function overlaps with the nucleus. In QDs, however, the ES is localized on the small number of $N \approx 10^5$ nuclei (see Fig. 2.6) and the filling factor F is close to 1[14]. The interaction with the arbitrarily ordered NSs leads to an ESP dephasing by

---

[13] Note that it further depends on the exact primitive cell and the Bloch amplitude of the electron wave function therein [Gla18b, p. 64]. As an example, the primitive cell of GaAs incorporates two nuclei with different hyperfine constants, but the volume of the primitive cell scales accordingly.

[14] While the localization is weaker for a shallow donor in a low-density QW, it is still prominent enough to experience a considerable hyperfine interaction.

introducing a Gaussian distributed fluctuating NS field with the half width at half maximum (HWHM) δB_{N}, which scales with the number of nuclei by $\sqrt{N}^{-1}$ [Gla18c, p. 35]. Similarly, a fluctuating Knight field $\delta\omega_{\mathrm{e}}$ forms a NS relaxation channel[15].

The noncollinear hyperfine interaction to consider in this work is the interaction of ESs with the tilted NSP due to the quadrupole interaction in strained QDs [DK07]. Therefore the noncollinear hyperfine interaction can lead to a NSP perpendicular to the ESP by the scalar hyperfine interaction (2.8)[16] [Kre10].

To conclude, the hyperfine interaction renders the following ES and NS channels efficient:

Hyperfine Interaction with Disordered Nuclear Spins
The NSs in the crystal lattice are disordered and the ESs are therefore in a randomly oriented effective magnetic field [KLG02; MER02]. This leads to the depolarization by hyperfine interaction and the coherent transfer of ESP to the NSS. The hyperfine interaction of ES and NS is discussed in more detail in Sec. 2.4. The contribution to the ES relaxation is only weak in bulk semiconductors but becomes the dominant one for localized electrons as in QDs [Blo54]. In moderate longitudinal magnetic fields, however, this relaxation channel is suppressed, as evidenced from the polarization recovery curve (PRC) [SK03] (see Sec. 3.2.5 for details).

Hyperfine Interaction with Disordered Electron Spins
On the other end of the NS-ES hyperfine interaction, the NSs are subject to a randomly oriented ESP. While the randomly oriented NSP can be considered frozen for the ESs, the NSs are subject to a rotating ESP[17] [MER02]. Additionally to being a depolarization channel, the hyperfine interaction can be used to polarize NSs by ESs (see Sec. 2.4).

Electrostatic Coupling to Nuclear Quadrupoles, Noncollinear Hyperfine Interaction
Although nuclei do not feature an electric dipole moment, nuclei with a spin $I \geq 1$ have an electrostatic quadrupole moment due to a non spherical charge distribution which interacts with an inhomogeneous electric field [Urb13]. Resident electrons in the s like conduction band, as studied in this work, however, do not couple to the nuclear quadrupole potential directly [Abr83b, p. 165]. The interaction of NSs with quadrupole moments and electric field gradients in strained QDs preserves a tilted NSP which, in turn, interacts with the ES via hyperfine interaction [Kre10]. Moreover, the NS is directed even without an external field due to the quadrupole interaction, which is expected to elongate

---

[15]In a typical self-assembled QD, the fluctuating nuclear field amounts to tens of mT while the fluctuating Knight field reaches only several mT [Gre09].

[16]The investigations in this work are performed in Voigt geometry where the applied external field is oriented perpendicular to the light propagation.

[17]The Larmor frequency of ESs is several orders of magnitude larger than that of NSs.

the ES coherence [DK07] as it is expected to replace the external field. This noncollinear hyperfine interaction is detailed in Sec. 2.4.

However, the hyperfine interaction can be harnessed by directing the transfer of the ESP to the NSS [Gam97] and thereby shaping the effective field for the ESs[18], referred to as DNP. To make use of the dynamic part of the hyperfine interaction, one has to consider, that the nuclear magneton μ_N is three orders of magnitude smaller than the Bohr magneton μ_B, which leads to a thousandfold difference in the nuclear and the electron Zeeman splittings and Larmor frequencies [Urb13]. This prohibits an ES-NS flip-flop (the spin of a single electron and a single nucleus flip simultaneously) even at moderate external fields [Gam01] and asks for the provision of energy by either an (external) RF field (solid effect [Abr83e, p. 393]), the additional quadrupole splitting NSs are subject to in strained structures [Kre10], or a detuned optical excitation where the detuning energy covers the missing energy of an ES flip (optical Stark effect [Kor11]). Two detailed examples are given in Sec. 2.5.2.

To conclude, the localization of the resident ES in a strained QD leads to an enhanced ES-NS coupling with reduced NS diffusion out of the QD. The ENSS therefore provides a good investigation platform of complex phenomena arising from the hyperfine interaction.

2.5 Electron-Nuclear Spin System in an Ensemble of Quantum Dots

The studied QD ensemble consists of weakly interacting single electrons each localized in one QD and separated by approximately 30 nm [Spa11]. An additional time scale emerges by the ES ensemble dephasing as a result of the ES precession frequency spread within the ensemble ESs, as evidenced by optical pump probe (PP) experiments [Bau94; Yug07]. Two contributions to the frequency spread need to be taken into account, which ultimately originate from the different QD sizes and indium (In) to Ga fractions in each dot [Eis08]:

(i) The NSF δB_N depends on the QD size and is therefore unique for each QD. The actual OF in a given QD at a given time is randomly taken from the individual Gaussian distributed NSFs [KLG02]. The NSF therefore leads to a dephasing characterized by the time $T_{2,f}^*$ which is independent of the external field magnitude

---

[18] As one way to quantify the transfer efficiency, the leakage factor f_N is introduced [BGK08; FM84, p. 183]

$$f_N = \frac{T_{1,n}}{T_{1,n} + T_{1,ne}}$$

as a relation of the NS-lattice relaxation rate $1/T_{1,n}$ to the (de)polarization rate $1/T_{1,ne}$ due to the interaction with ESs.

B_x. For a QW structure with a low density electron gas, the number of NSs interacting with an ES is several orders of magnitudes larger and the NSF can therefore be neglected for the ESP dephasing [Zhu09].

(ii) The differences in the QD composition and size lead to a difference in g factor in each QD and depends negatively linear on the trion excitation energy E_{Tr} [RLZ59; Yug09]. The g-factor spread in a QW is narrow and therefore does not lead to a significant dephasing [Zhu06]. By the excitation with a pulsed laser of wide spectral distribution, the g-factor distribution Δg_e leads to an ES precession frequency spread of $\Delta \omega_{g_e}$ and ESP dephasing quantified by the time $T_{2,g}^*$, which scales inversely linear to the external field[19]

Combined with the single ES decoherence time $T_{2,e}$, the dephasing rate of the ESP is given by

$$\frac{1}{T_{2,e}^*} = \frac{1}{T_{2,e}} + \frac{1}{T_{2,f}^*} + \frac{1}{T_{2,g}^*} \quad .$$

The dynamics of the ESP projection S_z in an ensemble subject to an external field B_x then follows a Gaussian decaying cosine after an excitation with a pulse area as introduced in Eq. (2.5) $\Theta = \pi$ [MER02]

$$S_z = S_{z,0} \cos\left(\omega t + \phi\right) \exp\left[-\frac{t^2}{2\left(T_{2,e}^*\right)^2}\right] \tag{2.11}$$

with the ESP projection right after the pulse $S_{z,0}$.

2.5.1 Resonant Spin Amplification and Spin Mode Locking

The trion recombination releases the bound resident electron after a random time on the time scale of its recombination time τ_{Tr}, which resets the ESP. The ESP can be amplified by applying a train of laser pulses with a laser pulse repetition period (PRP) $T_R < T_{2,e}$ as follows.

In an external magnetic field B_x transversal to the light propagation, a resident electron not bound in a trion precesses with the Larmor frequency ω_L about B_x. The trion is in a singlet ground state which prevents the precession of an ES within [Sha03]. The trion recombination time τ_{Tr} is orders of magnitudes shorter than $T_{2,e}$[20] and T_R.

Obviously, a resident ES precessing with the same frequency as the PRF, polarized along $|\rightarrow\rangle$ at the incidence of the first pulse, remains undisturbed by each laser

---

[19]In a typical (In,Ga)As/GaAs QD sample the g-factor spread amounts to $\Delta g_e = 0.0018$ meV^{-1} [Gre09].

[20]In a typical (In,Ga)As/GaAs QD sample $T_{2,e} \approx 800$ ns [Her08] and $\tau_{Tr} \approx 400$ ps [Gre06b]. Similar ratios are found in CdTe/CdMgTe QWs [Zhu07].

pulse and its $|\rightarrow\rangle$ component relaxes within the ES coherence time $T_{2,\mathrm{e}}$. A resident electron bound in a trion is released with a random phase of its Larmor precession to the laser pulses. If the precession of the previously bound resident ES is in the right phase to the laser pulses and if its Larmor frequency matches the PRF $\omega_\mathrm{R} = 2\pi T_\mathrm{R}^{-1}$, the total ESP is amplified. This happens until a large portion of ESs with a fitting Larmor frequency (2.6) precesses in phase. The phase synchronization condition (PSC)

$$\omega = K\omega_\mathrm{R} = \frac{g_\mathrm{e}\mu_\mathrm{B}}{\hbar}B_x, \ K \text{ integer.} \tag{2.12}$$

defines the modes K which are amplified. In contrast, ESs with a not fitting frequency are depolarized by every laser pulse. This is shown in Fig. 2.7(a) for a steady state ESP. The red peaks give the periodic laser excitation. The black and gray curves depict the ES precession with the mode numbers $K = 3$ and $K = 3.5$, relaxing exponentially in the time scale $T_{2,\mathrm{e}}$.

As the ES precession frequency is spread within an ES ensemble (see Sec. 2.5), more than one mode commensurate with the PRP can be amplified and the number of participating precessing modes M is calculated by [GYB09]

$$M = \frac{2\Delta\omega T_\mathrm{R}}{2\pi} \tag{2.13}$$

with the frequency spread $\Delta\omega$[21]

$$\Delta\omega = \frac{\mu_\mathrm{B}}{\hbar}\sqrt{(\Delta g_\mathrm{e}B_x)^2 + (g_\mathrm{e}\delta B_\mathrm{N})^2} \ .$$

The multi-mode precession leads to beating patterns of the total ESP projection S_z between the precession phase defining pump pulses. Two examples for different mode amplitude distributions are illustrated in Figs. 2.7(b) and (c)[22]. Four neighboring ES precession modes are shown in shades of gray together with their sum as a thick black line. For a flat mode amplitude distribution (all modes have the same amplitude), Fig. 2.7(b), three beating nodes caused by destructive interference are observed. For Gaussian distributed mode amplitudes centered around $K = 6.5$, Fig. 2.7(c), the total ESP dephases on the time scale $T_{2,\mathrm{e}}^*$ and rephases only before the next pulse within the same time scale. This is referred to as ES mode locking (ML) [Gre06c] with the ML (revival) amplitude observed right before the next pump pulse. Similarly, S_z also rephases, when the train of pump pulses is suddenly blocked. As depicted in Fig. 2.7(d) for Gaussian distributed mode amplitudes, the sum of the neighboring modes rephases on integer multiples of the PRP T_R. This is referred to as ESP bursts, numbered starting from the burst right after the last pump pulse [Gre07].

---

[21] The term $\Delta\omega$ denotes the FWHM of the frequency spread and M gives the number of major modes. The number of modes can also be modified by additional ES modes activated by a non-fluctuating OF.

[22] The hole precession in the trion and the trion decay observed in a real world experiment is not depicted here.
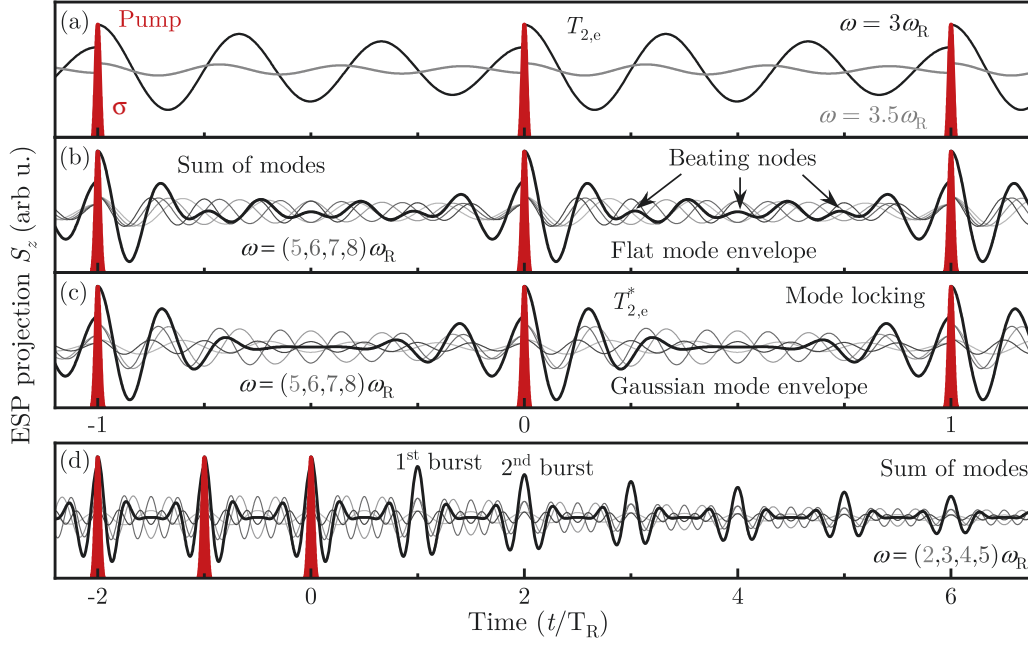
Figure 2.7: RSA and superposition (thick black line) of equally spaced modes (shades of grey, without NIFF). (a) The in-phase arrival of the ESP with a precession frequency of multiples of the PRF ω_R leads to the amplification of resonant modes ($\omega = 3\omega_R$). Non-resonant modes ($\omega = 3.5\omega_R$) are not amplified. (b) Four neighboring modes $\omega = K\omega_R$ ($K = 5, 6, 7, 8$) of flat amplitude envelope lead to the formation of ESP revivals before the next pump pulse. Moreover, three beating nodes form in the superposition of the four ES precession modes. (c) The four neighboring modes of (b) with Gaussian distributed amplitude envelope. The revival before the next pump pulse persists but the superposition is flat in between the pump pulses. (d) Evolution of the superposition of the modes $K = 2, 3, 4, 5$ with Gaussian amplitude distribution after the pulsing stops at $t = 0$. ESP bursts form at each multiple of the PRP. Panel (a) according to Ref. [Yug12].

The ES precession frequencies in CdTe QWs are homogeneous to the point, that only one mode contributes to S_z [Zhu06]. Therefore the ES beatings are not observed, but the ESP is amplified only when B_x leads to a commensurate ES precession frequency. The ESP projection S_z then peaks as a function of the external field, which is observed as a resonant spin amplification (RSA) curve [KA98].

2.5.2 Nuclei-Induced Frequency Focusing and Spin Dragging

To complete the background of this work, two examples of the rich hyperfine mediated spin phenomena in the ENSS of self-assembled QD are presented in the following: The beating patterns in Figs. 2.7(b)-(d) directly reveal the underlying mode structure by Fourier transform and their modification indicates changes in

the effective magnetic field, namely the OF. When excited by pump pulses with a PRP of 13.2 ns, 90 % of all ESs in the QD sample end up in the amplified precession modes [Gre07], which is referred to as nuclei-induced frequency focusing (NIFF). NIFF adjusts the OF exerted by the NSs in a QD on the ES to tune the precession frequency such, that it matches the PRF. In order to transfer the ESP to the NSP via the scalar, collinear hyperfine interaction (2.8) in a transversal magnetic field, either an effective nuclear field with a component along the optical propagation or a component of the ESP along the external field is required. For NIFF, one of the proposed microscopic origins [Car09] takes into account the optical Stark field as a result of the excitation with a laser pulse spectrally detuned from a trion resonance [Kor11]. The Stark field is oriented along the y axis and leads to a subtle tilting of the ESP in the direction of the external field, which enables the collinear hyperfine interaction. Moreover, the detuning provides the necessary energy to compensate for the differences in ES and NS Zeeman splittings. Including the OF, the PSC (2.12) needs to be modified to [Sha03; Yug09]

$$\omega = K\omega_{\mathrm{R}} = \frac{g_{\mathrm{e}}\mu_{\mathrm{B}}}{\hbar}B_x + \omega_{\mathrm{N}}, \; K \text{ integer.} \tag{2.14}$$

Instead of introducing the PRF as a temporal resonance condition, the OF in a single QD can also be varied by spectral spin dragging [Xu09; Lat09; Hög12]. Here, the trion is resonantly excited by a continuous wave (cw) laser in a (transversal) magnetic field B_x and the absorption in the QD is then determined by a cw probe laser. A slow spectral sweeping of the probe laser then reveals, that the trion resonance is dragged to higher energies, supported by the Zeeman energy provided by the OF. The NS polarization transversal to the ESP is attributed to noncollinear hyperfine interaction mediated by the nuclear quadrupole interaction [Kre10; HH10; Hög12] (see Sec. 2.4).

This work builds upon the discussed examples and investigates the underlying interactions. In order to set the stage, the NS dynamics in strain reduced, non quadrupole CdTe QWs is investigated by means of optically-detected NMR (see Sec. 3.4 for details on the experimental method). By switching to (In,Ga)As/GaAs QDs with their enhanced ES-NS interaction, NIFF is analyzed with unprecedented resolution of the constituent ES precession frequencies, which sheds light on the OF contribution. Subsequently, the efficiency of the NS polarization is enhanced by employing an increased PRF of 1 GHz, as compared to the widely studied PRF of 75 MHz. This allows on the one hand to increase the OF created by NIFF and to reduce the NSF, while it establishes a novel NS polarization scheme in a transverse external field on the other hand. In contrast to the spectral spin dragging, in this scheme, the external field drags the NSP which allows one to build up a significant OF in the inhomogeneous QDs of an ensemble simultaneously (without the need for extensive QD binning before the NS polarization).

3 Experimental Details

This chapter describes the experimental techniques used to obtain the results discussed in the following chapters. As a base, a pump-probe setup is used, which allows one to measure short timescales with high temporal resolution. Moreover, two extensions to this basic technique are laid out. The first describes a way to increase the total time, that a system can be observed and the second implements an RF setup to additionally modulate the NSs.

3.1 Faraday Rotation and Ellipticity

The Faraday rotation (FR) and Faraday ellipticity (FE) probe the real and the imaginary part of the complex refractive index of a material subject to a magnetic field, respectively. These properties can be measured in a transmission setup while the magneto-optical Kerr effect is measured in a reflection setup [HO17, p. 140].

One notable feature is the different response of the FR and the FE on a possible detuning of pump and probe energies. While the FE shows an absorption-like dependence on the detuning, the FR shows a dispersion-like profile [Gla10][1]. The detuning is working within each pulse, where the photon on one flank of the spectral profile is detuned from a photon on the other side of that flank. Therefore, even for degenerate pump and probe pulses stemming from one laser, the effect of detuning is relevant. The different spectral profiles of FR and FE should be taken into account additionally, when inferring from the measured signal to the actual ES projection. Note that the average electron g factor is dependent on the trion excitation energy and hence the spectral profile may alter the average electronic g factor observed in the experiment.

3.2 Pump Probe Setup

The systems studied for this work exhibit timescales of several nanoseconds up to microseconds with oscillation periods of the ES on the order of tenth of picoseconds.

---

[1]Therefore, the FE is best suited for an optically degenerate measurement (the optical pump energy equals the optical probe energy), while the FR yields a higher signal for optically detuned setups.

The following setup offers the temporal resolution and the extended setup enables to measure the undisturbed kinetics by offering the total scanning time necessary.

3.2.1 Pump Probe Principle

The pump probe technique implements a prototype experiment. A pump pulse is used to excite a system under study and an ideally non-perturbative probe pulse measures a physical property of the system. In order to get the full dynamics of the probed property, the sequence of pump and probe pulses has to be repeated with a slightly changed delay between them. A scheme can be found in Figure 3.1(a). The physical property measured here are the FR and FE of a linearly polarized probe pulse. For the remainder of the section, FR is written although the same would apply to FE measurements if not stated otherwise.
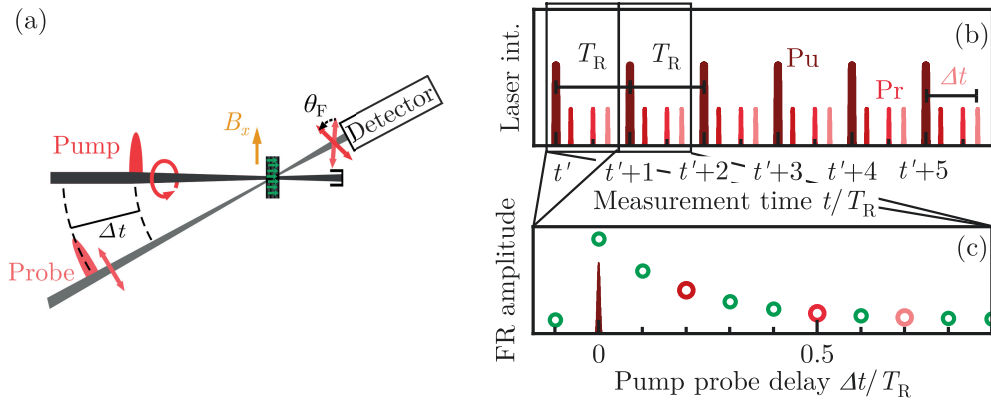

Figure 3.1: Principle of a pump-probe experiment. (a) Scheme. Pump and probe pulses hit the sample with a fixed time delay Δt. Here, the pump pulse is circularly polarized to induce an ES orientation in an external magnetic field B_{ext} and the probe pulse is linearly polarized. The tilted polarization axis by an angle θ_F of the transmitted probe pulse due to the FR is detected. (b) Pulse arrival diagram. Starting from time t', the probe pulses arrive shifted by a set time delay. This basic measurement is repeated each laser pulse repetition period T_R and the signal is integrated. As a next step, the delay is shifted to another Δt and the signal is again integrated. (c) The resulting PP curve shows the dynamics of the ESP. The integrated signals of different Δt are plotted against their respective delay. Zero delay is the coincidence of pump and probe pulses, while a negative delay is equivalent to a large positive delay.

The laser emits pulses with a PRP T_R between them. On the one hand, the measurement is repeated every T_R and thus allows for millions of measurements in one second. On the other hand, the free dynamics can be measured only for systems with dynamics faster than the time delay of T_R between pump and probe pulses. On panel 3.1(b), a protocol of pump and probe pulses is depicted. The pulse

amplitude is shown versus the measurement time. The pump pulses are shown in dark red with a lager amplitude and the probe pulses are shown in shades of light red. Each measurement consists of only one probe pulse, the other two probe pulses are shown to depict the process of consecutive measurements with the probe pulse shifted relative to the pump pulse. The dashed boxes show a single measurement within T_R. The resulting points taken for each measurement and delay between pump and probe pulses are shown on panel 3.1(c). The FR amplitude (green dots) is plotted versus the measurement time. The pump pulse is again shown in dark red. The points colored in shades of lighter red correspond to the accordingly colored probe pulses in panel 3.1(b).

To achieve a FR amplitude trace over a given time, one proceeds as follows. Pump and probe pulses are set to have a certain time delay. The measurement of this time delay is repeated each PRP and the resulting FR amplitudes are added up. One datapoint on the graph in panel 3.1(c) is traced. Then the time delay is varied by a small amount and again the resulting FR amplitudes are added up. Note that a negative time delay is the same as a large positive time delay due to the periodicity of the laser pulses. As stated before, the longest dynamics that can be traced undisturbed using this method is ultimately limited by the PRP, while the length of the traceable dynamics is limited by the maximal time delay between pump and probe pulses. The resolution of the traced dynamics is limited by the resolution of the time delay that can be set between pump and probe pulses or the laser pulse duration.

3.2.2 Experimental Realization of the Pump Probe Principle

The experimental realization is a strongly modified version of the pump-probe setup already used before [Gre06a; Bau94]. A detailed version of the setup is depicted on Figure 3.2. This section describes a general setup mostly used for this thesis. Changes to this setup will be stated in the corresponding sections.

The pump and probe pulse trains stem from the same laser source. The beam containing the laser pulses is guided through a telescope setup of two plano-convex lenses to achieve a collinear beam. Each pulse is split into a pump and a probe pulse with the pump pulse containing 90 % and the probe pulse 10 % of the intensity after losses of the beam splitter.

The pump pulse train is then directed along a variable mechanical delay of 4 m length (13.3 ns delay). Throughout this work, the pulse duration is not smaller than 150 fs while the resolution of the time delay amounts to a maximum of 100 fs. The resolution is therefore only limited by the laser pulse duration. As a next step, the pump pulses pass a gray filter wheel to set the appropriate average power. Before hitting the sample, the pump pulse train is helicity modulated between σ^+ and σ^- by a PEM with a pump modulation frequency of $\nu_{\mathrm{Mod,Pu}} = 84\,\mathrm{kHz}$.
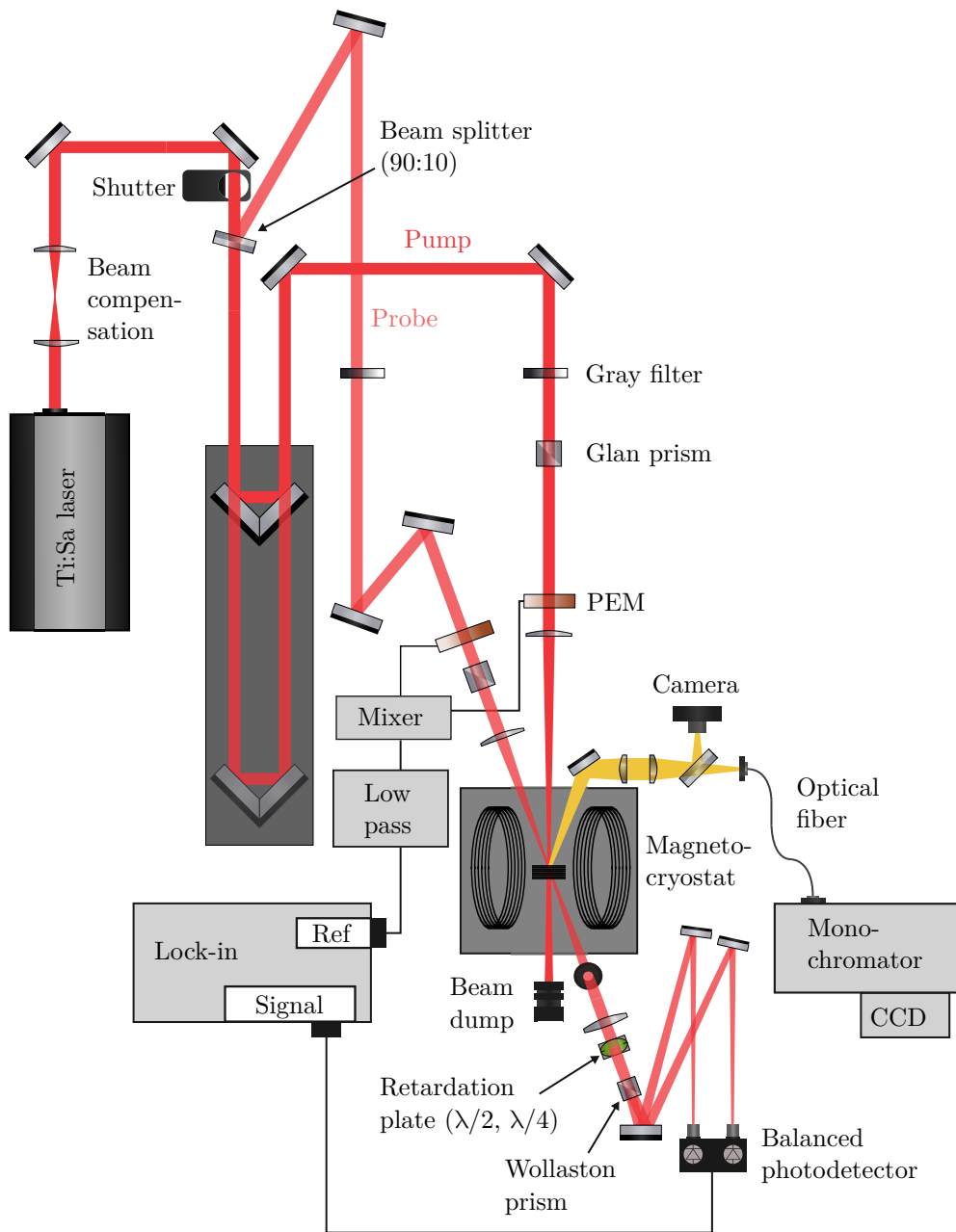
Figure 3.2: Scheme of the experimental setup for the PP experiments. Additionally to the optical PP setup, the electric setup for the double modulation is shown. The electric Sine signals from the photoelastic modulators (PEMs) are mixed (multiplied) and the difference frequency is used as a reference for the lock-in amplifier. Shown in yellow is the sample imaging with white light scattered from the sample surface as well as the spectrometer setup with monochromator and charge-coupled device (CCD) for recording the photoluminescence spectrum (PL).

This modulation frequency is slow enough to allow the full polarization of the ES [Zhu18b] and fast enough to prevent a significant NSP via DNP [MBI07] in one half of the modulation period. The circular polarization allows for the spin polarization selective ES orientation (see Section 2.2.1). To increase the average power per area, the pump beam is focused to a spot diameter of approximately 50 μm (FWHM) by passing through a biconvex lens with a focal distance of 250 mm. The lens is positioned such, that the focal point is slightly moved behind the sample plane to ensure a slightly larger spot size than the probe beam. As the experiments presented in this work are transmission experiments, the transmitted pump pulses are dumped behind the sample.

After being split from the pump pulse train, the probe pulses are directed over the optical table to accumulate a fixed flight time, that allows one to cover the delay range of interest by the pump pulses via the mechanical delay. The probe beam also passes a gray filter wheel to adjust the average power. Before hitting the sample, the probe pulses are intensity modulated by a combination of a PEM and a Glan prism. The PEM varies the linear polarization of the light between vertical and horizontal. The Glan prism transmits only vertically polarized light, which in combination leads to a vertically polarized beam, that is intensity modulated with a frequency of $\nu_{\mathrm{Mod,Pr}} = 100\,\mathrm{kHz}$. Note that this configuration ensures a modulation going through zero light amplitude so that even a not perfect modulation leads to a high modulation depth. As for the pump beam, the probe beam is directed through a biconvex lens with a focal distance of 250 mm but the focal point is placed on the sample plane. The spot size on the sample is approximately 45 μm FWHM.

After the transmission through the sample, the divergent probe beam is collected using a biconvex lens. To realize an optical polarization bridge, the polarization is split by a Wollaston prism such, that the vertical linear polarization is split from the horizontal polarization. Each polarization is directed into one entrance of a balanced photo-detector. To balance the light intensity on the entrances, a wavefront retardation plate is used in front of the Wollaston prism. A wavefront retardation plate delays the wavefront of light of one polarization relative to the wavefront of light of the transversal polarization by an amount equal to the indicated value upon transmission of the whole plate. A retardation of $\lambda/2$ tilts the polarization axis of linearly polarized light. A retardation of $\lambda/4$ transforms linearly polarized light to circularly polarized light and vice versa. The change of the complex refractive index in the ES polarized sample leads to a change of either the polarization axis (θ_{F}, FR) or the FE of the probe beam [Far46; BS66, p. 400]. To measure the FR, the light intensity on both entrances is balanced by a $\lambda/2$ retardation plate such that in the balanced case the polarization axis stands at 45° relative to the Wollaston prism. The FE is analyzed by placing a $\lambda/4$ plate in front of the Wollaston prism. In this way, a difference in amplitude of the circularly polarized light components is transformed into a tilt of the polarization axis and, therefore, a difference of the amplitude on the two diodes. Hence, a change of either the FR or the FE leads to an electric difference signal from the balanced photo-detector.

As the probe pulse train is modulated with $\nu_{\mathrm{Mod,Pr}}$, the main contribution to this electric signal is also running on the frequency $\nu_{\mathrm{Mod,Pr}}$. The electronic spin orientation is modulated with $\nu_{\mathrm{Mod,Pu}}$ and the signal of interest is, therefore, detected at the sum and the difference frequency $\nu_{\mathrm{Mod,Pu}} + \nu_{\mathrm{Mod,Pr}} = 184\,\mathrm{kHz}$ and $\nu_{\mathrm{Mod,Pu}} - \nu_{\mathrm{Mod,Pr}} = 16\,\mathrm{kHz}$ [AZ11]. The balanced photo-detector is specified to register signals with a frequency of up to $125\,\mathrm{kHz}$ and the signal with the sum frequency is not registered properly. The electric signal containing the signal of interest modulated with the difference frequency is fed to a lock-in amplifier (LI). An LI can be described as a frequency sensitive amplifier, which converts an electric signal oscillating with a given reference frequency to a constant voltage, which is proportional to the amplitude of the oscillating signal. Here, the reference frequency is taken from the modulating PEMs by feeding their output frequency into an electronic, multiplicative mixer. The mixer's output signal consists of the sum and the difference frequency of $\nu_{\mathrm{Mod,Pu}}$ and $\nu_{\mathrm{Mod,Pr}}$. The sum frequency is blocked by plugging an electric $45\,\mathrm{kHz}$ low-pass filter between the mixer and the LI, and the signal with the difference frequency serves as the reference signal for the LI. Note that, in this way, the reference signal is phase-synchronized to the optical modulation. Note also that the probe's optical modulation frequency $\nu_{\mathrm{Mod,Pr}}$ is double the modulation frequency by the probe PEM and the double frequency ('2f') electric output of the PEM is used for the electric reference.

The sample under study is placed in a magneto-cryostat. The cryostat is a Helium bath cryostat which allows to cool the sample down to $5\,\mathrm{K}$ by immersing the sample into cold Helium gas in a variable temperature insert (VTI). To further cool down the sample, the VTI can be flooded with liquid helium and evacuated to several millibar. By reducing the pressure in the VTI (a constant volume), the temperature of the liquid helium is reduced accordingly [Krö56]. Below a pressure of $40\,\mathrm{mbar}$, Helium undergoes a phase transition and becomes superfluid [Kap38]. Superfluid Helium is transparent for visible and near infra-red (IR) light and free of turbulences. It allows, therefore, to perform optical experiments at temperatures as low as $1.6\,\mathrm{K}$.

3.2.3 Two Laser Setup

As pump and probe pulses stem from the same laser, they have a fixed phase relation. Laser pulses from another laser source running on a different PRF not synchronized to the pump and probe laser would excite the sample but would not leave a direct trace on the probe signal. Even if the pump pulses and the additional pulses are modulated identically for the lock-in amplification and are running on the same optical frequency, the averaging over the measurement time for each delay step in the PP measurement only leaves the contribution of the pump pulse running with a fixed phase to the probe pulse. The contribution of the additional laser pulses is averaged out. This feature is used for the two-laser measurements in Chapter 6, where laser pulses with a PRF of $1\,\mathrm{GHz}$ prepare the NSS, while the time-resolved

Faraday rotation (TRFR) of the ESP in the prepared system is measured using a laser emitting pulses with a PRF of 75.76 MHz.

In the experimental setup, the 1 GHz laser beam is placed parallel (horizontally, on the same level), approximately 1.5 cm, to the 75.76 MHz pump beam such that both beams go through all pump beam optics, especially through the Glan prism and the PEM for the polarization modulation. Both beams hit the lens off-centered horizontally such, that the focal points match. For the data acquisition, the larger the 1 GHz power is set, the larger the additional component (long dephasing component or beating, not shown). Similarly, the best overall signal is achieved when the power of the 75.76 MHz is set such that the best signal for the 75.76 MHz alone appears. To best set it up, one sets a good signal for the 75.76 MHz PP setup. Ideally, the mechanical delay line (DL) is placed to a maximum or minimum of the component which is added due to the 1 GHz excitation. The 1 GHz beam is then directed through the pump path (without changes in the pump path itself) such that the signal after the LI is maximized (minimized).

3.2.4 Resonant Spin Amplification

The setup described above allows to perform additional experiments with a fixed delay but varied external magnetic field. The measurement of resonant spin amplification (RSA) is a tool to determine the dynamics of a sufficiently homogeneous ES system with ES relaxation times $T_{2,\mathrm{e}}^*$ and $T_{2,\mathrm{e}}$ far larger than the PRP in transversal magnetic fields B_x [KA98]. In such a system, the repeated ES orientation leads to amplified, single spin modes, which fulfill the PSC described in Sec. 2.5.1.

The delay between pump and probe pulse is set to a minimal negative delay such that the amplitude of the ESP is probed and not the oscillation phase[2]. Further details can be found in Ref. [HO17, pp. 142–144].

3.2.5 Polarization Recovery Curve

In contrast to the RSA experiments, a polarization recovery curve (PRC) is obtained at a fixed delay close to the next pump pulse (Fig. 3.3(a)) while varying the longitudinal magnetic field B_z.

This technique allows to gain insight into the magnetic field dependence of the interplay between ES orientation and depolarization. In the physical systems and setup studied here, the ES orientation is dependent on the PRF and the pump pulse area Θ (the average pump power). The depolarization is governed by interactions with the NSs via hyperfine contact interaction [MER02], described by the spin-lattice

---

[2]If the probe pulse would be placed further to the center between two pump pulses, the resulting RSA curve would also include the amplitude variation due to the oscillation frequency change when varying B_x.
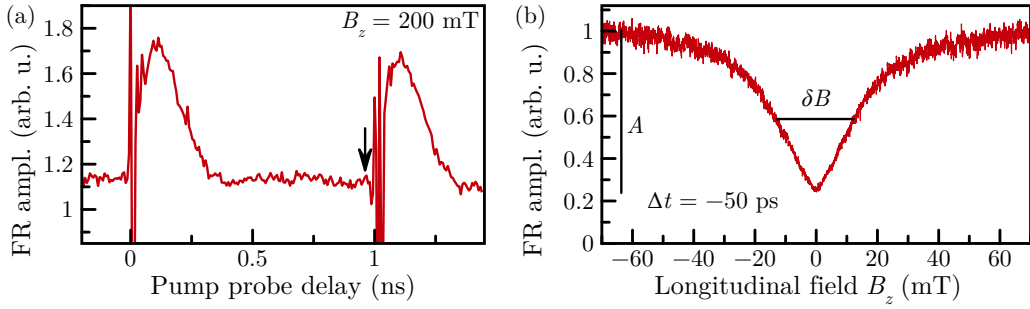
Figure 3.3: Exemplary PRC measurement. (a) The pump probe delay is placed such that the ESP is probed 50 ps before the next pump hits the sample (black arrow). All short lived dynamics, here the trion recombination, decayed and only the long lived dynamics are probed. (b) At a constant pump probe delay, the ESP is measured against the longitudinal magnetic field. The amplitude A is a function of the spin pumping efficiency while the width of the central minimum δB describes the dependence of the interplay of ES orientation and depolarization on the longitudinal external magnetic field.

relaxation time T_1. The general features are shown in Fig. 3.3(b). In longitudinal fields around 0 T, a fluctuating nuclear field leads to depolarization of the ES. The width of this central minimum is a measure for the nuclear field causing the depolarization. Note that the nuclear fluctuating field $\delta B_{\mathrm{N}} = \delta B/2$ can only be extracted for a minimal average pump power as any ES pumping causes an additional widening of the central minimum [SUS19]. At large longitudinal fields, a saturation of the ESP is reached as the influence of the nuclear fluctuating field is suppressed by the larger, static and unidirectional external field. The saturation level is determined by the spin pumping efficiency.

A PRC with the ESP S_z, measured by the FR as shown on Fig. 3.3(b), can be evaluated by [Gre12]

$$S_z(B_z) = A * \left[1 - \frac{R}{1 + \left(\frac{B_z - B_0}{\delta B} \right)^2} \right] + o \tag{3.1}$$

with a possible experimental offset o and a shifted zero field B_0. The parameter R approaches $R = 2/3$ in the case of small average pump powers [SUS19]. Under the right experimental circumstances[3], the PRC can show modulations at purely longitudinal fields that allows the ESP to fulfill the PSC [Sch21]. This allows to trace the RSA curve given by the PSC based on the longitudinal electron g factor. In a titled external field with a small B_x component, by contrast, the transversal g_{e} defines the PSC [Zhu12]. The measurement toolbox described so far can also be applied in the extended pump probe setup described in the next section.

---

[3] An effective hyperfine coupling of ES and NS, and the mode separation in the longitudinal field needs to be small enough to fulfill the PSC in the 0 T field depolarization dip, while also being sufficiently large such that it allows the distinction from one mode to the next.

3.3 Extended Pump Probe Setup

The pump probe setup described in Section 3.2 allows to measure the spin dynamics within 13.3 ns directly. However, the carrier spins in the samples under study are known to have relaxation times far larger [Bec15]. In order to increase the measurable delay between pump and probe pulses, an EPP setup was developed [Bel16].
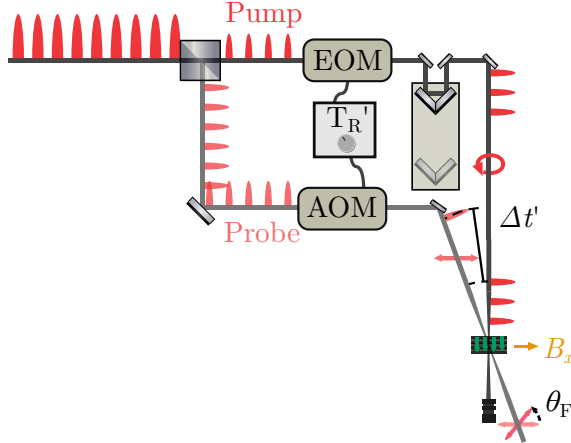

Figure 3.4: Sketch of the extended pump-probe setup. The laser pulse train is split into pump and probe pulse trains. Two pulse selection devices (an electro-optical modulator (EOM) for the pump pulses and a PEM for the probe pulses) allow to introduce a delay $\Delta t'$ between pump and probe pulses larger than the PRP in step sizes of the PRP. Both devices as well as the laser source are electronically synchronized to each other.

Instead of using every single pulse that is emitted by the laser, it is possible to block selected pulses. In a simple version, a pulse picker is used to select single pulses from the original laser train before splitting pump and probe pulses. One pump and one probe pulse hit the sample with a delay set by the DL. The time between such a pump probe pulse pair is defined by the number of pulses blocked between each picked pulse. This scheme can be used to determine the transversal ES relaxation (coherence) time $T_{2,\mathrm{e}}$ in (In,Ga)As/GaAs QDs [Gre06c].

The scheme developed here allows to pick a single probe pulse and a train of pump pulses separately. The pulse emission and the pulse picking for pump and probe pulses is synchronized to each other electronically. The probe pulse is picked by a commercially available pulse picker (acusto-optical modulator (AOM)), while a pump pulse train is picked by an EOM. A schematic working setup is shown on Fig. 3.4. The delay between pump and probe pulses can, hence, be varied by multiples of the PRP by pulse picking. Additionally, the delay can be fine-tuned by the use of the DL and thus allows to access a wide range of delays with a time resolution only limited by the laser pulse duration. A comprehensive pulse arrival diagram is shown on Fig. 3.5(a) with a corresponding EPP curve, see Fig. 3.5(b). Note that several restrictions remain: (i) the PRF should not be larger than 90 MHz as the pulse picker used can not switch fast enough to pick a single pulse, (ii) conversely the PRF should not be smaller than 75.2 MHz as the DL will not cover a whole PRP, and (iii) the separation of the pulse sequences should not exceed a quarter of the modulation period for the LI detection. The last condition limits the maximal measurable delay with the setup as described here to 2.9 μs.

Figure 3.5: Laser pulse sequence for an extended pump probe (PP) measurement. (a) Pulse arrival diagram. The pulses are picked to comprise a pulse sequence period of $T_R^{'}$. Each sequence consists of a pump (Pu) and a probe (Pr) pulse. A single pump pulse is picked at $t^{'}$ and the corresponding probe pulse is picked $2T_R$ later. The DL allows to delay the probe pulse additionally by Δt to an effective delay of $\Delta t^{'}$. (b) The PP curve for kinetics with a relaxation time larger than T_R. Picking another single probe pulse and shifting the DL allows to reach all delays within $T_R^{'}$ and to measure the dynamics with high temporal resolution. The dark red pulse shows the pump pulse while the lighter red dots are measured by the probe pulses colored accordingly in (a).
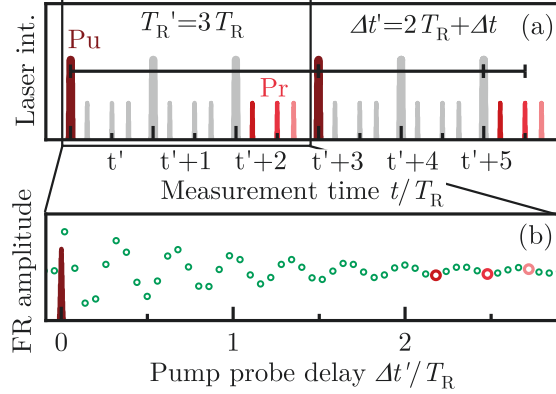
Additionally, the EOM in the pump path enables to select a train of pump pulses, as shown in the scheme on Fig. 3.4. It allows to imprint complex ES precession patterns on the electron spin system [Bel16] as well as to study the build-up dynamics of the ESP [Eve18].

3.4 Radio Frequency Manipulation of Nuclear Spins

While the Larmor frequency for ESs is in the GHz range even for comparably low magnetic fields, the Larmor frequency for NSs is in the MHz range for external fields in the order of 1 T. It is thus accessible by electronics more easily than for electrons and it is viable to use a simple copper coil directly in front of the sample [BES74]. The direct nuclear manipulation allows to either depolarize all nuclei or certain isotopes, or to induce coherent manipulations. Moreover, the ESP is not affected by the MHz RF radiation [Abr83e, p. 394]. The optically build-up nuclear polarization points, on average, along a transverse magnetic field and, as such, changes the Zeeman splitting [Che15] and precession frequency [San06] of hyperfine coupled ESs. As shown on Fig. 3.6, an RF field perpendicular to the external field induces rotations of NSs with a Zeeman splitting resonant to the RF.

The precessing NSP in the Bloch sphere with the state $|\uparrow\rangle$ falling parallel to the external, static field is shown on Fig. 3.6(a). The external field leads to a precession about it, with a constant component along it. In a coordinate system rotating with the Larmor frequency ω_L about the x axis, the NSP is static [RRS54]. A linearly
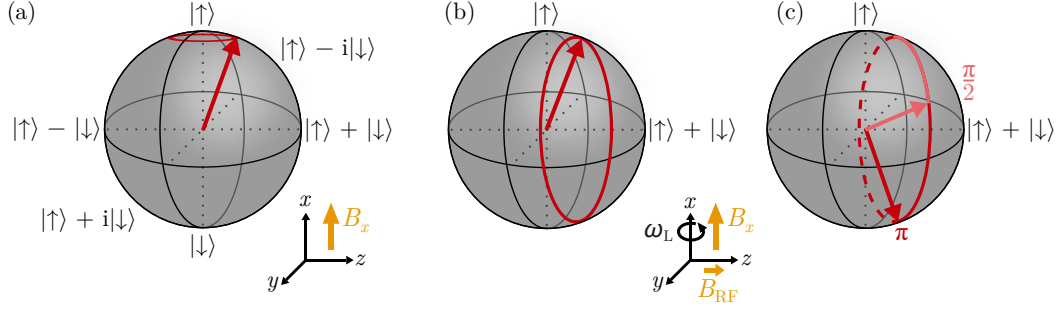
Figure 3.6: Resonant manipulation of the NSS. (a) The NSP precesses about an external magnetic field in x direction (falls along the $|\uparrow\rangle$ state) with the Larmor frequency ω_{L}. (b) A resonant RF field perpendicular to the external field B_x induces a precession about the field B_{RF} in a coordinate system rotating with ω_{L}. It thus changes the component of the NSP along the x axis. (c) The pulse area Θ of a resonant RF pulse determines the tilting angle of the NSP about the z axis. A $\Theta = \pi/2$ pulse tilts the NSP in the yz plane while a π pulse inverts the x component of the NSP.

polarized RF field B_{RF} can be separated in a rotating and anti-rotating field. In the rotating coordinate frame, the anti-rotating component is not resonant to the Zeeman splitting and can be neglected [BS40]. The rotating field is resonant to the Zeeman splitting and is static in the rotating frame. For a properly chosen phase, it points along the z axis and the NSP precesses about it. It leads to a tilt of the NSP towards the yz plane with the angular speed given by the RF field amplitude, and the final tilt angle ϑ is given by the duration of the RF field application. The total tilt angle can exceed a full revolution of the NSP and Rabi oscillations [Rab37], with a frequency Ω_{Rabi}, are observed[4]. The tilt in a Bloch sphere is depicted in Fig. 3.6(b). The final tilt angle

$$\vartheta = \Omega_{\mathrm{Rabi}}t = \gamma B_{\mathrm{RF}}t \tag{3.2}$$

also depends on the reduced gyromagnetic ratio $\gamma/2\pi$ of the specific isotope.

The knowledge of the Rabi frequency for a certain RF power allows one to determine the necessary pulse duration to apply pulses with a defined tilt angle ϑ, and vice versa. π pulses enable one to invert the x component of the NSP, in order to measure the longitudinal spin relaxation time $T_{1,\mathrm{n}}$. RF pulses, which tilt the NSP in the yz plane, allow one to study the transversal NS dynamics and are called $\pi/2$ pulses. These pulses are depicted on Fig. 3.6(c).

As described in Section 2.2, one distinguishes between the spin dephasing and the spin decoherence for the transverse spin dynamics. [5] Ramsey fringes [Ram50], which consist of two $\pi/2$ pulses, allow to measure the dephasing time $T_{2,\mathrm{n}}^*$: The z

---

[4] Rabi oscillations are only observed if the transverse coherence time $T_{2,\mathrm{n}}$ of the NSP is considerably larger than the Rabi period.

[5] Here, the spin dephasing is the loss of total NSP due to the slightly different Larmor frequency

Figure 3.7: Pulse protocols for different coherent RF measurements. Rabi oscillations are induced by pulses of varied duration (dashed line). The derived pulses for measuring the longitudinal relaxation, Ramsey fringes and a Hahn echo sequence are shown, with the times to derive the NS dephasing time τ_{12} and the NS coherence time τ_{13} depicted on the x axis.
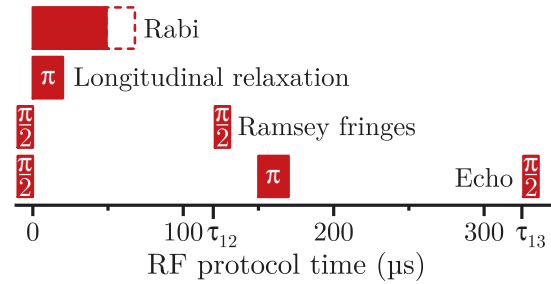
component of the NSs is tilted in the yz plane by the first pulse and the individual spins precess with their respective (transverse) Larmor frequency. After a time τ_{12}, the second $\pi/2$ pulse tilts the remaining total yz components back to the x axis. [6] The RF protocol of the Ramsey fringes is shown on Fig. 3.7.

The spin coherence time $T_{2,n}$ is determined by applying a Hahn echo sequence [Hah50]. As for the Ramsey fringes, a $\pi/2$ pulse tilts the x component of the NSP in the yz plane. The NSs dephase, but a π pulse inverts the NSs like they were mirrored at the xz plane. NSs with a higher Larmor frequency precessed further, but after a time equal to the time between the first $\pi/2$ pulse and the π pulse, the NSP is in phase again, as the NSs with a higher Larmor frequency also have a larger angle to cover to the original position. At this time, the rephased NSP is tilted back to the x axis by a $\pi/2$ pulse. The total NSP is reduced only by the loss of coherence of the individual NSs as the dephasing has been reversed. Hence, the coherence is measured over the time between the two $\pi/2$ pulses τ_{13}. The RF Hahn echo protocol is also shown on Fig. 3.7.

3.4.1 Experimental Realization

A scheme for the application of transverse RF fields in the experiment is shown on Fig. 3.8(a). The RF is applied by a pulsed RF amplifier, which enables to induce a field in the sample by a small diameter copper coil, mounted 1 mm in front of the sample, for pulse lengths of up to 60 ms. The RF field is estimated by the Rabi oscillation frequency (see Sec. 3.4). Long pulses with a spectral width of 100 kHz allow one to determine the resonant frequencies in the sample. An exemplary

---

transverse to the magnetic field and subsequent randomization of the individual NS orientation. The individual NSs keep their individual phase and the original state can, in principle, be restored. Only when all individual phase information is lost, the original state can not be restored and the NSs lost coherence.

[6] The remaining x component of the total NSP determines the effective magnetic field about which the ESP precesses. Note also, that the longitudinal NS relaxation time is orders of magnitude larger than all transverse spin relaxation times and times necessary to measure the ESP in the studied systems [Eve19]. Therefore, the transverse spin relaxation is preserved for the measurement once tilted back to the x axis.
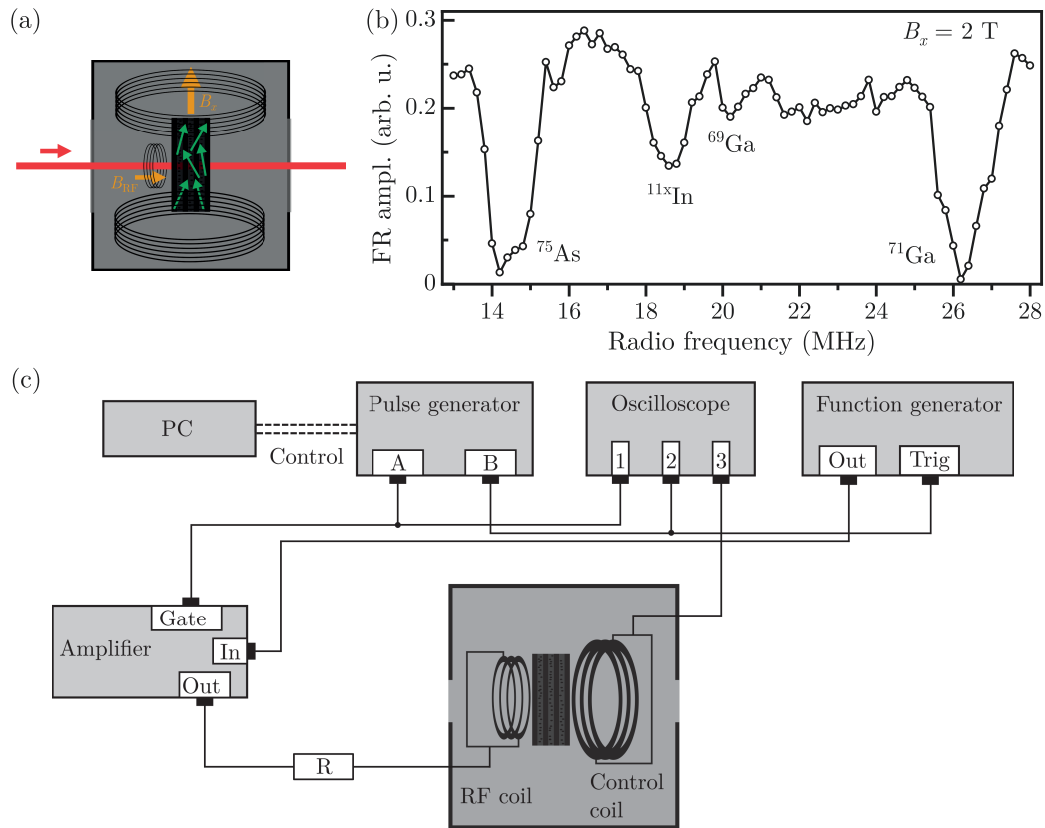
Figure 3.8: Radio frequency setup and typical RF spectrum. (a) Scheme of the coils for the direct manipulation of NSs using RF manipulation. In Voigt geometry, with a large transverse magnetic field B_x, an additional coil is mounted in front of the sample to add a longitudinal RF field B_{RF} of several mT. It serves to rotate the NSs (green arrows) about the external field axis (x axis). (b) RF spectrum of an (In,Ga)As/GaAs QD ensemble. The FR amplitude depends on the nuclear polarization in each QD. Long RF pulses with a matching frequency to the nuclear Zeeman splitting at $B = 2\,\mathrm{T}$ depolarize the NSs. All constituent isotopes can be addressed. (c) Electrical setup for the application of pulsed NMR. The pulse generator acts as a clock, that synchronizes the function generator and the pulsed amplifier to ensure that phase-stable pulses reach the RF coil. The ohmic resistor R serves as a primitive tool to flatten the frequency dependence of the coil reflection. The induced RF signal is picked up by the control coil.

spectrum for an (In,Ga)As/GaAs QD ensemble is shown on Fig. 3.8(b). In the configuration used here, the FR amplitude depends on the NSP. The application of resonant RF fields equalizes the population of the NS levels, thus depolarizes the NSs, and the FR amplitude is reduced [Eve18, App.]. This RF application setup allows one to address all central nuclear transitions individually, but a long pulse covering all NMR frequencies depolarizes the whole NSS. It allows for measurements with suppressed NSP influence as used in Sec. 5.2. The application of a narrow band, RF pulse sequence, however, allows one to determine the NS dynamics as applied in Chap. 4.

The detailed electric setup for the application of RF pulse sequences is shown in Fig. 3.8(c). The pulse generator triggers both the *Gate* of the RF pulse amplifier as well as the function generator with the same pulse sequence delayed by $10\,\mu s$ between the outputs A and B (B before A). The function generator either sends out a previously calculated Fourier transform of a flat frequency band, with a fixed width and central frequency, or a nearly single frequency sine. The implementation of the broadband RF application is detailed in Appendix A. The fixed delay between the trigger of the function generator and the amplifier ensures a fixed starting phase of the induced RF pulses. The amplifier gives out the RF pulses via an ohmic resistance R, which smooths the frequency dependence of the coil reflectivity. From the observed Rabi frequency Ω_{Rabi} measured in the experiments (see Sec. 4.4), an achievable field of $B_{\mathrm{RF}} = 10\,\mathrm{mT}$ can be estimated using Eq. (3.2). A control coil mounted behind the sample picks up the induced RF fields and allows one to monitor the RF pulses on a multi channel oscilloscope triggered by the pulse generator.

3.5 Samples Under Investigation

All samples studied in this work are negatively charged, low-dimensional semiconductors.

3.5.1 InGaAs/GaAs Quantum Dot Samples

The experiments in Chapter 6 are performed on sample #11955-945. The sample #11955-945, grown in year 2004, is build up of 20 layers of (In,Ga)As/GaAs QDs, each separated by 80 nm layers of GaAs. The layers are grown by MBE on (100)-oriented GaAs substrate. The admixture of In reduces the band gap compared to GaAs. Moreover, InGaAs is lattice mismatched to GaAs. Following Stransky-Krastanov growth, islands of InGaAs quantum dots form due to the aforementioned lattice mismatch and are subsequently homogenized by thermal annealing at a temperature of 945 °C. This also shifts the central emission to 1.391 eV (891.5 nm). Each QD consists of 1×10^5 atoms on average and the density of each layer amounts

to $1 \times 10^{10}\,\mathrm{cm}^{-2}$. A δ doping layer of Si is grown 16 nm below each QD layer and leaves each QD singly charged on average.

The sample is well-known and it is the same sample as used in Refs. [Gre06b; Gre06c; Gre07; Her08; GYB09; Gre09]. Previous works found a number of properties that are listed in table 3.1. The value of the g factor for a given trion resonance energy E_{Tr} follows a linear dependence [RLZ59] and is described by [Yug09]

$$g(E_{\mathrm{Tr}}) = -1.75\,\mathrm{eV}^{-1} * E_{\mathrm{Tr}} + 2.99 \quad , \tag{3.3}$$

which falls in line with the results obtained later in this work.

Table 3.1: Parameters of the ENSS in this QD sample. The parameters are known from previous publications as indicated for every parameter. Δg_{e} is the electronic g-factor spread, δB_{N} the nuclear fluctuations acting on the ESs, $T_{2,\mathrm{e}}$ the electron spin coherence time, τ_{Tr} the trion recombination time, and $T_{1,\mathrm{n}}$ the NS relaxation time.

Δg_{e} [Gre09]	δB_{N} [Gre09]	$T_{2,\mathrm{e}}$ [Her08]	τ_{Tr} [Gre06b]	$T_{1,\mathrm{n}}$ [Gre07]
$0.0018\,\mathrm{meV}^{-1}$	$7.5\,\mathrm{mT}$	$800\,\mathrm{ns}$	$0.4\,\mathrm{ns}$	$> 15\,\mathrm{min}$

The sample #14056a-880 strongly resembles sample #11955-955 but is grown with 60 nm-thick layers of GaAs between the QD layers. Moreover, the sample has been annealed at a temperature of 880 °C. The ensemble is also singly negatively charged on average. The central trion energy is shifted to 1.373 eV (903 nm).

3.5.2 CdTe/CdMgTe Quantum Well Sample

The CdTe QW #031901C studied in Chapter 4 is a MBE grown CdTe/Cd$_{0.78}$Mg$_{0.22}$Te heterostructure. The admixture of Mg raises the bandgap compared to pure CdTe. The base of the heterostructure is given by a (100) oriented GaAs substrate. On top of the substrate, a thick 2 μm Cd$_{0.78}$Mg$_{0.22}$Te buffer layer is grown, followed by a CdTe/Cd$_{0.78}$Mg$_{0.22}$Te superlattice. Five QW layers are stacked on top of the supperlattice, and each layer consists of a 110 nm-thick Cd$_{0.78}$Mg$_{0.22}$Te barrier and a 20 nm-thick CdTe layer. To reduce the influence of surface charges, an additional barrier of 110 nm thickness is grown on top of the five barrier-QW periods. Excess electrons are offered to the CdTe layer by doping the barriers with Iodine donors and lead to the formation of a two-dimensional electron gas with a density of $n_{\mathrm{e}} = 1.1 \times 10^{10}\,\mathrm{cm}^{-2}$. The resident electrons lead to the possible formation of a negative trion state, shifted to the lower energy from the free exciton state by the additional binding energy. Finally, the GaAs substrate was chemically removed in order to enable optical transmission experiments and the remaining sample is embedded in SiO$_2$ (Silicon dioxide or silica) to stabilize it.

4 Optically Detected Nuclear Magnetic Resonance in CdTe Quantum Wells

The hyperfine interaction also allows one to study the ENSS dynamics in a 2D CdTe QWs. While the NS dynamics in GaAs QWs is well studied [San06], there are some key differences to the QWs studied here: (i) All nonzero NS isotopes in CdTe have a spin $1/2$, while all nonzero NS isotopes have a spin $3/2$ in GaAs. Therefore, no intrinsic quadrupole interaction, which leads to an additional NS relaxation [Urb13], is present in the sample studied here and only one NMR transition per isotope has to be considered. (ii) Prominent works are realized in a tilted external field[1] in order to increase the sensitivity [San06] or to maximize the achievable Overhauser field [Moc17]. Here, a weak NSP suffices to study the NSP enabled by the frequency resolution of the ES precession with its 8 ns long dephasing time [Zhu07].

The chapter starts by detailing the optical setup and sample in Sec. 4.1. In Sec. 4.2, the ES-NS interaction relevant for this sample is discussed and the detection of the NSP by the ESP is elucidated. Detecting the NSP allows one to determine the NMR frequencies of the present nuclei in Sec. 4.3. For each isotope, coherent RF manipulation is demonstrated in Sec. 4.4 by inducing Rabi oscillations. To quantify the NSP relaxation, the longitudinal relaxation time $T_{1,\mathrm{n}}$ is identified in Sec. 4.5, the transversal dephasing time $T_{2,\mathrm{n}}^*$ in Sec. 4.6, and the transversal relaxation time $T_{2,\mathrm{n}}$ in Sec. 4.7. Finally, the results are concluded in Sec. 4.8.

The results presented in this chapter have been published in Ref. [Eve19].

4.1 Optical Setup and Basic Sample Characterization

The NSP is studied by its effect on the ES precession frequency. The ES-NS interaction is mediated via collinear, Fermi contact hyperfine interaction [Fli90]. The NSP acts as OF on the ESP and thus modifies the effective field. Consequently, the ESP precession frequency changes depending on the sign of the OF. Here, the precession frequency is determined by a PP setup as described in Sec. 3.2.2 with the sample placed in a magneto-cryostat. The external field is applied perpendicular to the light propagation and sample growth axis (Voigt geometry). A single 75.76 MHz Ti:Sapphire laser is used for both pump and probe pulses and is set to a central energy of $E_{\mathrm{Pu}} = E_{\mathrm{Pr}} = 1.5986\,\mathrm{eV}$ (775.6 nm), with a FWHM of 1.5 meV (1 nm). A

---

[1] The external field is not perpendicular to the light incidence and to the QW growth direction.

mechanical shutter right behind the laser enables to switch the illumination on and off within 5 ms and enables to observe the NSP with continuous pulsed excitation or in darkness. The average power in front of the cryostat amounts to $P_{\text{Pu}} = P_{\text{Pr}} = 0.6\,\text{W}$ (power density $D_{\text{Pu}} = D_{\text{Pr}} = 48\,\text{W cm}^{-2}$). The ESP is determined by the evaluation of the FE. For all measurements, the sample temperature is set to $T = 1.5\,\text{K}$.
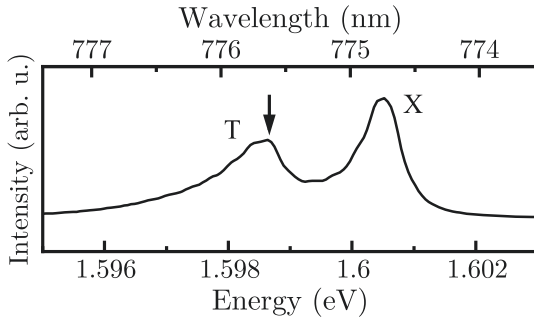

Figure 4.1: PL of the CdTe/CdMgTe-QW sample at $T = 6\,\text{K}$. Two lines are present: the exciton (X) and the negative trion (T) line. The central laser energy is placed on the T line, as indicated by the black arrow.

In order to initialize a significant ESP, the route via the spin polarization dependent trion excitation as given in Sec. 2.2.1 is pursued. An electron of the two-dimensional electron gas in the QW can form a trion with the photo-excited exciton[2]. The excitation with circularly polarized light binds electrons with one spin orientation in the trion and leaves the other free, thus creating a total spin polarization in the electron gas [Zhu10]. This can be realized by the resonant excitation of the trion. The PL after excitation with a 532 nm cw laser is shown in Fig. 4.1 and allows one to identify the exciton (X) and the negative trion line (T). The additional binding energy shifts the trion energy towards lower energies compared to the exciton energy [Zhu07].

Furthermore, the electron g factor is determined to $g_{\text{e}} = -1.64$ by analyzing the ES Larmor frequency at an external field of $B_x = 1\,\text{T}$ (see Fig. 4.2), which matches the electron g factor for pure CdTe QWs found previously [Sir97]. Further detailed studies on the sample revealed the ES dephasing time dependence on the external field, the temperature, and the excitation power density as well as the hole spin relaxation time in the trion [Zhu06; Zhu07; Ast08].

4.2 Optical Traces of the Nuclear Spin Polarization

In general, the ES is excited with a train of laser pulses such that the NSP reaches a steady state and the ES precesses about the local magnetic field which consists of the external field B_x and the OF B_{N}. The origin of the NSP is illustrated by the following considerations. The population difference in thermodynamic equilibrium

---

[2]The electron density $n_{\text{e}} = 1.1 \times 10^{10}$ cm^{-2} is low enough, so that the Fermi energy is smaller than the exciton binding energy [Zhu07].

resulting from the Boltzmann distribution only leads to a degree of NSP of less than $0.02\,\%$ at $T = 1.5\,\mathrm{K}$ and $B_x = 1\,\mathrm{T}$[3] and, therefore, DNP has to be considered as the observed degree of NSP exceeds that by two orders of magnitude. However, alternating the polarization of the pump pulses between σ^+ and σ^- with the frequency $\nu_{\mathrm{Mod,Pu}} > T_{2,\mathrm{n}}{}^{-1}$ ($T_{2,\mathrm{n}} \approx 2.5\,\mathrm{ms}$ shown below), as used here, reportedly prevents the build up of a sizable NSP [FM84, p. 201] in Faraday geometry (external field along optical axis). Moreover, the sample excitation in pure Voigt geometry (perpendicular to the light propagation along z) does not lead directly to an ES **S** component along the external field. Only this component polarizes a NSP **I** along the external field via collinear hyperfine interaction $A\mathbf{I} \cdot \mathbf{S}$ (with the hyperfine constant A) [Dya17, p. 5]. The NSP could, however, originate from noncollinear hyperfine interaction, namely quadrupole interaction [FM84, p. 224], but all nuclei in the sample possess a NS $|\mathbf{I}| = {}^1\!/_2$, and therefore do not have a quadrupole moment [Hay12]. An optical excitation, detuned from the trion resonance in an even slightly inhomogeneous ensemble, can introduce an optical Stark field, which acts like a field in the light propagation direction. As described for self-assembled QDs in Sec. 2.5.2, the optical Stark effect can lead to a NSP via collinear hyperfine interaction [Ber08]. The origin of the optical detuning could lie in the broad laser spectrum of $1.5\,\mathrm{meV}$, which introduces an optical detuning even if the central energy matches the narrow central trion resonance. Despite the modulated excitation, this could lead to a sizable NSP as the direction of the established NSP only depends on the sign of the optical detuning, but not on the sign of the circular polarization of light [Car09].

The effect of the NSP on the ESP is clearly seen in Fig. 4.2. The black trace shows the PP trace of the ESP measured by FE in a steady state NSP. The ESP precesses with a single frequency. After applying a single, resonant RF π pulse, the frequency changes as the OF is inverted (red trace). This results in a shifted precession phase on a given PP separation. Therefore, the phase shift serves as an indicator for the NSP. To register the phase shift, a small section of the precession is registered before and after the application of RF fields.

For the exemplary data given in Fig. 4.2, one can calculate the OF change ΔB_{N} on the ES induced by the RF by

$$\Delta B_{\mathrm{N}} = \frac{h\nu}{g_{\mathrm{e}}\mu_{\mathrm{B}}} \left(1 - \frac{t_0}{t_0 + d}\right) \tag{4.1}$$

---

[3] The degree of NSP is calculated by [Blü19, p. 145]

$$\frac{n_- - n_+}{n_- + n_+} = \frac{1 - \exp\left(-\frac{\gamma}{2\pi}\frac{hB_x}{k_{\mathrm{B}}T}\right)}{1 + \exp\left(-\frac{\gamma}{2\pi}\frac{hB_x}{k_{\mathrm{B}}T}\right)}$$

with the population of the NS state higher (lower) in energy n_+ (n_-), the gyromagnetic ratio $\gamma_{{}^{125}\mathrm{Te}}$, the Planck constant h, and the Boltzmann constant k_{B}. The gyromagnetic ratio of ${}^{125}\mathrm{Te}$ is larger than that of ${}^{111}\mathrm{Cd}$ and ${}^{113}\mathrm{Cd}$ and, therefore, gives the largest possible degree of NSP.
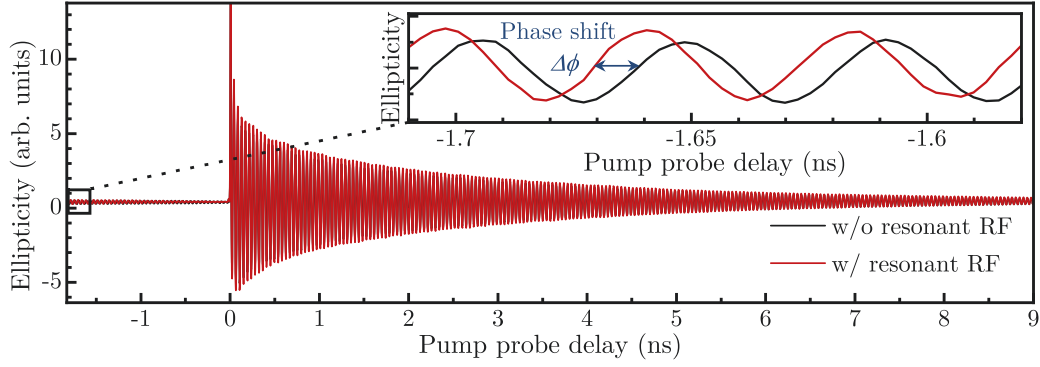
Figure 4.2: Influence of the resonant RF on the PP signal. The black trace shows the ES precession in an external field $B_x = 1\,\text{T}$. A resonant RF pulse changes the total NSP and, thus, the OF and the effective magnetic field (red trace). The resulting frequency change leads to a phase shift evaluated after $11.5\,\text{ns}$ (blue arrow).

with the Planck constant h, the precession frequency ν and the delay t_0 at a given cumulated precession phase in the steady ENSS (x axis position of the blue arrow on the black trace), the delay difference d to the same cumulated phase in the ES precession after the application of RF (x axis position of the blue arrow on the red trace), and the electron g factor $g_\text{e} = -1.64$. Alternatively, the OF can be calculated using the phase shift $\Delta\phi$ as

$$\Delta B_\text{N} = \frac{h}{g_\text{e}\mu_\text{B}t_0}\frac{\Delta\phi}{2\pi}\quad. \tag{4.2}$$

The change in OF amounts to $\Delta B_\text{N} = 0.81\,\text{mT}$ or $1.2\,\%$ of the maximal OF $B_\text{N,max} = 69\,\text{mT}$. The maximal OF is calculated using the values in Tab. 4.1 according to Eq. (6.3).

Table 4.1: Basic properties of present isotopes. For the three isotopes ^{111}Cd, ^{113}Cd, and ^{125}Te, the NS magnitude $|\mathbf{I}|$ [Hay12], the natural abundance a_nat [Hay12], the reduced gyromagnetic ratio $\gamma/2\pi$ [Hay12], and the electron-nuclear hyperfine constant A is given. Additionally, the maximal OF for each isotope in a CdTe QW is given according to Eq. (6.3).

Isotope	$|\mathbf{I}|$	a_nat	$\gamma/2\pi\left[\frac{\text{MHz}}{\text{T}}\right]$	$A\,[\mu\text{eV}]$	$B_\text{N,max}\,[\text{mT}]$
^{111}Cd	$^1/_2$	$13\,\%$	-9.07	$-37\,$[Syp11]	25
^{113}Cd	$^1/_2$	$12\,\%$	-9.49	$-39\,$[Syp11]	25
^{125}Te	$^1/_2$	$8\,\%$	-13.5	$-45\,$[Tes09]	18

Figure 4.3: NMR spectrum of the contributing nuclei. RF pulses with a spectral width of 100 kHz around the central frequency lead to sharp oscillation phase changes of the ESP precession. All constituent isotopes are resolved. The line is a guide to the eye.
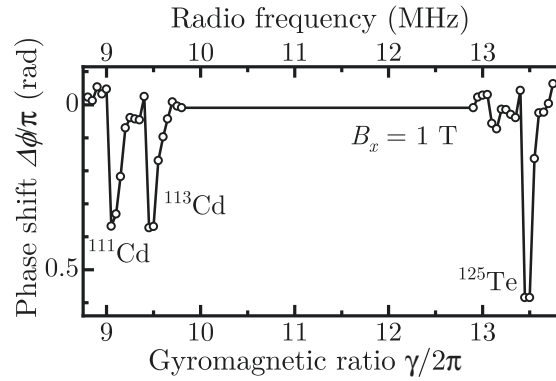
4.3 Spectrum of Contributing Nuclei

Instead of using spectrally broad RF fields which depolarizes all nuclei, the contribution of each isotopes NSP is identified by applying long, spectrally narrow RF pulses. For a width of 0.1 MHz the contributing isotopes show up and are clearly separate (see Fig. 4.3). The resonant NMR frequencies at $B_x = 1$ T are determined to $\nu_{\mathrm{NMR},^{111}\mathrm{Cd}} = 9.05$ MHz, $\nu_{\mathrm{NMR},^{113}\mathrm{Cd}} = 9.47$ MHz, and $\nu_{\mathrm{NMR},^{125}\mathrm{Te}} = 13.48$ MHz in agreement with the reported values in Tab. 4.1. The asymmetry of the peaks is a result of the (too) short time interval between subsequent RF applications which does not allow the NSs to reach a steady state polarization[4]. The signature of both cadmium (Cd) isotopes reaches only a magnitude of two thirds of the ^{125}Te signature although the abundance of ^{125}Te is only $a_{\mathrm{nat}} = 8\,\%$ whereas the abundance of both Cd isotopes is close to $a_{\mathrm{nat}} = 12\,\%$ and the hyperfine constant A is similar. The natural abundance directly reflects the nuclei, that were present in the sample, as the ratio of Cd to tellurium (Te) is 1:1 in the primitive cell. As shown in Sec. 4.5, the difference in magnitude reproduces the difference in OF exerted on the ESs in the steady state ENSS.

4.4 Radio Frequency Induced Nuclear Spin Rabi Oscillations

In a second step, resonant RF pulses are applied using the pulse generator and the RF pulse amplifier described in Sec. 3.4.1. A set of single frequency pulses resonant to each of the three isotope frequencies with varying power and duration allows one to trace Rabi oscillations. With increasing pulse area Θ, the NSP tilting angle ϑ increases. After every pulse, the NSP is determined by observing the phase shift $\Delta\phi$ of the ES precession. Exemplary Rabi oscillations for the resonant frequency to ^{125}Te are shown in Fig. 4.4. For a fixed voltage of 250 mV, a fit with a single, exponentially damped sine function yields a Rabi frequency of $|\Omega_{\mathrm{Rabi}}| = 0.5\,\mu\mathrm{s}^{-1}$.

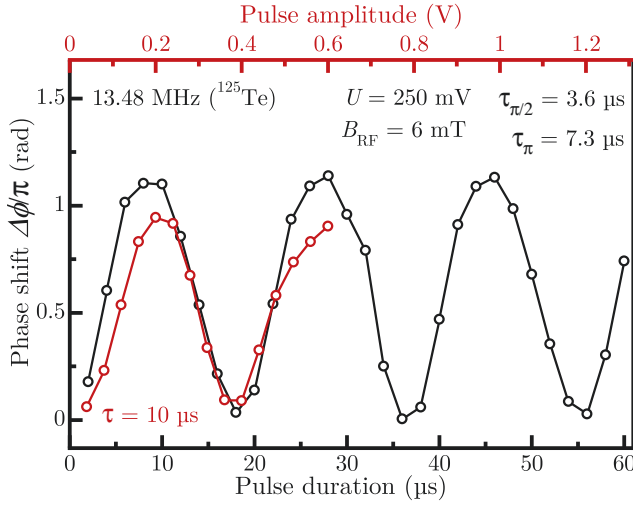[4]The scanning direction is from low to high frequencies.

Figure 4.4: Rabi oscillations of the NSP. The ES precession phase shift $\Delta\phi$ due to the OF change is plotted against the RF pulse duration at a voltage of $U = 250\,\text{mV}$ (black, bottom axis) and the RF voltage at a pulse duration of $\tau = 10\,\mu\text{s}$ (red, top axis). The Rabi frequency Ω_{Rabi} is determined by fitting a damped sine for $U = 250\,\text{mV}$, and allows one to determine the RF field B_{RF} and the times τ_{π} and $\tau_{\pi/2}$ for the coherent Ramsey fringes and Hahn echo experiments.

Using Eq. (3.2), the RF field is calculated to $B_{\text{RF}} = 6\,\text{mT}$. Moreover, the knowledge of the Rabi frequency gives the necessary pulse duration for the pulses of a pulse area $\vartheta = \pi$ and $\vartheta = \pi/2$, as used in the coherent Ramsey fringes and Hahn echo sequences (see Sec. 3.4). As a reminder, after tilting by an angle $\vartheta = \pi/2$, the NSP component formerly directed along the external field B_x points perpendicular to B_x, along the y axis. Tilting by an angle $\vartheta = \pi$ leads to the inversion of the NSP component formerly directed along B_x. The pulse duration at constant power for these pulses is determined for the three isotopes and given in Tab. 4.2.

Isotope	RF voltage	$\pi/2$ pulse	π pulse
^{111}Cd	650 mV	2.2 µs	4.4 µs
^{113}Cd	650 mV	2.2 µs	4.5 µs
^{125}Te	250 mV	3.6 µs	7.3 µs

Table 4.2: Specific pulse areas determined by Rabi oscillations for the contributing isotopes.

4.5 Longitudinal Depolarization Time

The polarization time is measured using a single RF π pulse that inverts the NSP along the x axis. Subsequently, the ES precession phase is observed as the NSs depolarize. The depolarization for each isotope is registered in two configurations: In the first one, the sample is kept in darkness after the steady state ENSS is reached, especially during the NS depolarization after the application of the single π pulse, and the laser pulses are only opened afterwards for tracing the ES precession. In the second configuration, the mechanical shutter is left open and the ESs are excited by laser pulses during the NS depolarization. As the π pulse inverts the NSP along the external field, the change in OF induced by the RF pulse allows one to determine

Figure 4.5: Depolarization of ^{111}Cd after NSP inversion by a single RF π pulse at an external field of $B_x = 1\,\text{T}$ and a temperature $T = 1.5\,\text{K}$. The phase shift of the ES precession is shown against the time after the application of the RF pulse. The ENSS is left in darkness until the PP measurement. The longitudinal relaxation time is determined by a single exponential fit.
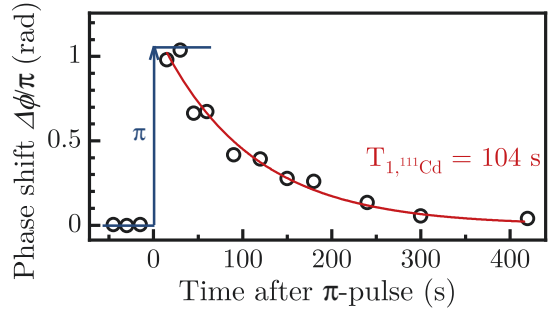
the NSP in the steady state ENSS for each isotope. The change in OF ΔB_N is calculated from the phase shift $\Delta\phi$ using Eq. (4.2) and translates to the actual OF by $B_\text{N} = {}^{\Delta B_\text{N}}/_2$. The resulting OF for each isotope is given in Tab. 4.3. An exemplary depolarization measurement is given in Fig. 4.5. The resulting OF of the different isotopes reflect the amplitudes found in Fig. 4.3. The maximal fraction of the maximal OF is reached by ^{125}Te with 9.7 % and, together, the NSP is polarized to 6.8 %. This is significantly lower than the 37 % determined for the technique used in Ref. [San06] for GaAs QWs and therefore allows to study the NSP dynamics in a weakly perturbed system. Moreover, the option to block the sample illumination during the longitudinal NS relaxation ensures a minimal perturbation by the ESP.

Figure 4.6: Longitudinal depolarization time $T_{1,\text{n}}$ with (red) and without illumination (black) of the sample during the RF application for the example of ^{125}Te. The phase shift due to NSP is plotted against the time after a single π pulse. The results with illumination are fitting with a double exponential decay, whereas the results in darkness are fitted with a simple exponential decay as the short decay already vanished before the first data point is taken.
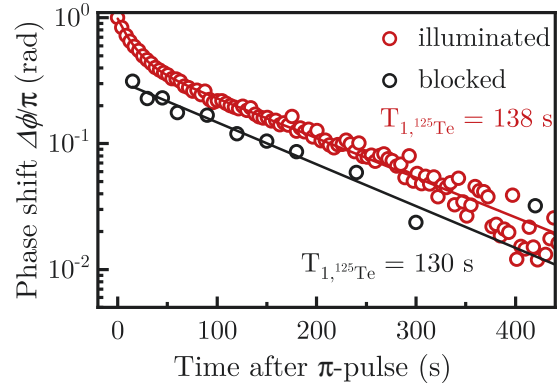
To determine the NSP depolarization time, the ES precession phase shift is plotted against the time after the application of the π pulse, as shown in example in Fig. 4.6. For the measurement with persistent pump pulses, a double exponential fit is used, as a fast decay was observed which already vanished before the first measurement when keeping the sample in darkness. Hence, this data is fitted with a simple exponential decay. The resulting polarization times are shown in Tab. 4.3. Exemplary data for the comparison between the dynamics in darkness and under pulsed illumination in the case of ^{125}Te is shown in Fig. 4.6. Strikingly, the longitudinal relaxation is significantly slower in illumination for both Cd isotopes but nearly unchanged for

Table 4.3: Isotope specific NSP and NS depolarization time at $B_x = 1\,\text{T}$ and $T = 1.5\,\text{K}$. The isotope specific OF contribution to the steady state ENSS is given together with the fraction of the maximal OF for that isotope. Additionally, the depolarization (longitudinal relaxation) time $T_{1,\text{n}}$ for each isotope when kept in darkness and when illuminated with pump pulses is compared.

Isotope	B_{N} [mT]	$B_{\text{N}}/B_{\text{N,max}}$	$T_{1,\text{n}}$ [s] dark	$T_{1,\text{n}}$ [s] illuminated
^{111}Cd	1.5	6.0 %	104	173
^{113}Cd	1.4	5.5 %	116	169
^{125}Te	1.8	9.7 %	130	138

^{125}Te. Further reasoning on these differences is given in Sec. 4.8.
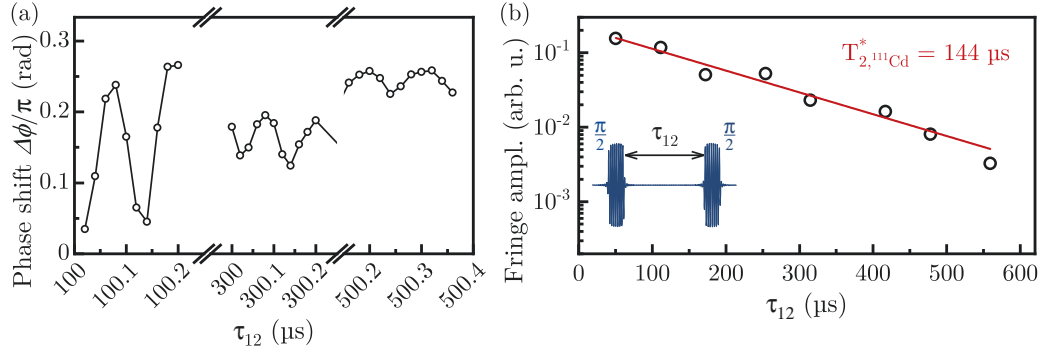
4.6 Nuclear Spin Polarization Dephasing Time

Figure 4.7: Determining the dephasing time for the NSP of an isotope species, here ^{111}Cd, at $B_x = 1\,\text{T}$ and $T = 1.5\,\text{K}$. (a) The phase shift of the ES for different pulse separations τ_{12} in fine resolution for three larger separations. Each dot represents the phase shift of the ES precession relative to the steady state ENSS. A single sine function is fitted to the signal in each section. The frequency of the fitted sine reflects the NSP precession frequency in the external field B_x and the amplitude gives the fringe amplitude. (b) The fringe amplitude is plotted against the pulse separation τ_{12}. Fitting with a single exponentially decaying function yields the dephasing time $T_{2,\text{n}}^*$.

The NSP dephasing time $T_{2,\text{n}}^*$ for each isotope is determined by applying Ramsey fringes. The NSP dephasing could emerge from differences in the five QW layers or from strain induced differences between NSs close to the QW edge and in the center of it. Ramsey fringes consist of two resonant $\pi/2$ pulses with a free evolution time τ_{12} of the NSP in between them [Ram50]. The first pulse leads to the tilting of the NSP along the y axis and the second pulse reorients the NSP along the x axis. The total NSP along x after the second pulse depends on the (transversal) dephasing of the individual spins to eachother during τ_{12} and allows one to determine the NS dephasing time as a NS ensemble effect (for details see Sec. 3.4). This measurement is facilitated by the 100 seconds long longitudinal relaxation time for all isotopes, as the NSP can be considered constant after the NSP is tilted back along the external field.

The dephasing time is identified by gathering data in three steps: (i) For each pulse separation τ_{12}, the ES precession phase is determined by the PP trace over two oscillation periods of the ES precession. (ii) To quantify the remaining total NSP, the ES precession phase is determined within a single NS precession about the external field (see Fig. 4.7(a)) by scanning the separation time τ_{12} in fine resolution. Each NSP precession period is fitted with a single sine function as well. The frequency gives the precession frequency of the total NSP about the external field and matches the frequency determined by the gyromagnetic ratio $\gamma/2\pi$ (see Tab. 4.1). (iii) The amplitude of each precession period (fringe amplitude) is plotted against

the separation time with a coarse separation time resolution as thousands of NSP revolutions fit within the identified NSP dephasing time. The fringe amplitude is plotted against the pulse separation τ_{12} in Fig. 4.7(b). An exponential fit to the fringe amplitude then yields the dephasing time $T_{2,n}^*$.

The measurement procedure is repeated for the remaining two isotopes using Ramsey fringes with their respective resonant RF frequency and under constant pulsed illumination as well. The resulting NSP dephasing times are given in Tab. 4.4. Similar to the results in Sec. 4.5, the constant, pulsed excitation and ES polarization

Isotope	$T_{2,n}^*$ dark	$T_{2,n}^*$ illuminated
^{111}Cd	144 µs	366 µs
^{113}Cd	191 µs	446 µs
^{125}Te	200 µs	200 µs

Table 4.4: Isotope specific NSP dephasing times in the absence of repeated ES polarization (darkness) and under constant pulsed illumination at $B_x = 1\,\mathrm{T}$ and $T = 1.5\,\mathrm{K}$.

significantly slows down the NSP dephasing for both Cd isotopes, but leaves the ^{125}Te NS dynamics unchanged. This will be discussed further in Sec. 4.8.

4.7 Nuclear Spin Coherence Time

In contrast to the NS dephasing time due to the dephasing in the total NSP, the decoherence time describes the loss of phase information of a single NS. In order to revert the NSP dephasing, a Hahn echo sequence is applied by adding a rephasing π pulse in the middle between the two $\pi/2$ pulses [Hah50] (for details see Sec. 3.4). As described in Sec. 4.6, the NS coherence time $T_{2,n}$ is determined in a three step process, which only differs in the applied RF pulse sequence. The measurements are also performed for all three present isotopes as well as in darkness and under constant pulsed illumination during the application of the RF sequence. The identification of the NS coherence time for ^{111}Cd in darkness is illustrated in Fig. 4.8(a) and (b). In

Isotope	$T_{2,n}$ dark	$T_{2,n}$ illuminated
^{111}Cd	2.5 ms	2.9 ms
^{113}Cd	2.6 ms	4.6 ms
^{125}Te	2.6 ms	3.8 ms

Table 4.5: Comparison of the NS coherence time $T_{2,n}$ for different isotopes when kept in darkness and when illuminated with pump pulses during the application of the RF sequence.

comparison to GaAs QWs, the NS coherence time is elongated tenfold ($T_{2,n} = 270\,\mathrm{\mu s}$ for the ^{71}Ga central transition [San06]). This may reflect the increased NS relaxation facilitated by the quadrupole interaction with charge carriers [PAK08].

To illustrate the different NS coherence times in darkness and under pulsed illumination, the decay of the Hahn echo amplitude is shown in Fig. 4.9, for the example of ^{125}Te. The increase of the NS coherence time in the studied CdTe QWs under pulsed illumination is discussed in the following section.
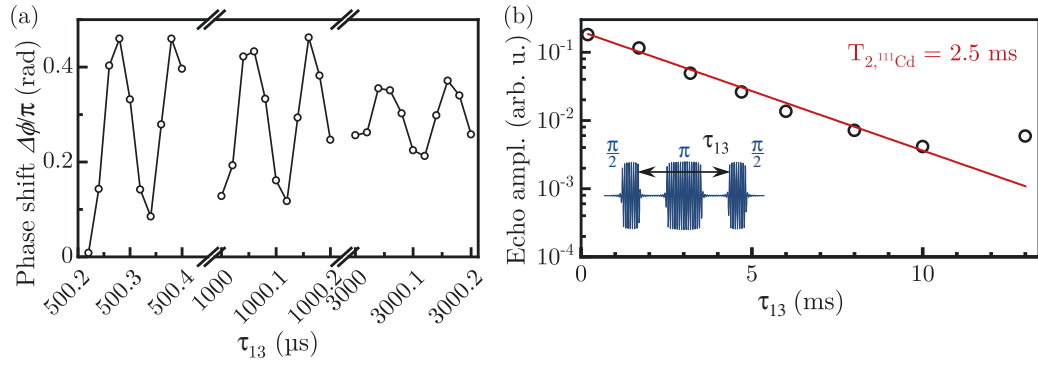
Figure 4.8: NS coherence time measurement using a RF Hahn echo sequence for ^{111}Cd at $B_x = 1\,\text{T}$ and $T = 1.5\,\text{K}$. (a) ES precession frequency shift relative to the steady state ES precession versus the pulse separation between first and second $\pi/2$ pulse τ_{13} divided in three sections of fine τ_{13} resolution. The NS precession is fitted with a single sine function. The frequency corresponds to the respective gyromagnetic ratio $\gamma/2\pi$. (b) Echo amplitude as amplitude of the oscillations in (a) plotted against the pulse separation τ_{13} in coarse resolution. An exponential fit yields the NS coherence time $T_{2,\text{n}}$.

Figure 4.9: ^{125}Te coherence time $T_{2,\text{n}}$ with (red) and without illumination (black) of the sample during the RF echo sequence. The echo amplitude is plotted against the time between the first and the third pulse τ_{13}. The decay is fitted with a single exponential function in both cases, which shows that $T_{2,\text{n}}$ is elongated under illumination.
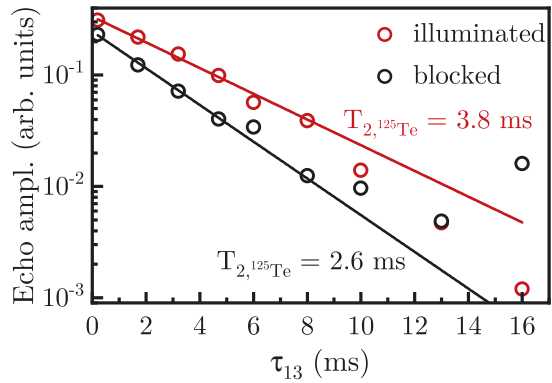
4.8 Conclusions

The present setup allows for a low perturbation characterization of the NSP dynamics. Three different timescales are found for the three fundamentally different processes: The longitudinal NS relaxation (depolarization along the external field B_x) takes place on the minutes timescale, the transversal NS relaxation (decoherence) occurs within milliseconds and the (transversal) dephasing within the NSP happens in the hundreds of microseconds. This applies to the dynamics of all nonzero spin isotopes (^{111}Cd, ^{113}Cd, and ^{125}Te). The NSP dynamics for all isotopes is uniform in the absence of pulsed excitation during the NS evolution. It is a hint to an efficient spin transfer between the isotopes. This is supported by the timescale of $T_{2,\text{n}}$ which is typical for the dipole-dipole interaction in such semiconductor structures [Kal17,

p. 425]. It is only efficient if the difference in Zeeman splitting between neighboring nuclei does not exceed the effective dipole field of the nearest neighbor [Kal17, p. 393]. While a common blocking of the spin diffusion via nuclear dipole-dipole interaction between one isotope species in low-dimensional structures is given by the localized electron (Knight field) [Hei15], this does not apply to the weakly localized electrons in the studied CdTe QW structures [Zhu07]. The NS diffusion is also not hindered by additional quadrupole splittings as all nonzero NS isotopes have spin $1/2$.

Between different isotope species, however, the significantly different Zeeman splittings hinder an efficient NS diffusion via nuclear dipole-dipole interaction. Instead, the ES could lead to a NS diffusion by flip-flop processes, effectively linking two different NSs. This is an efficient source of NS depolarization in QDs [MBI07] and can be mediated by weakly localized electrons [Rei10]. These flip-flop processes are considered here as the main NS diffusion mechanism.

It is also shown in this work, that the significantly spin polarized electron gas under constant, circularly polarized pulsed excitation [Zhu07] slows down and diversifies the NS dynamics for the different isotope species. The pulsed excitation seems to suppress the NSP relaxation and inter isotope diffusion. When compared to similar studies, it is especially puzzling that the longitudinal NS relaxation $T_{1,\mathrm{n}}$ is elongated under illumination: For the localized electron ZnSe:F (fluorine-doped zinc selenide), $T_{1,\mathrm{n}}$ drops by three orders of magnitude under equivalent illumination compared to the evolution in darkness [Hei16].

As an outlook, the characterization of the NS dynamics as presented in this chapter could be applied to a larger variety of low-dimensional systems with considerable hyperfine interaction, complementary to the measurement of the Zeeman shift in the sample PL [Che15]. For the studied CdTe QW system, further experiments for different experimental parameters (excitation power density D_{Pu}, external field dependence B_x, and experiments in a tilted external field for increased NSP [San06]) should be carried out to elucidate the striking differences between the evolution of the NSP in darkness and under pulsed excitation.

5 Free Electron Spin Dynamics in the Electron-Nuclear Spin System of an Ensemble of InGaAs Quantum Dots

The development and demonstration of the EPP setup on a well-studied physical system [Bel16] allows one to utilize it confidently on an ensemble of singly-charged (In,Ga)As/GaAs QDs. For reference, the data presented in this chapter is measured on sample #14056a-880, unless stated otherwise.

In this chapter, the rephasing of the inhomogeneous ESP to bursts is briefly introduced in Sec. 5.1. In the remainder, the free dynamics of the ESP in a transverse field is studied. It is of particular interest since it allows to resolve the individual ES spin modes, which contribute to the spin ML. By using spectrally wide RF fields, it is possible to suppress the influence of the NSP on the ESP in Sec. 5.2.1 and allows one to study the ES system separately in Sec. 5.2.2. The penultimate Sec. 5.3 presents a measurement, where the free dynamics and mode spectrum is used to find an explanation. The chapter finishes off with conclusions drawn from the presented results in Sec. 5.4. The results shown here have been partly published in Ref. [Eve18].

5.1 Electron Spin Polarization Bursts

In an ensemble of QDs pumped by an infinite train of laser pulses, the ESP can rephase before the next pulse. This is referred to as ES ML [Gre06b] or ESP revival [Jäs17]. The ML originates from the phase-locking of the majority ESP by each pulse. The ESP also rephases without any pump pulse at multiples of the pump pulse separation [Gre07] (see also Sec. 2.5.1). This has, however, only been shown for pump pulse sequences separated by far less than the ES coherence time. Figure 5.1 illustrates the formation of these bursts at an external magnetic field of $B_x = 2\,\mathrm{T}$ with Fig. 5.1(a) depicting the PP spectrum with pump pulses orienting the ESP every 13.2 ns. An ESP revival forms before the next pump pulse (ML). No bursts are visible. In Fig. 5.1(b), an additional pump pulse orients the ESs also after a quarter of the repetition period. This allows one to modify the PSC such, that only ESP precession modes with a fourfold frequency separation are excited. It leads to the appearance of two ESP bursts, that are a signature for the modified
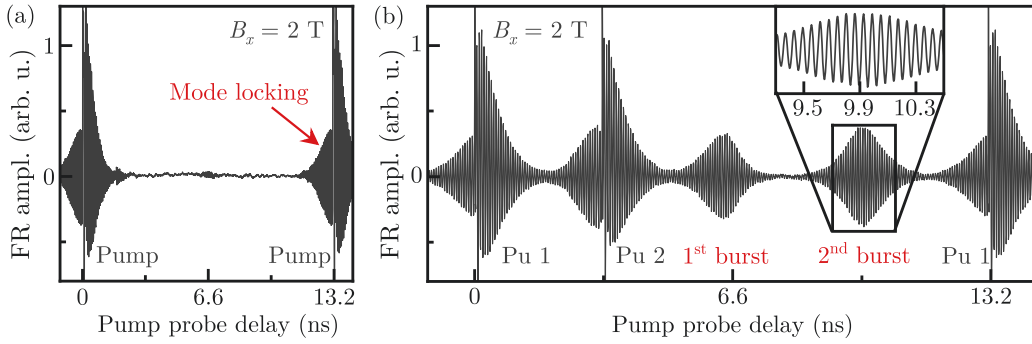
Figure 5.1: Dephasing and rephasing of the ESP in an ensemble of QDs leads to the formation of ES bursts. (a) The ESP is oriented by the pump pulses every 13.2 ns and dephases within 1 ns due to the spread of the precession frequencies. Before the next pump pulse, the ESP rephases as result of the equal phase at pump excitation of each ES (mode locking (ML) [Gre06c]). (b) A second pump pulse introduced at $1/4\,T_R$ between the two pumps fixes the precession phase of each amplified ES at $1/4\,T_R$. The ESP rephases also at $1/2\,T_R$ and $3/4\,T_R$, and ESP bursts appear.
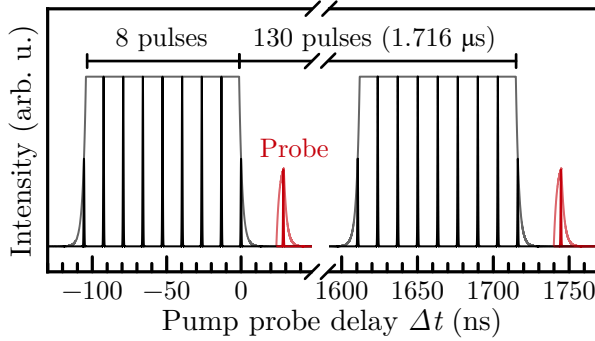

Figure 5.2: Exemplary laser pulse sequence for an EPP measurement. The dynamics can be probed within the 1600 ns dark time between the pulse trains of 8 pump pulses (black) by the probe pulse (red). The solid lines give the electric signal to the modulators. The pulse sequence is repeated in a period of 1716 ns or 130 pulses. The 8 pump pulses are defined as 8 full pulses: the first and the last pulse of the 9 pulses are set to half intensity.

mode structure. The inset shows the resulting beating and central frequency. Note that there is still a large number of modes present.

The EPP technique allows one to study the free dynamics of the ES without excitation within the ES coherence time $T_{2,e}$. Figure 5.2 depicts exemplary pulse sequences used. The period of the pulse sequence amounts to 1.716 µs and is therefore larger than the typical $T_{2,e} = 0.8\,\mu s$ [Her08]. As all pulses are sliced out of a continuous sequence of pulses with a period of $T_R = 13.2\,ns$, the EPP period has to equal a multiple of T_R. The period of the exemplary sequence in units of T_R would be 130 pulses and the period of number of pulses can be used as a timescale as well. Out of these 130 pulses, eight pulses are taken as pump pulses. The pump

pulses are close to π pulses for optimal ES orientation[1]. The probe pulse is cut out of the 130 probe pulses. The probe pulse can probe after the pump pulses (as depicted in this example) as well as in between pump pulses. Note that pump and probe pulses stem from the same laser and are therefore synchronized to each other.

Figure 5.3: First ESP burst after different number of pump pulses separated by a repetition period of 13.2 ns. The delay of the first rephasing point is marked with a gray line. The amplitude increases with the number of pulses, while the width decreases. More precession modes lead to the decreased burst width while the amplitude increase is a hint to a larger total ESP.
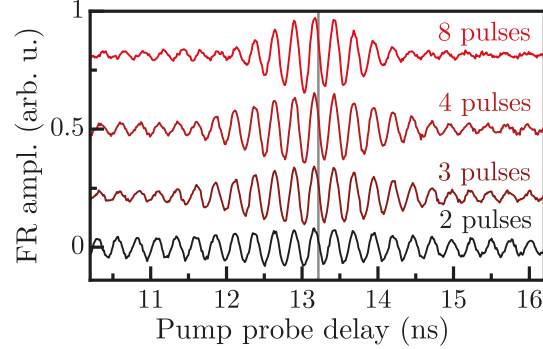
This exemplary pulse sequence is used to study the first burst at the position of the first missing pulse in dependence of the number of exciting pump pulses, as shown in Fig. 5.3. The burst amplitude as the FR amplitude at 13.2 ns determines the degree of the ESP. The amplitude rises and reaches saturation, when orienting the ESs with four pump pulses. The width of the burst gives a hint to the number of modes contributing to the signal. While for two pulses, only a small number of modes is present, for three and four pulses an increasing number of modes is activated. Note that for eight pulses, the amplitude does not increase but the width decreases. The ESP is redistributed to more modes, as evidenced in more details in the following sections. As the distance between the pump pulse trains is larger than the electron coherence time, the ESP solely stems from the excitation with the indicated number of pump pulses. The NSP created by DNP, however, persists up to seconds [Gre07] and allows to forward the information on the past ES orientations to the next pulse sequence.

5.2 Influence of the Nuclear Spin Polarization

The influence of the NSP is studied in this chapter by suppressing the NSP, using long broadband RF pulses which randomize the NS state population of all constituent nuclei (see Sec. 3.4 for details). The comparison to the non-suppressed TRFR spectrum allows to identify their contribution.

A striking demonstration is given for the case of the exemplary EPP pulse sequence shown in the previous section with two orienting pump pulses. The free dynamics

---

[1]A π pulse refers to a pulse with a pulse area $\Theta = \pi$ [Yug09].
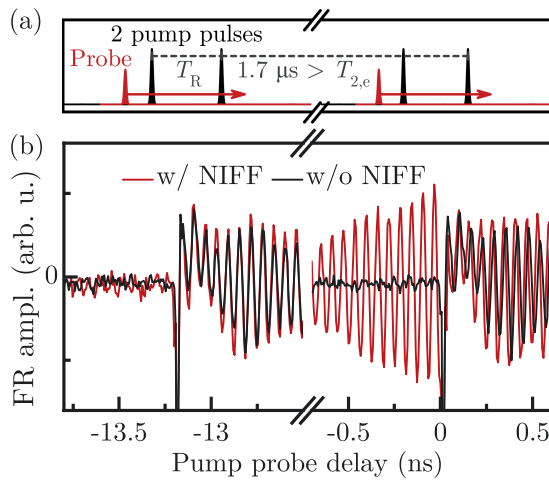
(a)

(b)

Figure 5.4: Influence of the NIFF on the ESP precession. (a) Pulse arrival diagram. Two pump pulses (black) are used with a repetition period of $1.7\,\mu s > T_{2,e}$. The probe pulse (red) is scanned over both pump pulses. (b) PP spectrum with NIFF (red) and with suppressed nuclear polarization (without NIFF, black). No ML without NIFF is present before the second pulse as the ES does not remember the pulse sequence, but it can be imprinted on the NSP with much larger depolarization time by NIFF.

and further details are given in the following sections. Figure 5.4(a) shows the used pulse sequence. Here, the EPP spectrum is taken over the distance of both pump pulses and shown in Fig. 5.4(b). The black curve shows the FR without NS contribution (RF suppression of the NIFF). The first pump pulse orients the ESP, and it precesses with an average frequency until the ensemble precession ceases due to the destructive interference caused by the different individual ESP precession frequencies. Upon the second pump pulse, the signal is already dephased and no ML is observed. The second pump pulse orients the ESP like the first one. With nuclear contribution (no NSP suppression), the first pump pulse orients the ESs to the same degree as in the previous case (green curve). The ESP precesses with an average frequency and dephases. Before the second pulse, however, the ESP rephases and ML appears.

The second pump pulse preferably orients ESs with a precession frequencies commensurate to the PRF. ESs with a non-commensurate precession frequency can be subject to an additional optical Stark field which tunes the ES Zeeman splitting to the NSs Zeeman splitting and enables a spin transfer to the NS bath (NIFF [Yug09]). The information on the two pulse excitation is stored in the NSP for times longer than the pulse sequence separation [MER02] and allows the preferential orientation of the ESs embedded in the NS bath, by the first pump pulse in the latter case. This mechanism is suppressed in the former case and the information on the two pulse excitation is lost, as the ESs are not coherent to the ESs oriented by the previous pulse sequence.

5.2.1 Influence on the Free Dynamics of the Electron Spin Polarization

To observe the free dynamics of the ESP, the EPP setup with the previously described pulse sequence is used. The free dynamics of the ESP at an external field
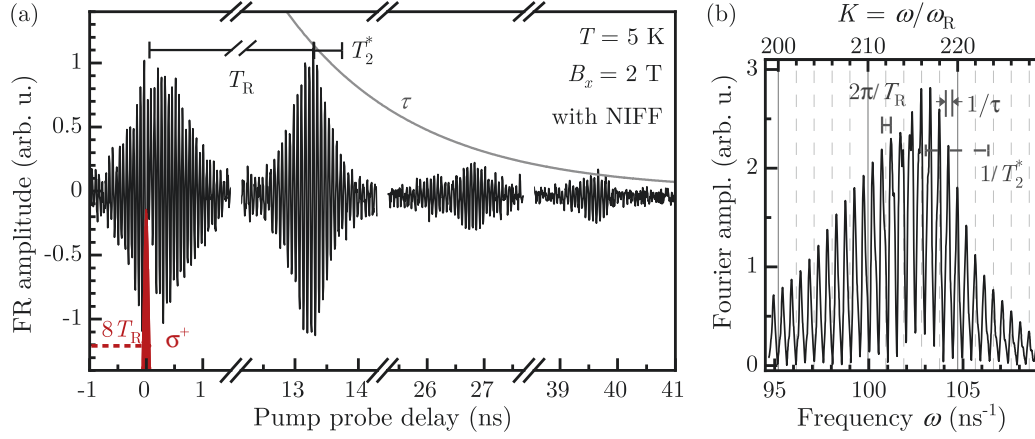
Figure 5.5: Free dynamics of the ESP. (a) PP spectrum after a pump pulse train of 8 pulses with the last at a delay of 0 ns. The dephasing and rephasing within $T_{2,e}^*$ to the first burst within T_R as well as to to additional bursts with a burst amplitude decay τ is shown. The nuclear polarization is not suppressed. Hence, the ESP is shown with NIFF. (b) Fourier transform of the measured free dynamics. A spectrum of well defined modes is present. The timescales τ, T_R, and $T_{2,e}^*$ are reflected by the width of each mode, the mode separation, and the width of the envelope, respectively.

of $B_x = 2\,\text{T}$ with NIFF is shown on Fig. 5.5(a). After the last pump pulse, the ESP dephases within $T_{2,e}^* = 1\,\text{ns}$. The first ESP burst forms after $T_R = 13.2\,\text{ns}$ and up to 3 bursts are visible at multiples of T_R. The burst amplitude decays on a timescale τ. To analyze the free dynamics, a numeric Fourier transform is carried out as shown on Fig. 5.5(b). The Fourier amplitude is shown versus the frequency (bottom scale) and the mode number K (top scale). The timescales present in the dynamics are reflected in the Fourier spectrum. It consists of a Gaussian envelope with width $1/T_{2,e}^*$ in which the constituent modes with a separation of $2\pi/T_R$ are resolved. The mode width is defined by the burst decay $1/\tau$.

The number of modes in the FWHM of the envelope, calculated with a g-factor spread of $\Delta g_e = 0.028$ according to (2.13), amounts to $M = 10$ at the field of $B_x = 2\,\text{T}$ around the central mode 214[2]. However, the width of the envelope clearly exceeds this value and can be explained by DNP as explained in the next section. Note also, that the modes are running on integer numbers K for frequencies higher than the central frequencies, while they are running in between integers for lower frequencies. It is as well caused by NIFF [Kop19] and will be studied in more detail in the next section.

The experiment was repeated without nuclear contribution by broad spectral RF application (see Fig. 5.6). The TRFR after 60 pump pulses is shown, while the

---

[2]The g-factor spread is calculated from the magnetic field dependent PP spectra used for Fig. 5.9.
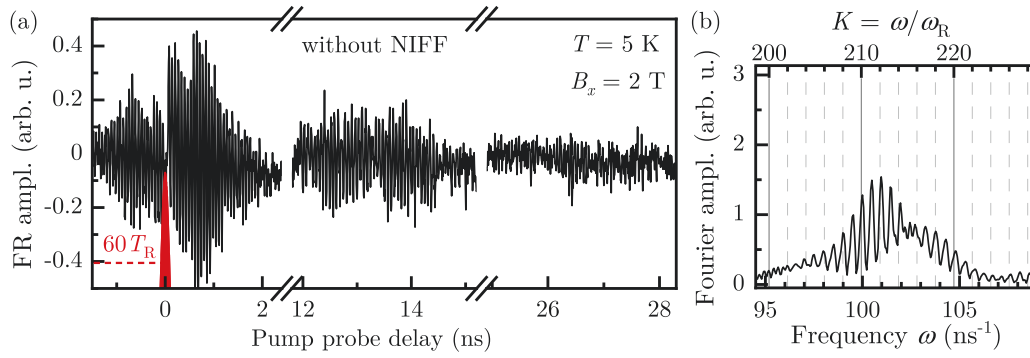
Figure 5.6: Free dynamics of the ESP with suppressed NSP (without NIFF). (a) The PP spectrum is shown after 60 pump pulses and a pulse sequence separation of 1.7 µs. (b) Fourier transformation of the PP spectrum. The mode spectrum exhibits the timescales present in the PP spectrum and two flanks around the central mode ($K = 214$) as a result of the spectral dependence of the Faraday rotation (see Sec. 6.3.2). The comparison of the spectra with and without NIFF is shown in Fig. 5.7.

remaining parameters of the pulse sequence are chosen as in Fig. 5.2. Even after 60 pump pulses, the total ESP is halved when compared to the case with NIFF. Moreover, the second burst is hardly visible and the burst width is larger than with NIFF. It is reflected in the Fourier transform. The number of modes is reduced to the expected number and the mode width is increased as the amplitude does not drop close to zero in between modes. Additionally, two sides of the spectrum can be clearly seen around the central mode 214. Towards lower frequencies, the mode amplitude is increased with more pronounced modes. It is an effect of the dependance of the Faraday rotation detection on the optical detuning between probe and trion resonance [Eve18] and is also present with NIFF. It is however hidden due to the NSP, which lets ESs precess on frequencies not matching their precession frequency mainly defined by the g factor and, hence, detuning. A separate analysis of the real and imaginary part of the precession spectrum reveals these peculiarities in the next section.

5.2.2 Electron Spin Mode Spectra

The amplitude of the Fourier transform of the free dynamics is not sensitive to the sign of the precessing ESP. Further analysis of the mode spectra is therefore done on the real and imaginary part separately. Fig. 5.7 displays the mode spectra for the real and the imaginary part for the case with and without NIFF. Additionally, two different numbers of pump pulses are investigated to assess the build-up of the ES precession spectrum.

The imaginary part is taken as an example for a detailed discussion, but the main
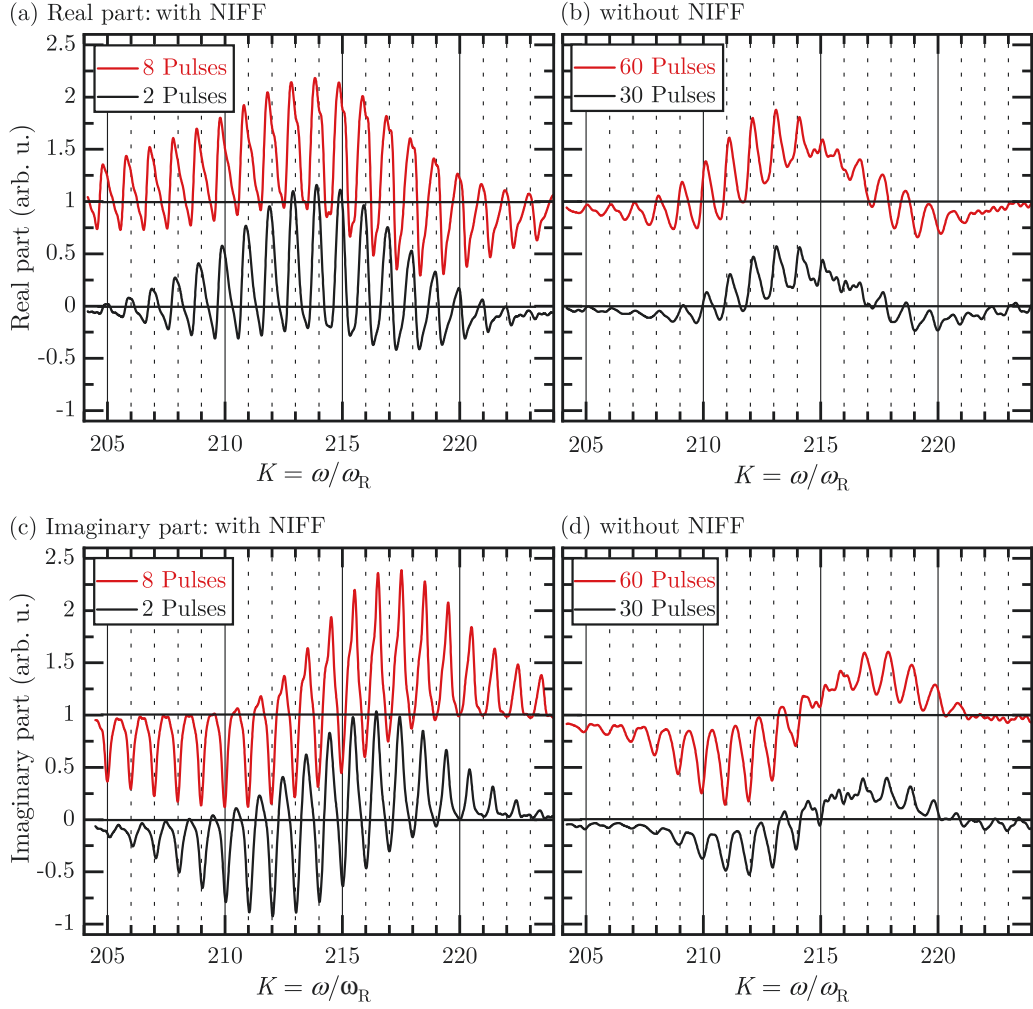
Figure 5.7: Imaginary and real part of the complex Fourier transformation with and without NIFF. (a),(b) Real part of the Fourier transform with and without NIFF. (c),(d) Imaginary part of the Fourier transform with and without NIFF. The dispersion-like spectral dependency of the Faraday rotation leads to the dispersion-like mode amplitude. $B_x = 2\,\text{T}$.

features are also present in the real part. As before, the central mode is mode $K = 214$. In the case with NIFF (see Fig. 5.7(c)) as well as in the case without NIFF (see Fig. 5.7(d)) the FR, with a dispersion-like spectral dependence on the optical trion resonance, leads to a negative contribution for lower frequencies (positive optical detuning) while it leads to a positive polarization for higher frequencies (negative optical detuning) [Kop19].

Without NIFF, the regimes are clearly separated. The modes on the low frequency side (negative peaks) as well as on the positive side (positive peaks) fall on integer mode numbers. The polarization of modes far-off the central mode does not increase strongly when polarizing with 60 pump pulses instead of 30 pump pulses and the number of modes is restricted to the number of modes calculated by the *g*-factor spread.

The picture gets more involved with NIFF. The FR signature is still clearly visible. With NIFF, however, the regime of positive and negative detuning overlap around the central mode. As the optical trion resonance does not change, the NSP is considered responsible for the shift of the precession frequency by adding an effective field, the OF. It is supported by model calculations [Eve18], that the OF, established by the optical Stark effect [Kor11], can overlap several modes. In Sec. 6.2.1, it is shown that the OF can be build-up far larger. Additionally, the comparison between the free dynamics after two pump pulses and eight pump pulses shows that far-off modes, which should not be polarized significantly, are populated with an increasing number of pump pulses. Note also that higher frequency peaks now precess in between integer modes, while the lower frequency modes precess on integer modes. It is as well expected in a hyperfine interaction mediated spin transfer from the ESP to the NSP, as shown in [Car09], in a quantum mechanical central spin model [BUA17] as well as in a fluorine-doped ZnSe epilayer [Zhu18a]. The mode spectra thereby give a convincing evidence that the NIFF is, dominantely, mediated by collinear hyperfine interaction.

5.2.3 Build-up of the Electron Spin Polarization

The EPP scheme allows to observe the steady-state ESP for different number of pump pulses and to observe the build-up of the ESP. The differences between the build-up with and without NIFF are analyzed. In order to determine the steady state ESP, the ML amplitude is evaluated before the last pump pulse against the number of total pump pulses in the pulse sequence, described in Sec. 5.1. The ML amplitude is determined by fitting an inhomogeneously decaying cosine function (2.11) to the PP spectrum as shown in Fig. 5.8.

To describe the ESP build-up, the ML amplitude is fitted by an exponential saturation law

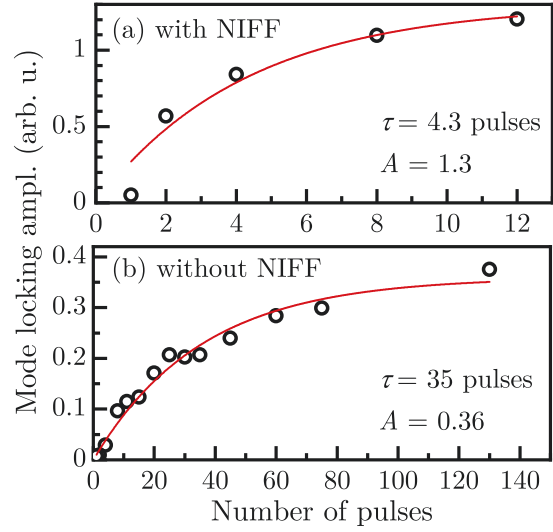$$y = A \left(1 - \mathrm{e}^{-\frac{N}{N_{\mathrm{sat}}}} \right)$$

Figure 5.8: Build-up of the ESP with increasing number of pump pulses. (a) The ML amplitude before the last pulse is plotted against the number of preceding pump pulses in a pump pulse sequence. The saturation is reached at twelve preceding pulses. (b) Without NIFF, the ML amplitude saturates only at a fourth of the level with NIFF after 130 pulses.

with the saturation amplitude A and the number of pulses until the ML sets in, N_{sat}. Without NIFF, the ML amplitude only saturates with the continuous application of pump pulses (130 pump pulses) at an amplitude of $A = 0.36$. This amplitude is arbitrary and only relevant relative to the data present here. The characteristic number of pulses is $N_{\mathrm{sat}} = 35$ pulses. With NIFF, the amplitude reaches $A = 1.3$ and the characteristic number of pulses amounts to $N_{\mathrm{sat}} = 4.3$ pulses[3]. These results show that NIFF increases the ESP achievable in the ensemble fourfold, as additional ESs not fulfilling the PSC are also polarized [Gre07]. The number of pulses necessary to reach a maximal ESP with NIFF fits to the estimations in Ref. [Sha03]. Although NIFF was not considered therein, the work focused on a single quantum dot with an electron Larmor frequency commensurate to the PRF ω_{R}, which thus fulfills the PSC by definition, without modification by NIFF. The build-up of the steady-state ESP presented here support, that the QD ensemble with NIFF can be modeled as initiated by Shabaev et al. [Sha03]. The results presented here also show that an application of pump pulses for $10\,\%$ of the total measurement time suffices to drive a large fraction of QDs on commensurate modes by NIFF.

5.3 Mode Locking Amplitude Dependence

The analysis of the ES precession frequency spectrum allows one to investigate the role of the NSP on the magnetic field dependence in Voigt geometry of the ML amplitude. It was demonstrated, that the ML amplitude shows a non-monotonic behavior with a dip of the ES polarization around $B_x = 4\,\mathrm{T}$ [Var14a]. A detailed investigation of the ML amplitude dependence is studied in FE for three different

---

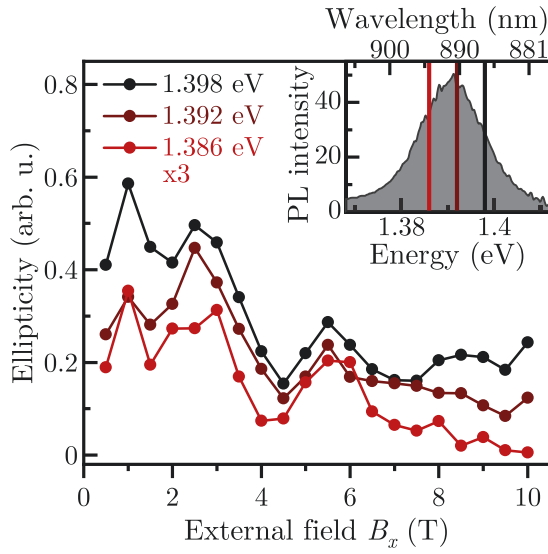[3]Note that π-pulses are used for optimized ES orientation.

Figure 5.9: Dependence of the ML amplitude on the external magnetic field B_x. The ML amplitude (measured in FE) is given for three different excitation energies. The inset shows the positions of the excitation energies in the PL of the QD ensemble in sample #11955-945. On top of the monotonous decrease of the ML amplitude with increasing field, for all excitation energies a minimum around 4 T to 4.5 T appears.

trion resonance within the QD ensemble, as shown in the inset in Fig. 5.9. The sample under study is #11955-945. One optical energy corresponds to the low-energy flank, one to the high-energy flank and one to the center of the PL. The ML amplitude is determined as in the previous section by fitting (2.11) to the PP spectra. The external magnetic field dependence of the ML amplitude shows similar features for all three optical energies, as shown in Fig. 5.9. The ML decreases until 4.5 T with a (local) maximum around 2.5 T. Above 4.5 T, the ML amplitude increases to a local maximum around 6 T and decreases with increasing field. This behavior can be traced back to the Larmor precession of NSs by a fully quantum mechanical as well as a classical central spin model [Kle18]. The number of quarter revolutions of the NSs within the PRP leads to the appearance of pronounced ESP modes running on integer or half-integer multiples of the PRP. The ESP predominantly run on integer modes for odd numbers of quarter revolutions while it is running on half-integer modes for an even number of quarter revolutions. This manifestation of the NSP on the ESP can be investigated using the EPP scheme.

To investigate the mode spectrum, the free dynamics at two different optical frequencies is measured for the field with a local maximum ($B_x = 2$ T, see Fig. 5.10(a)) and with the minimum (4.5 T, see Fig. 5.10(b)). The free dynamics is taken using the pulse sequence introduced before (see Fig. 5.2) and shown in Fig. 5.10(a) for the field with a local maximum ($B_x = 2$ T) as well as in Fig. 5.10(b) for the minimum (4.5 T) at an optical energy of 1.392 eV. The ML amplitude is smaller relative to the signal on the positive side. The bursts are hardly visible for $B_x = 4.5$ T. The Fourier transform of the shown free dynamics as well as for the free dynamics at an optical energy of 1.398 eV are shown in Fig. 5.10(c). Note that the central position of the electronic g factor is shifted according to the negative slope of the spectral g-factor dependence in the sample [Gre06b]. For both optical energies, the envelope
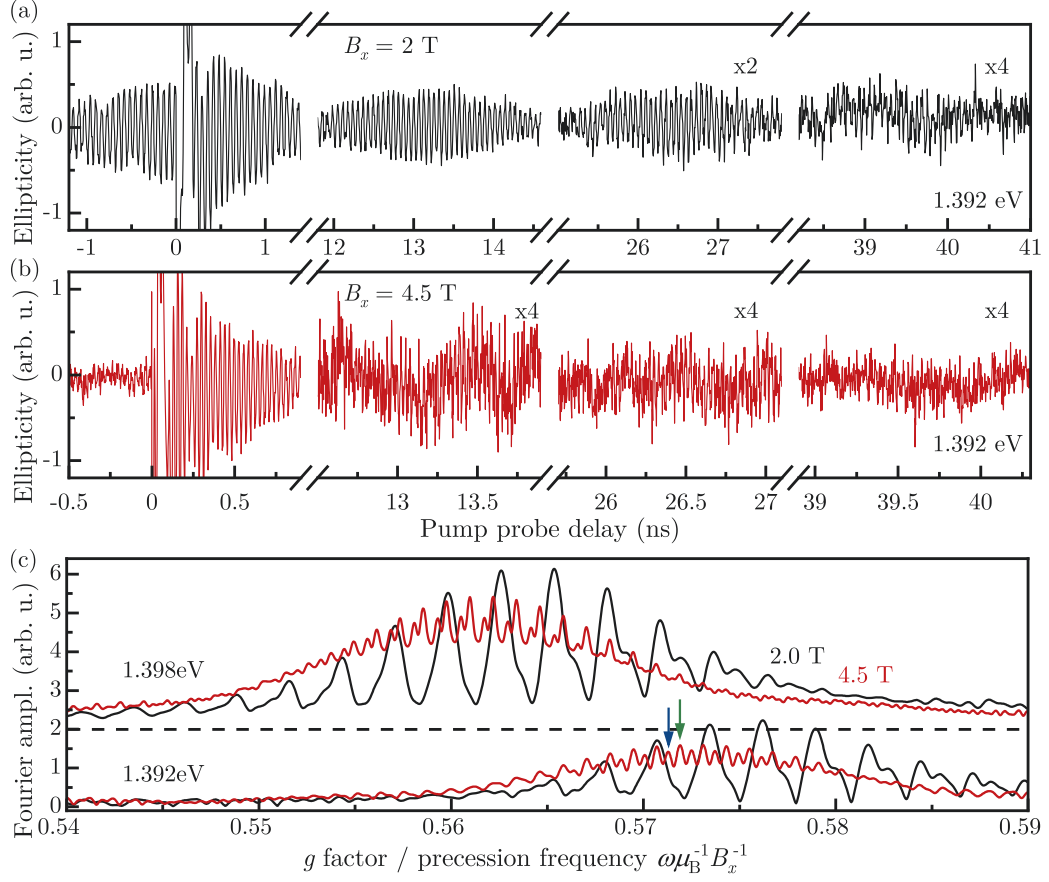
Figure 5.10: Free dynamics and mode spectra for different excitation energies
and external magnetic fields. (a) Free dynamics for $1.392\,\mathrm{eV}$ at $B_x = 2\,\mathrm{T}$. ML
amplitude and the amplitude directly after the pump pulse are similar. The first
and the second burst are of similar amplitude. (b) Free dynamics for $1.392\,\mathrm{eV}$
at $B_x = 4.5\,\mathrm{T}$. (c) Fourier transform of the free dynamics for $2\,\mathrm{T}$ (black) and
$4.5\,\mathrm{T}$ (red). The top curves are measured at an excitation energy of $1.398\,\mathrm{eV}$ while
the bottom curves are measured at $1.392\,\mathrm{eV}$. The shift of the mode spectrum
center reflects the different central electron g-factors. For $4.5\,\mathrm{T}$ not only the mode
separation of the integer modes (green arrow) is reduced 2.25 times, but also modes
on half integer locations of similar amplitude appear (blue arrow).

of the ESP follows a Gaussian curve for both external fields. The amplitude for $B_x = 2\,\mathrm{T}$ is larger than for $4.5\,\mathrm{T}$. In the case of $B_x = 2\,\mathrm{T}$, the ESP is predominantly running on integer frequencies. For $4.5\,\mathrm{T}$, the larger number of present modes stems from the higher external field, as the mode separation is decreased. Additionally, the half-integer modes are more pronounced or even dominant. The green arrow indicates an integer mode and the blue arrow indicates an half-integer mode. The mode spectrum experimentally reveals the manifestation of the NSS on the ESP as cause for the non-monotonic ML amplitude dependence on the magnetic field. The results presented in this section have been partly published in Ref. [Kle18].

5.4 Conclusions

The increased measurement time beyond a single PRP in conjunction with the selective pump pulse blocking reveals bursts of the ESP at multiples of the PRP. Surprisingly, only up to four bursts could be registered although the bursts are expected to emerge up to the ES coherence time $T_{2,\mathrm{e}}$[4]. This could be caused by an additional, low frequency beating of the signal corresponding to the repetition frequency of the pump pulse train with eight consecutive pulses out of 130. The picture remains, when suppressing the NS polarization by resonant RF fields, although in this case, 30 out of 130 pulses are required to achieve a significant ESP.

The extended measurement time allows one to perform a high resolution Fourier transform of the ESP with and without NIFF. While the ES precession mode structure without NIFF follows the FR signature around the central mode [Gla10], the NSP modifies the lower and higher frequency modes differently. As predicted [Car09], NIFF leads to the focusing of lower modes on integer modes K, while the higher modes are focused on the half-integer modes $K + 1/2$[5]. Moreover, NIFF leads to the inclusion of additional modes by the formation of an OF which spans eight modes or $75\,\mathrm{mT}$.

The high resolution Fourier transform also shines light on the reported external field B_x dependence of the ES ML amplitude [Kle18]. At around $B_x = 4.5\,\mathrm{T}$, the ML amplitude drops only to rise again for larger external fields. In the models, this is attributed to the resonance of the PRF with a quarter of the NS Larmor frequency, which leads to the simultaneous existence of integer and half-integer modes canceling out the ESP rephasing. These modes are resolved in the Fourier transform.

---

[4]In other words, the width of each mode is significantly larger than $1/T_{2,\mathrm{e}}$.

[5]This is not the first experimental trace of the focusing on half-integer modes, however, as it was experimentally investigated in the same Ref. [Car09].

6 Efficient Nuclear Spin Polarization in InGaAs Quantum Dots Under 1 GHz Pulsed Optical Excitation

To establish an efficient NS polarization in n-doped InGaAs QDs optically, it has been suggested to use a high PRF pulsed excitation with circularly polarized pulses [Car09]. The suggestion is based on the finding, that the direct action of the laser pulse has been identified to trigger the transfer of the ES to the NSS via collinear hyperfine interaction in Voigt geometry, as the optical pulse creates a Stark field along the optical axis [Ber08]. The ES acquires a component parallel to the external field, which enables the NS polarization by collinear hyperfine interaction[1]. However, this transfer is hindered, when the circularly polarized laser pulse arrives at a QD, where the resident electron is still bound in the negative trion, originating from the previous pulse. The ES polarization is therefore inefficient for a PRP T_R close to the trion lifetime τ_Tr ($\tau_\mathrm{Tr} = 400$ ps in the studied sample [Gre06b]) and, hence, the PRP should be not much lower than $3\tau_\mathrm{Tr} = 1.2$ ns. The excitation with 1 GHz PRF (1 ns PRP) thus promises an efficient NS polarization, close to the lower limit of the PRF.

The chapter starts off with the introduction of a collective ES precession of resident electrons in an inhomogeneous ensemble of quantum dots under 1 GHz pulsed excitation in Sec. 6.1, which is studied in detail in Sec. 6.1.1. The importance of the NSP in the QDs for the ES precession on a single mode is elucidated in Sec. 6.1.2. The two laser setup, which allows for the measurement of the ESP dephasing time $T_{2,\mathrm{e}}^*$ larger than 1 ns, is described in Sec. 6.1.3 and the elongated dynamics accessible indicates a reduction of the NSF, as detailed in Sec. 6.1.4. The seconds-long NS depolarization time is used to demonstrate the single mode ES precession in QDs, even without the driving 1 GHz laser, in Sec. 6.1.5.

Sweeping the external magnetic field B_x under 1 GHz pulsed excitation leads to the build-up of a NSP, which counteracts the external field variation, as introduced in Sec. 6.2 and detailed in Sec. 6.2.1. The depolarization dynamics of the established NSP is investigated in Sec. 6.2.2. The knowledge of the involved timescales allows one to implement an optimized NS polarization protocol presented in Sec. 6.2.3. To bring down a round figure, additional parameters of the setup are investigated, such as the sweeping down of the external field under illumination (Sec. 6.3.1),

---

[1]Additionally, a larger PRF leads to a larger ESP [Yug09] which in turn also enhances the spin transfer.

the influence of the pump probe detuning on the NSP build-up (Sec. 6.3.2), the influence of the external field sweeping rate and the field angle (Sec. 6.3.3), and the behavior of the ENSS for external field sweeping larger than the maximal discernible NSP (Sec. 6.3.4). The chapter finishes with a conclusion of the main findings in Sec. 6.4.

6.1 Single Mode Electron Spin Precession in an Inhomogeneous Quantum Dot Ensemble

The investigation of an ensemble of QDs offers several benefits when compared to the measurement on single QDs, like the mentioned large total light matter coupling and the simultaneous measurement of 10^{10} QDs, which highlights general features. The results presented in this section have been published in Ref. [Eve21b].

However, the ensemble is inhomogeneous in trion energy and in QD size (the number of atoms in a QD). The inhomogeneity in trion energies[2] causes an inhomogeneity in g factor Δg_e and Zeeman splitting, described by the Roth-Lax-Zwerdling relation [RLZ59]. Additionally, each individual QD has a randomly oriented NSP δB_N, as any given time. Although this NSP fluctuates in time in individual QDs, each QD exhibits its own fluctuating NSP in an ensemble measurement, whose average value depends on the QD size (see also Sec. 2.5). The NSF can therefore be treated as an ensemble effect [SRU14] and also leads to an inhomogeneity of the effective Zeeman splittings in the ensemble via hyperfine interaction. For pulsed excitation with circularly polarized laser pulses in n-doped InGaAs/GaAs QDs, only precession modes, that fulfill the PSC (2.14), develop in the ENSS. Only modes covered by the broadened Zeeman splittings can be amplified and the separation of modes is given by the PRF (see Sec. 2.5.1 for details). The number of modes excited simultaneously is therefore directly dependent on the PRF.

6.1.1 Single Mode Precession Under 1 GHz Excitation

In the extensively studied pulsed excitation with a PRF of 75.76 MHz, the separation of precession modes amounts to $\omega_\mathrm{R} = 0.476\,\mathrm{ns}^{-1}$ or $B_0 = 9.72\,\mathrm{mT}$, which leads to the simultaneous excitation of several modes in any external Voigt field for the studied QD ensemble [Gre09][3]. However, for the 1 GHz PRF studied in this work,

---

[2]The laser spectrum is Gaussian shaped and, therefore, the g-factor spread follows a Gaussian distribution. The NSF are also Gaussian distributed [MER02].

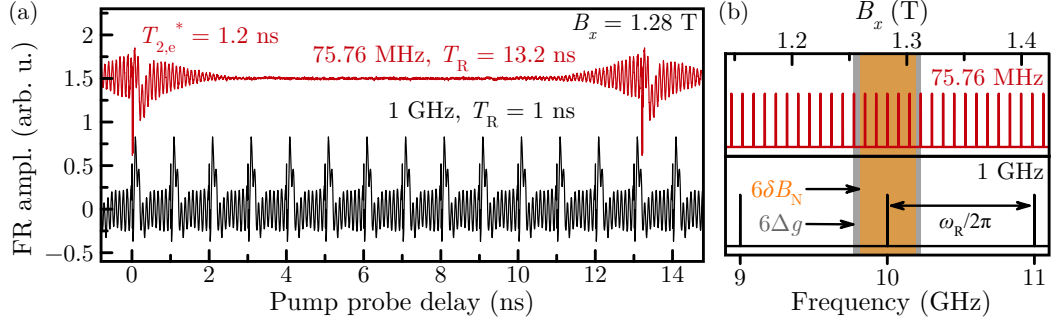[3]Even in the doubled PRF of 151.52 MHz in Ref. [Gre09], several modes exist simultaneously.

Figure 6.1: ESP in an inhomogeneous ensemble of QDs under excitation with an PRF of 75.76 MHz (red) and 1 GHz (black). (a) PP traces at an external field of $B_x = 1.28$ T. The 75.76 MHz trace shows an ESP dephasing time of $T_{2,\mathrm{e}}^* = 1.2$ ns, while the 1 GHz trace shows a single precession frequency between two pump pulses. The 75.76 MHz curve is shifted vertically. (b) Scheme of expected ES precession modes due to the g-factor spread Δg_e in the ensemble (gray) and the NSF in the QDs δB_N (orange) at $B_x = 1.28$ T. The expected modes are covered by the correspondingly colored areas. The areas reflect the three-fold standard deviation in each direction, as even barely covered modes are effectively polarized due to NIFF. At 1.28 T, the number of modes is defined by $6\Delta g_\mathrm{e}$. For an PRF of 75.76 MHz, the coverage of seven modes is expected, while for 1 GHz only one mode is polarized, as seen in (a).

the mode separation with an average electron g factor of $g_\mathrm{e} = 0.557$[4] yields

$$\omega_\mathrm{R} = \frac{g_\mathrm{e}\mu_\mathrm{B}B_0}{\hbar} = 6.27\,\mathrm{ns}^{-1} \quad \text{and} \quad B_0 = \frac{\hbar\omega_\mathrm{R}}{g_\mathrm{e}\mu_\mathrm{B}} = 128\,\mathrm{mT} \tag{6.1}$$

with the Planck constant $\hbar$ and the Bohr magneton μ_B. This is 16-fold the reported NSF for this sample of $\delta\omega_\mathrm{N} = 0.37\,\mathrm{ns}^{-1}$, as well as the precession frequency spread at 1 T of $\Delta\omega_{g_\mathrm{e}} = 0.35\,\mathrm{ns}^{-1}$ [Gre09].

The experimental technique used in this chapter is the PP technique with experimental details given in Sec. 3.2. The measured single mode precession at an external field of $B_x = 1.28$ T is shown in Fig. 6.1(a) (black curve). In between the pump pulses coming each 1 ns, the ESP precesses with a single frequency[5]. For a PRF of 75.76 MHz (red trace), however, the ESP coherently dephases within $T_{2,\mathrm{e}}^* = 1.2\,\mathrm{ns}$[6]. Right before the next pump pulse, the ESP rephases within $T_{2,\mathrm{e}}^*$. The dephasing is dominated by the destructive interference of many modes.

---

[4] The average electron g factor is determined by evaluating the precession frequency in different external fields B_x for a pulsed excitation with a PRF of 75.76 MHz, as given in Sec. 6.1.4. The precession frequency shows a linear dependence on B_x with a slope proportional to the electron g factor. The experimentally determined g factor falls in line with the previously found relation in Sec. 3.5.1.

[5] The trion decays within $\tau_\mathrm{Tr} = 400$ ps [Gre06b], which is reflected in the initial exponential decay. This decay is also present in the 75.76 MHz PP trace (red).

[6] The dephasing time results from a fit with the Gaussian decay given in Eq. (6.2).

As found in Sec. 5.2.2, all modes even barely excitable in the QD ensemble are efficiently polarized due to NIFF [Eve18]. The number of simultaneously present modes can be described by the six-fold standard deviation around the main mode, as shown in Fig. 6.1(b). Quantitatively, the PRF needs to exceed 180 MHz to enable single mode precession in the external field-indepedent nuclear fluctuation field. For external fields larger than 1.1 T, the field dependent precession frequency spread caused by the *g*-factor inhomogeneity dominates. While the 75.76 MHz PP trace consists of at least seven modes, the single mode precession following the 1 GHz excitation conforms to the reported *g*-factor spread and broadening due to the NSF. Only for external fields larger than $B_x = 3.1$ T, a second precession mode can develop when the external field is exactly between mode fields, and a third mode should only show up for fields larger than $B_x = 6.0$ T, when using a 1 GHz pulsed laser. As
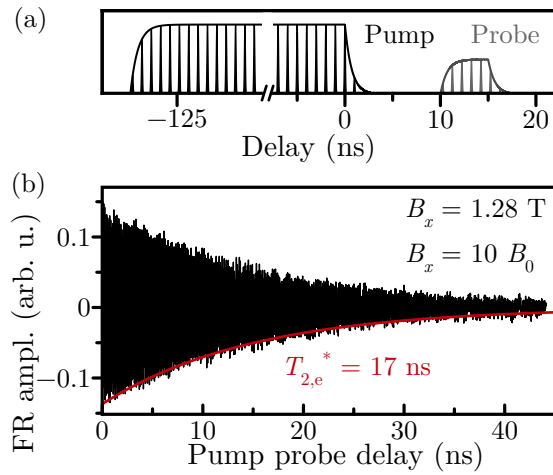

Figure 6.2: Extended pump probe (EPP) measurement of the ESP dephasing at $B_x = 1.28$ T. (a) Timing diagram of the 1 GHz pulses picked. The electronic driving and optical components of the pulse picking does not allow to cut off immediately after one pulse (see envelope). Only six probe pulses can be picked together and lead to an additional exponential decay. (b) EPP trace corrected by the additional exponential decay due to the multi-pulse picking. Zero delay is placed, where no direct interference of the pump and probe pulse is observed any more. The $T_{2,e}^*$ is given by an exponential fit to the EPP trace.

the dephasing time clearly exceeds 1 ns, using the EPP technique [Bel16] enables to measure long dynamics by selectively blocking pulses and, thus, to increase the separation of pump and probe (see Sec. 3.3). As a 1 GHz repetition frequency is used, the electronics of the blocking devices, pulse picker and EOM, are not fast enough to select single pulses. Moreover, the leading and falling edges are too broad, and the pulses diminish in intensity over 5 ns (the edges of the electronics) and are not blocked from one pulse to the next. Additionally, the laser could not be synchronized to the blocking electronics. Fortunately, pump and probe pulses are synchronized to each other, as are the pump blocker and the probe blocker. Hence, an uncertainty of the arrival time of the pulses on the order of the edge times is assumed as it is not known, which probe pulse contributes with which intensity to the signal (broad edges) but pump and probe pulses still have a fixed relation to each other (synchronized pulses).

In the extended ES dynamics, shown in Fig. 6.2, the last pump pulse is estimated by assuming that the last coincidence peak is the last registered coincidence with

significant contribution. The external field is set to $B_x = 1.28\,\text{T} = 10B_0$, hence on a mode field. The ES is amplified and exhibits a dephasing time of $26\,\text{ns}$. It is significantly shorter than the ES coherence time $T_{2,\text{e}} = 800\,\text{ns}$ [Her08]. This indicates, that a distribution of precession frequencies in the vicinity of the mode still exists, but this distribution is smaller than the ESP dephasing time induced by the NSF. Hence, the nuclear fluctuations are suppressed, which will be investigated further in Sec. 6.1.4.

6.1.2 Electron Spin Precession Frequency Steps

To study the ES dynamics in different external fields B_x, a series of 1 GHz PP traces with an optical PP detuning as in setup 3 in Fig. 6.15(a) is taken each $13\,\text{mT}$. The average laser powers right in front of the cryostat amount to $P_{\text{Pu}} = 5\,\text{mW}$ (power density $D_{\text{Pu}} = 260\,\text{W cm}^{-2}$) and $P_{\text{Pr}} = 130\,\mu\text{W}$ ($D_{\text{Pr}} = 8\,\text{W cm}^{-2}$). The external field is driven under 1 GHz illumination. Starting from $300\,\text{mT}$, the external field is driven in between measurements with a speed of $6.1\,\text{mT/s}$.

Each PP trace is fitted with a single, non-decaying cosine. The resulting precession frequency is given in Fig. 6.3(a). For low magnetic fields of up to $0.5\,\text{T}$, a nearly linear increase of the electronic spin precession frequency is observed with an increasing external magnetic field. It is, however, a hint of steps in the precession frequency visible. Similar to the case of ZnSe:F QWs [Zhu18a], plateaus with constant precession frequency and amplified polarization form at mode fields[7]. The additional field necessary to fix the ES precession frequency on the plateaus can be attributed to the NSP as OF and can, thus, be described in the frame of DNP: The optically detuned pump pulse induces an optical Stark field, which leads to an ES component along the external field B_x [Car09]. The direction (parallel or anti-parallel to B_x) of this ES component depends on the difference of the precession frequency to the nearest mode frequency [Kop19]. Consequently, the hyperfine interaction leads to ES-NS flips, which tune the OF to match a mode field together with the external field [Car09][8]. Alternatively, the ES precession on a mode can be described as the most stable ENSS configuration, which is therefore favorably realized [Kor11]. It is known that the quadrupolar interaction in strained QDs also play a significant role in the transfer of the ESP to the NSP [Urb13]. However, the description used here is based on the model used in [Eve21b; Eve21a], which suffices to describe the observed phenomena[9].

---

[7] The term mode field denotes external magnetic fields at which the PSC for the electronic spin precession is fulfilled. This corresponds to integer multiples of B_0.

[8] The direction of the OF depends on the sign of the electronic g factor, the sign of the optical detuning, and the sign of the hyperfine constant A.

[9] The suppressed NSF as a result of coherent population trapping (CPT) can also be modeled based on the Fermi contact hyperfine interaction alone [OW18].
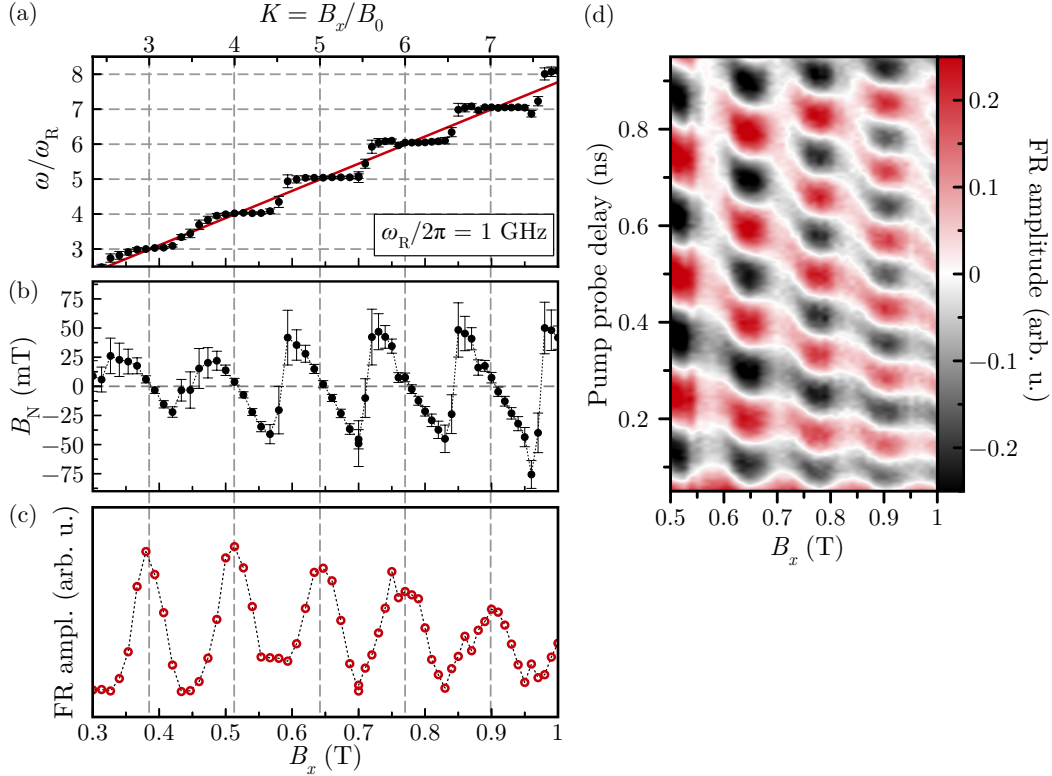
Figure 6.3: NS induced single ES precession frequency modes. Starting from 0.3 T, the magnetic field is ramped under 1 GHz pulsed illumination. Each 10 mT to 13 mT, a PP spectrum is taken with the 1 GHz laser and fitted with a single cosine function. (a) Precession frequency of the ESP depending on the external field B_x. The dotted lines give frequencies commensurate to the PRF. Below 0.6 T, the precession frequency mainly follows the external field determined Larmor frequency. Above 0.6 T, the NIFF forces the ESP on steps precessing with the closest frequency given by the PSC. The error bars give a standard deviation. (b) Average Overhauser field (OF) established for a given external field B_x. The OF is calculated as difference of the effective field causing the observed precession frequency and the external field. The error bars give the standard deviation gathered from the fitting process. (c) Amplitude of the ESP against the external field. The ESP is amplified on mode position and diminishes in between. Zero amplitude is along the y axis. (d) Contour plot of the PP spectra depending on the external field B_x. The FR maxima follow a step structure induced by the OF.

For magnetic fields larger than 0.6 T, the plateaus are pronounced and cover the whole external field range between $(K - 0.5)B_0$ and $(K + 0.5)B_0$ with the mode number K. The NS polarization efficiency is mainly dependent on the optical detuning [Car09] and becomes more efficient with increasing external field [DN08; Kop19]. As a result, a larger OF can be established. This is visualized in Fig. 6.3(b). The OF is calculated as the deviating field from the corresponding mode frequency. The single cosine fits of the PP traces also reveal, that the ESP is maximal on mode position and drops close to zero in between (see Fig. 6.3(c)). This is interpreted as individual QDs having an individual detuning and their ESP is amplified, if the individual OF allows to match a mode frequency. The formation of the precession frequency steps hints to a NIFF mechanism, which causes a considerable OF.

The frequency steps can also be visualized in a contour plot comprised of PP traces, which are plotted along the y axis (pump probe delay) with the external field B_x on the x axis. The FR is colored according to sign and intensity in Fig. 6.3(d). The maxima and minima form steps, which give a direct visualization of the constant precession frequency.
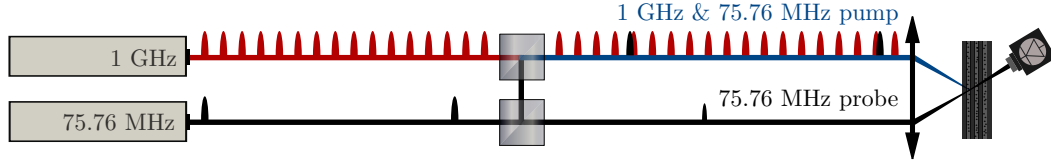
6.1.3 Two Laser Setup

Figure 6.4: Two laser setup for the experimental resolution of multiple 1 GHz ES precession modes. The 1 GHz laser pumps the ENSS. Simultaneously, the 75.76 MHz laser pulses act as pump and probe pulses. Both lasers are not synchronized, as their PRF is incommensurate. Only the ESP induced by the 75.76 MHz pump pulses are probed. This ESP precesses in the OF influenced by the 1 GHz laser.

In order to further study the effect of the frequency focusing on the ENSS, the ESP dephasing is studied in more detail. As it outscales the 1 ns PRP, the dynamics of the ES embedded in the NSS are registered using a 13.2 ns PRP PP setup. As depicted in Fig. 6.4, the 1 GHz laser runs on the pump path and is polarization-modulated (σ^+/σ^- with a frequency of 84 kHz) like the pump beam. The PRFs are incommensurate, and thus only the influence of the 1 GHz excitation on the NSP is detected in the 75.76 MHz PP trace (see Sec. 3.2.3 for further details). The average beam power before the cryostat for all measurements in the two laser setup in this chapter amounts to approximately $P_{\text{Pu}} = 5\,\text{mW}$ (power density $D_{\text{Pu}} = 5\,\text{W cm}^{-2}$), $P_{\text{Pr}} = 150\,\text{µW}$ ($D_{\text{Pr}} = 10\,\text{W cm}^{-2}$), and $P_{\text{GHz}} = 7\,\text{mW}$ ($D_{\text{GHz}} = 350\,\text{W cm}^{-2}$) unless stated otherwise. This two laser setup allows to probe the ENSS over a timescale of 13.2 ns. Figure 6.5(a) shows the 75.76 MHz PP traces at different external mode
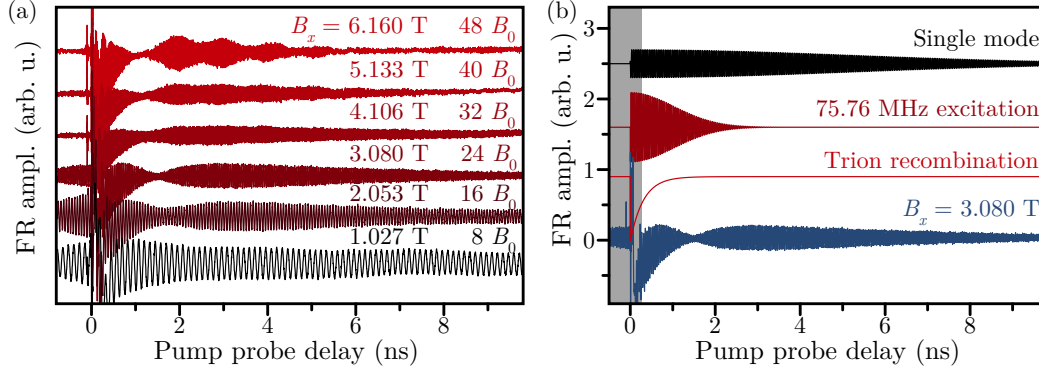
Figure 6.5: Few mode precession of the ESP induced by the 1 GHz laser with enhanced ESP dephasing time in the two laser setup. (a) PP traces at external fields B_x which are an integer multiple of the mode field B_0 with a g factor of $g = 0.557$. The external field is set before the sample is illuminated with the 1 GHz laser. Above $B_x = 40B_0$, the 1 GHz also covers multiple precession modes due to the g-factor inhomogeneity in the ensemble with one dominant frequency. (b) Components within the PP trace for $B_x = 3.080$ T. Apart from an offset, the PP trace consists of an exponentially decaying trion contribution, the multi-mode signal induced by the 75.76 MHz laser only (Gaussian decaying cosine) and the (dominant) single mode imprinted in the ENSS by the 1 GHz laser (exponentially decaying cosine). The gray area is not considered for the fit.

fields $B_x = KB_0$ in a degenerate setup: $E_{Pu} = E_{Pr} = E_{GHz} = 1.3867$ eV[10]. The 1 GHz pulsed excitation was blocked during the change of the external field. Each PP trace consists of three components (see Fig. 6.5(b)): (i) The trion recombination which is modeled by a single exponential decay, (ii) the ES precession modes resulting from the 75.76 MHz excitation of ESs, which do not run in the ENSS influenced by the 1 GHz laser, and (iii) the one (two) mode ES precession, which exhibits a long ESP dephasing time, only limited by the mode width[11]. The component (ii) is fitted by a Gaussian decay cosine according to Eq. (6.2), while (iii) is assumed to be an exponentially decaying cosine.

As seen in the EPP trace, the ESP dephasing time of (iii) exceeds 10 ns. For fields larger than 4 T, two modes appear and for an external field of 6.16 T three modes are visible. The ESP dephasing time depends on the external field, which will be investigated in the following section.

---

[10]For the degenerate setup, the negatively detuned QDs dominate the FR signal on mode fields [Eve21b].

[11]The beating in the FR amplitude in the first 1 ns to 2 ns of each PP trace is a result of the destructive interference of (ii) and (iii).

6.1.4 Suppression of Nuclear Spin Fluctuations

The ESP dephasing time when the ENSS is subject to a simultaneous 1 GHz excitation clearly exceeds the dephasing time without it at 1 T (see Fig. 6.6(a)). To compare the dephasing in different external fields, an additional series of PP traces is taken for the one laser, 75.76 MHz setup. The dephasing time of this series is given in Fig.6.6(b) (black curve). Both series are analyzed by

$$T_{2,\mathrm{e}}^* = \frac{\hbar}{\mu_\mathrm{B}} \frac{1}{\sqrt{(\Delta g_\mathrm{e} B_x)^2 + (g\delta B_\mathrm{N})^2}} \tag{6.2}$$

with the external field dependent component caused by the *g*-factor inhomogeneity Δg_e and the field independent component of the NSF δB_N [Yug09]. This equation is valid here as the pulses with a repetition frequency of 75.76 MHz are nearly π pulses. The NSF dominates close to zero external field and the *g*-factor spread drives the dephasing above 1.1 T. For external fields, where the long-dephasing component measured in the two laser setup consists of several modes, the dephasing time of the dominant mode is taken.
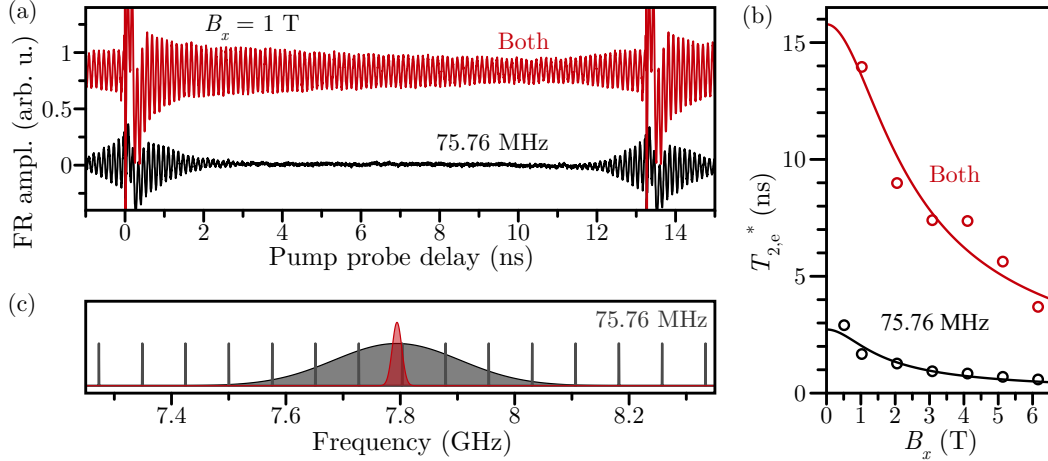
Figure 6.6: Reduction of the NSF and the *g*-factor spread. (a) TRFR spectra of the ESP under pumping with a PRF of 75.76 MHz only (black) and additional 1 GHz pumping (red) at $B_x = 1$ T. The black curve shows a fast dephasing ESP, while a single mode component with greatly enhanced dephasing time is present with the 1 GHz excitation. (b) Voigt field dependence of the ESP dephasing time $T_{2,\mathrm{e}}^*$. The lines are a fit according to Eq. (6.2). (c) Visualization of the contributing modes. The gray modes give all possible modes according to the PSC. The red and black shapes give the area with possible frequencies and amplitudes following the results of (b). Under pumping with 75.76 MHz only, 7 modes are covered while the pumping with the 1 GHz laser reduces the nuclear fluctuations such, that only 1 mode is excited (red).

Fitting the ESP dephasing time for the illumination with both lasers (red curve), one

finds the parameters $\Delta g_e = 4.2 \times 10^{-4}$ and $\delta B_N = 1.3\,\text{mT}$, and for the $75.76\,\text{MHz}$ only measurement, the fit yields $\Delta g_e = 4 \times 10^{-3}$ and $\delta B_N = 7.5\,\text{mT}$. The latter is consistent with previous findings for low external fields and low excitation power [Zhu18b]. The difference of one order of magnitude in the g-factor spread can be traced back to the single mode precession versus the multi mode precession.

Surprisingly, the NSF are reduced 5.8 times by exposing the ENSS to additional, non-synchronized laser pulses of $1\,\text{GHz}$ repetition frequency. The narrowing of the excitable ESP is depicted in Fig. 6.6(c). Note that the excitation with the $1\,\text{GHz}$ PRF laser does not filter the QDs that precess on the single mode, but homogenizes the precession frequencies in the QD ensemble by establishing a considerable OF. The total ESP is not reduced. This reduction is on a similar scale than the reduction achieved by CPT in single QDs [Xu08; Éth17; Onu16], which underlines, that ESs precessing on modes K can be understood as locked into coherent dark states of the pulsed excitation. In further perspective, the narrowed NSF is expected to enhance the ES coherence time [Gra16].

Remarkably, it is not necessary to alternate between the illumination with the $1\,\text{GHz}$ and the $75.76\,\text{MHz}$ laser in order to achieve the reduced NSF induced by the $1\,\text{GHz}$ excitation and the coherent ES precession caused by the $75.76\,\text{MHz}$ pump pulse simultaneously in one PP experiment. The best explanation to date is, that ESs are randomly excited by either laser as their PRF is incommensurate and that ESs in the dark state for one laser are not in a dark state for the other[12]. This would introduce an additional loss channel for the ESP and the determined ESP dephasing would be a lower limit[13].

Note that a model which only takes into account the collinear hyperfine interaction caused by the optical Stark effect predicts a reduction of the NSF by 2.5 [Eve21b]. The discrepancy to the experimentally determined reduction of 5.8 could be explained by a noncollinear hyperfine interaction stemming from quadrupolar moments in strained, self-assembled QDs, as investigated here [Urb13].

6.1.5 Preparing an Electron-Nuclear Spin System with Reduced Nuclear Spin Fluctuations

The NSP in InGaAs QDs is known to have a spin depolarization time in darkness of $T_{1,\text{n}} > 15\,\text{min}$ [Gre07], which drops to $T_{1,\text{ne}} \approx 1\,\text{s}$ [Mal07] under continued illumination at a temperature of $T = 6\,\text{K}$. The ENSS should therefore keep its single mode precession with reduced NSF for a considerable time without the $1\,\text{GHz}$

---

[12]Although the average power of the $1\,\text{GHz}$ excitation is higher than the average power of the $75.76\,\text{MHz}$ pump beam, the pulse area is only $\Theta = 0.2\pi$, while it is $\Theta = 0.9\pi$ for the $75.76\,\text{MHz}$ pump pulses. This limits the efficiency of the $1\,\text{GHz}$ excitation.

[13]It would also explain why the decoherence time measured by the ML amplitude as in Ref. [Gre06b] yields a much lower transverse relaxation time, when both lasers illuminate the sample simultaneously (not shown).

illumination[14]. The realization of such a setup is given by illuminating the sample for 15 s with the 1 GHz laser for an efficient NS polarization. Subsequently, the laser is blocked and, after a time of 0.3 s, the 75.76 GHz is opened to determine the ESP dynamics. During 1.5 s of 75.76 MHz illumination, ten steps on the mechanical delay line are measured. After another waiting time of 0.3 s, the 1 GHz illumination is continued for 15 s. The resulting PP trace at $B_x = 2.3$ T is shown in Fig. 6.7 together with an illumination diagram. The PP trace consists of the three components described in Sec. 6.1.4. The ESP dephasing time of the single mode component is reduced from 9 ns with simultaneous 1 GHz polarization to 5.6 ns, but still significantly larger than the 1.1 ns dephasing time without any 1 GHz ENSS preparation.
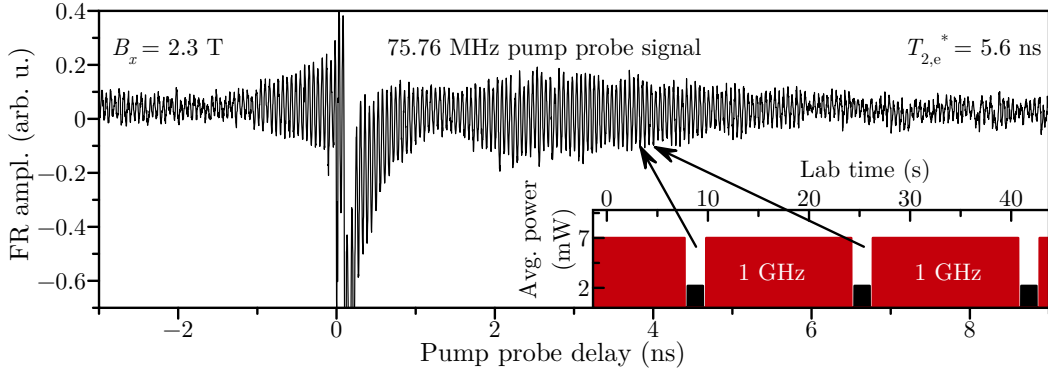

Figure 6.7: Lasting preparation of the NSS with the 1 GHz laser. The 1 GHz laser reduces nuclear fluctuations during an application time of 15 s for subsequent manipulation with a 75.76 MHz PRF laser source, while the 1 GHz laser source is blocked. The reduced fluctuations are preserved for at least 1 s of illumination with a laser source of arbitrary PRF, as evidenced by the increased $T_{2,e}^*$ compared to the $T_{2,e}^*$ without the preparation of the NSS (see Fig. 6.6(b)).

As a result, the NIFF induced by the 1 GHz laser can serve to prepare an ensemble of InGaAs QDs in a low dephasing, single mode regime whose ESP can be manipulated during a seconds timescale by arbitrary optical pulses. The NIFF leads to the build-up of a significant OF, which reduces the NSF. The following experiments focus to build-up an OF larger than half the difference between mode fields.

6.2 Electron Spin Mode Dragging and Mode Pick-Up

For now, the external field was driven without simultaneous illumination with a 1 GHz PRF. As suggested in Ref. [Car09], driving the external field under illumi-

---

[14]Reduced fluctuations persisting in the second range have so far been reported in Si-doped, thick GaAs films [Onu16] and in the millisecond range for charge-controlled, self-assembled InGaAs QDs [Éth17].

nation should lead to the build-up of an OF, which compensates the external field change and keep the ES precession on a constant frequency, even over a range larger than the mode separation B_0. It is referred to as (mode) dragging [Urb13] which was so far reported for single QDs, where either the absorption followed a spectral shift of the (cw) probe laser in a constant field [Lat09; Hög12] or the degree of circular polarization of a constant optical (cw) probe energy in a varied external field remained constant [Kre10].

However, in an ensemble of QDs the trion energy is inhomogeneous and thus the locking to a PRF while varying the external field B_x in Voigt geometry is used here. The ES precession frequency in the PP traces then shows the effective field for the ES. The results presented in this section have been partly published in Ref. [Eve21a].

6.2.1 Overhauser Field Build-Up by Driving the External Field

To study the OF build-up, a PP setup with the 1 GHz PRF laser only is used. The pump and probe pulses are negatively detuned as given by setup 5 in Fig. 6.15(a) ($E_{\mathrm{Pu}} = 1.3878\,\mathrm{eV}$ and $E_{\mathrm{Pr}} = 1.3867\,\mathrm{eV}$), with an average pump power right before the cryostat of $P_{\mathrm{Pu}} = 4\,\mathrm{mW}$ (power density $D_{\mathrm{Pu}} = 200\,\mathrm{W\,cm^{-2}}$) and an average probe power of $P_{\mathrm{Pr}} = 150\,\mathrm{\mu W}$ ($D_{\mathrm{Pr}} = 9\,\mathrm{W\,cm^{-2}}$). The external field B_x is increased in steps of 13 mT from a starting field $B_{\mathrm{S}} = 2.01\,\mathrm{T}$ with a speed of 6.1 mT/s (370 mT/min) in between. The closest mode field to the starting field is $B_x = 2.05\,\mathrm{T}$ with a mode number $K = 16$.

For all steps, the PP trace was measured. A selection of traces for even mode fields is shown in Fig. 6.8(a). At the field $B_x = 16B_0$, the ESP precesses on the single mode $K = 16$, as expected. When the external field reaches $B_x = 18B_0$, two beating nodes as a result of the interference of three simultaneous ES precession modes appear (see Sec. 2.5.1 for a visualization). The appearance of one additional beating node per overswept mode field can be spotted directly up to an external field of $B_x = 26B_0$[15]. As shown in Sec. 6.1.1, a dominantly single mode precession appears at this external field, when the external field is driven while the 1 GHz PRF laser is blocked.

All PP traces are analyzed further by fitting a number of single, non-decaying cosine functions to each trace. As expected, the best fit is reached with a number of cosine functions equal to the number of overswept mode fields (see Fig. 6.8(c))[16]. The frequencies of the cosine components fall on the PRF. The addition of a mode by oversweeping a mode field will be denoted mode pick-up. As the base mode (here

---

[15] For even higher field sweeps, the beating node structure breaks down, and a multi-mode structure similar to the ES ML forms. This hinders one to properly discern the individual modes (see Sec. 6.3.4).

[16] In the middle between two mode fields, an additional cosine component with the frequency corresponding to the external field appears.
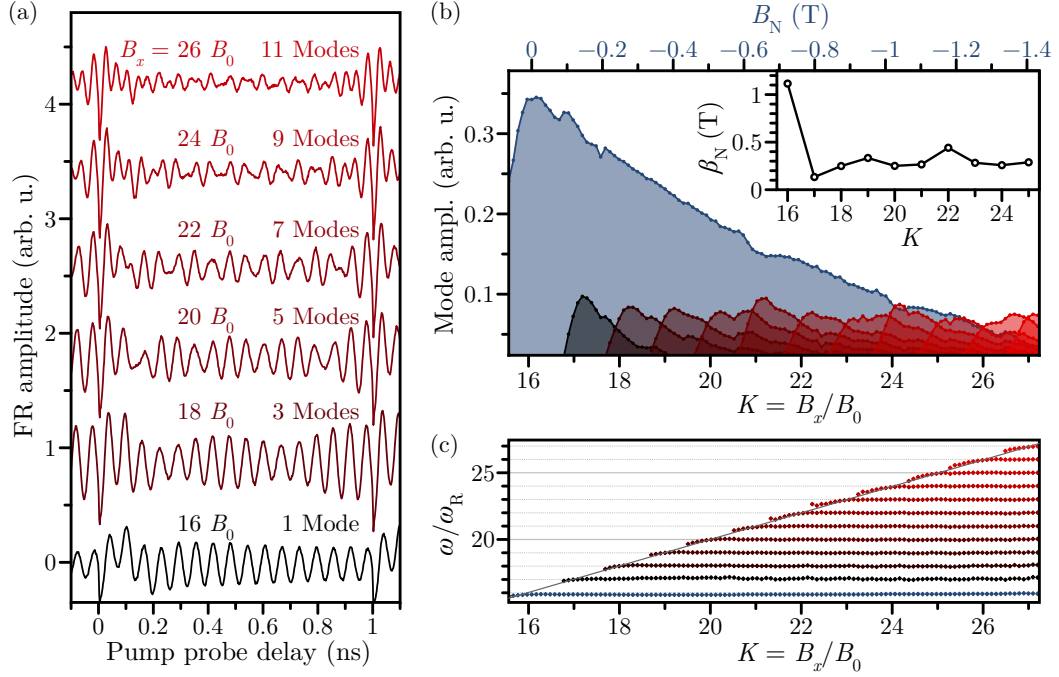
Figure 6.8: Mode dragging and pick-up by increasing the external field B_x under illumination with a 1 GHz PRF. (a) PP traces for different external magnetic fields of multiples of the mode field $B_0 = 0.128$ T. Starting from $B_x = 16B_0 = 2.01$ T, the number of modes increases to 11 modes, which corresponds to the number of overswept mode fields. The number of modes can be estimated by the number of precession nodes plus one. (b) Amplitude of different modes versus the external field. The PP traces are fitted with a number of cosine functions to extract the amplitudes. The modes diminish exponentially with a decay constant β_N (see inset). The first mode $K = 16$ (blue) is present up to 1.4 T higher than its original position, indicating an OF of $B_N = -1.4$ T in individual QDs. Note also, that the sum of all modes in all external fields stays constant. The upper x scale is only valid for the first mode $K = 16$. (c) Precession frequency of fitted cosines. The frequency settles on corresponding modes with multiples of the PRF ω_R. The frequency corresponding to the ES precession frequency in the external field is given as a gray line.

$K = 16$) is present in an external field $1.4\,\mathrm{T}$ higher than the corresponding field, mode dragging is observed.

Fitting the cosine components to the PP traces also reveals the dependence of the mode amplitudes on the external field (shown in Fig. 6.8(b)). The starting mode (blue) reaches its maximum at the corresponding external field. The amplitude diminishes exponentially with a decay constant of $\beta_\mathrm{N} = 1.12\,\mathrm{T}$ with increasing external field. The second mode appears in between the first and the second mode field and builds up until the maximum is reached at the second mode field. It then diminishes with $\beta_\mathrm{N} = 0.13\,\mathrm{T}$. This pattern repeats for all additional modes, but with a similar decay constant of $\beta_\mathrm{N} = 0.35\,\mathrm{T}$. Note that the maximal amplitude of the first mode gives the sum of all mode amplitudes for all external mode fields. This can be interpreted such, that the number of polarized ESs remains constant throughout all external mode fields and the ESP redistributes into the observed mode structure.

The mode dragging and mode pick-up can be modeled by taking into account the collinear hyperfine interaction between the ES and the NSs [Eve21a] and is only outlined briefly here. The model takes into account several features: (i) The trion resonance in the ensemble of QDs is inhomogeneous, (ii) the maximal OF, which can be realized in a QD using the PRF locking depends on the optical detuning from the pump energy of an individual QD[17], and (iii) once this maximal OF is reached, the NSP breaks down and the ES precesses on the frequency given by the corresponding external field [Kre10; Kor11]. It is assumed, that a single ES in one QD does not jump in between modes in a constant external field (the depolarization time of NSs is in the seconds range [Mal07]). One can therefore also exclude, that a single ES precesses in a superposition of all possible modes. In an intuitive picture, only QDs with the right detuning can be dragged over a large external field range. The NSP of QDs with an improper detuning breaks down at different fields and starts to build-up once again[18]. Only the NSP in fitting QDs in the mode $K = 16$ does not break down. That would make the mode dragging an effect of single QDs, while the mode pick-up is assumed to be an ensemble effect.

Although the discernible OF of $-1.4\,\mathrm{T}$ is only $22\,\%$ of the maximal OF, the decay constant β_N for the base mode K_S indicates that 400 QDs out of the excited 10^5 QDs could reach $100\,\%$ NSP. The maximal OF $B_\mathrm{N,max}$ can be estimated in the QDs used by calculating [MER02]

$$B_\mathrm{N,max} = \sum_\mathrm{j} \frac{I_\mathrm{j} A_\mathrm{j} a_\mathrm{j} n_\mathrm{QD,j}}{g_\mathrm{e} \mu_\mathrm{B}} = 6.23\,\mathrm{T} \tag{6.3}$$

---

[17] In the model, this is realized by an OF-dependent NS polarization time due to interaction with electrons $T_{1,\mathrm{ne}}$.

[18] Note that the decay constant for the second mode is similar to the mode separation B_0. These QDs experience the NSP breakdown even for the first mode and, hence, experience the break down again from the second to the third mode. Their detuning might allow only the formation of precession frequency steps as shown in Sec. 6.1.2.

with the index j running over all present isotopes of Indium (^{113}In, ^{115}In), Gallium (^{69}Ga, ^{71}Ga), and Arsenic (^{75}As), the NS I_j, the hyperfine constant A_j, the natural abundance a_j, and the respective fraction of the nuclear species (In, Ga, As) in the primitive cell $n_{QD,j}$. The numerical values are given in Table 6.1. The fractions of In and Ga are roughly estimated along the findings in Ref. [Pet08]. Note that for full NSP, the OF can be calculated as if the electron is localized within one primitive cell. The model developed in Ref. [Eve21a] suggests to increase the fraction of

Table 6.1: Parameters of the NS system in this QD sample. The NS I_j, the hyperfine interaction A_j, the natural abundance a_j, and the fraction of the primitive cell of this nuclear species $n_{QD,j}$ are given.

	I_j [Hay12]	A_j [Che17]	a_j [Hay12]	$n_{QD,j}$
^{113}In	4.5	56 μeV	4 %	20 %
^{115}In	4.5	56 μeV	96 %	20 %
^{69}Ga	1.5	43 μeV	60 %	30 %
^{71}Ga	1.5	55 μeV	40 %	30 %
^{75}As	1.5	44 μeV	100 %	100 %

the dragged OF closer to the maximal OF by tweaking the pump probe detuning according to the built up OF at a given external field.

The two laser setup allows one to measure the ENSS over multiples of the 1 GHz PRF, and the application of a FFT on the longer dynamics then directly reveals the constituent modes. The 75.76 MHz pump and probe pulses are degenerate $E_{Pu} = E_{Pr} = 1.3867$ eV, while the energy of the 1 GHz excitation is set to $E_{GHz} = 1.3878$ eV. The energies are set such that the 75.76 MHz PP energy equals the probe energy and the 1 GHz excitation energy equals the pump energy given in setup 5 in Fig. 6.15(a). The average powers equal the powers given in Sec. 6.1.3.

The PP traces for different configurations are given in Fig. 6.9(a). The $B_x = 2$ T (black) and the top $B_x = 3.5$ T curve (red) are measured by driving the external field to $B_x = B_S$ in darkness. The 1 GHz excitation is only applied once the external field $B_x = B_S$ is reached. The FFT, as shown in Fig. 6.9(b), reveals a (dominantly) single mode precession with frequencies corresponding to the external field (black and red). The bottom curve (blue) in Fig. 6.9(a) shows the ES dynamics, when driving the magnetic field under 1 GHz illumination from $B_S = 2$ T to $B_x = 3.5$ T with a speed of 6.1 mT/s. A beating pattern appears, whose rephasing maxima are separated by the PRP $T_R = 1$ ns. Consequently, the FFT (see Fig. 6.9) shows a number of constituent ES precession modes, each separated by the PRF $\omega_R/2\pi = 1$ GHz. Only the modes covered by the external field sweep under 1 GHz illumination show up. As seen for the modes in the 1 GHz PP experiment (see Fig. 6.8(b)), the mode amplitudes get exponentially smaller from the mode corresponding to the external field B_x to lower modes with the exception of the starting mode $K = 16$. The two laser setup allows the direct measurement of the mode dragging of up to $B_N = -1.4$ T without
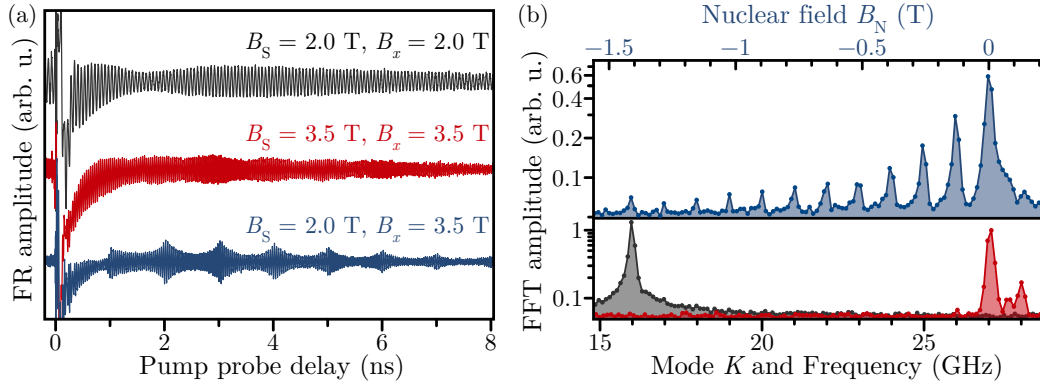
Figure 6.9: Mode dragging and pick-up in the long dynamics of the 75.76 MHz PP trace. (a) ESP dynamics measured by TRFR under simultaneous illumination with a 1 GHz laser in the two laser setup. The PP traces are given for constant external fields measured at the starting field $B_S = B_x$. Only one dominant mode is present for $B_x = 2$ T (black) and $B_x = 3.5$ T (red). When increasing the external field from $B_S = 2$ T to $B_x = 3.5$ T under 1 GHz illumination (blue), constructive interference of the ESP shows up, separated by 1 ns at an external field of 3.5 T. (b) Fast Fourier transform (FFT) spectra of the PP traces. While the spectra at constant external fields show one dominant mode (black, red), driving the external field polarizes all modes between the aforementioned modes. The two laser setup offers the resolution required to resolve the modes directly. The lowest mode is dragged for 1.4 T, indicating an OF of -1.4 T in some QDs. Note the logarithmic scale on the y axis.

relying on the multiple cosine fit within one PRP. Moreover, the mode dragging even persists under constant illumination with an incommensurately pulsing laser source. The dragging over $B_N = -1.4$ T is among the largest reported in a perpendicular external field [Urb13; Hög12][19].

6.2.2 Stability of the Driven Nuclear Spin System

A series of 1 GHz PP experiments shows the basic behavior of the ENSS under constant 1 GHz illumination and the decay of the OF in darkness[20]. The pump and the probe energies and average powers are equal to the settings in Sec. 6.2.1. To show that a build-up of NSP over illumination time at a single external field is not the cause of the OF, a simple experiment is conducted: All light is kept open while the external field was not varied. As shown in Fig. 6.10(a), the PP trace does not change with lab time, from two minutes of illumination at an external field of $B_x = 3.213$ T to 28 minutes.

---

[19]In spectral dragging as in CPT experiments, the dragging is given in µeV. To transform the OF measured here to the CPT dragging, the equation $E_{Drag} = g_e \mu_B B_N$ [Urb13] is used.

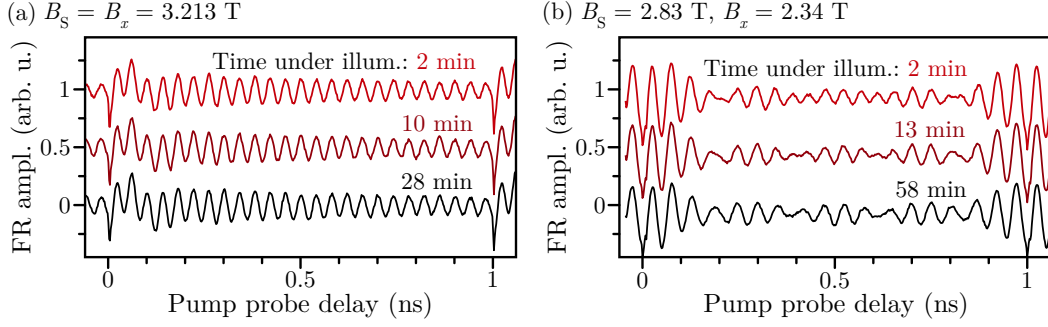[20]Both pump and probe beam are blocked.

Figure 6.10: Stability of the ES precession mode structure under illumination. (a) No additional modes only due to the long illumination of the sample appear. The sample is exposed to the 1 GHz illumination at the external field 3.213 T only for the time indicated, without changes to the PP trace within 28 min. (b) Additional modes are stable under 1 GHz illumination for 1 h. Under 1 GHz illumination, the external field is decreased from $B_S = 2.83$ T to $B_x = 2.34$ T. The PP traces show the same superposition modes for the indicated illumination time.

To investigate the decay of the built-up OF, the external field is driven from $B_S = 2.83$ T to $B_x = 2.34$ T with a speed of 6.1 mT/s under 1 GHz illumination. The illumination is kept open for up to one hour and the PP is measured continuously (see Fig. 6.10(b)). It is verified, that driving the external field down under 1 GHz pulsed illumination also leads to mode dragging and pick-up (see Sec. 6.3.1 for details). The beating structure in the PP trace after 58 minutes resembles the beating structure after 2 minutes. The OF persists over one hour under constant 1 GHz illumination. As a result, the OF can be build-up well controlled and persists as long as the illumination is not blocked. If the sample is kept in darkness after driving the magnetic field from $B_S = 2.83$ T to $B_x = 2.34$ T under 1 GHz illumination, however, the beating pattern will disappear within 30 minutes as depicted in Fig. 6.11. For each time in darkness, the ENSS is set up from scratch and the beams are closed for the indicated time.

To analyze the decay of each mode, the 1 GHz PP traces are fitted with multiple cosines. Five modes are identified in the original PP trace, from the starting mode $K_S = 22$ to the mode corresponding to the external field B_x, $K_x = 18$. After 30 seconds, all modes except for the corresponding mode K_x diminished in amplitude, but are still present. For longer dark times, the modes decay one by one. The higher the necessary OF to sustain the mode, the faster the mode disappears. Note that the decay of each mode lower than the base mode does not reflect the actual decay of the OF responsible for that mode. The OF relaxes such, that the ESP of higher modes relax into lower modes. The corresponding mode K_x gains amplitude up to 20 minutes of dark time as the ESP redistributes. It is evident, however, that the OF persists on the minutes timescale in darkness, as expected [Gre07], which allows to implement an alternative NSP protocol that does not require a large driving range of the external field.
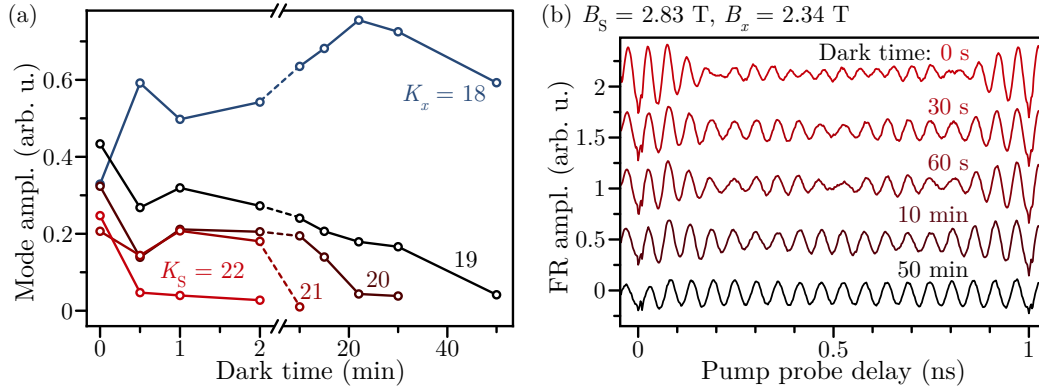
Figure 6.11: Stability of the different precession modes without illumination. (a) The precession mode amplitudes in the PP trace, after decreasing the external field from $B_S = 2.83\,\text{T}$ to $B_x = 2.34\,\text{T}$, range from the starting mode $K_S = 22$ to the mode fitting to the external field $K_x = 18$, depending on the time in darkness. With increased time in darkness, the modes drop out one by one, vanishing the earlier the higher the necessary OF is to maintain that mode until the whole ESP can be found in K_x. Note the two different scales and ranges on the x axis. (b) PP traces after different times in darkness. For each trace, the initial mode structure has been reestablished by driving the external field down from $B_S = 2.83\,\text{T}$ to $B_x = 2.34\,\text{T}$.

6.2.3 A Typewriting Protocol for the Electron-Nuclear Spin System

The previously described mode dragging requires that the external field is driven by the same amount as the OF is built up. The typewriter protocol lifts this restriction. Its principle is shown in Fig. 6.12. Surprisingly, the NSP persists not only in darkness, but also when driving the external field in darkness. To demonstrate the implications, four modes are written by increasing the external field from 2.8 T to 3.2 T with a speed of 6.1 mT/s (bottom curve). The curves give the FFT acquired by the two laser setup and the laser energies and average beam powers are set as given in Sec. 6.1.3 (optically degenerate). Subsequently, all lasers are blocked and the external field is driven down over three mode fields (0.3 T) with a speed of 6.1 mT/s. All modes are pushed to lower external fields. When again increasing the external field under 1 GHz illumination, additional modes are imprinted into the ENSS and the NSP of the previously written modes is increased to compensate the increasing external field. This can be repeated, the existing modes can be pushed to lower ES precession frequencies, and a new line of modes can be written[21]. To explore

---

[21]One could come to the idea that driving the field down for 65 mT in darkness and up for 65 mT under illumination would lead to the shift of a single mode. The result, however, is a single mode precession on the mode corresponding to the external field K_x (not shown). Mode dragging requires that a mode is polarized to adjust the NSP to it as the ENSS will otherwise adjust to the fitting, corresponding mode K_x. This typewriting protocol also highlights that it is not possible to block the 1 GHz excitation while the external field is driven over a mode field to

Figure 6.12: Typewriting ES precession modes in the ENSS of an ensemble of QDs. The curves show FFT spectra of the PP trace measured by the 75.76 MHz laser. The build-up of the mode spectrum happens from bottom to top. Under illumination with the 1 GHz laser, the external field is driven up from 2.7 T to 3.2 T (red arrow). All covered modes are imprinted in the ENSS. Without 1 GHz illumination, the field is driven down to 2.9 T (black arrow). The modes are pushed to lower precession frequencies without the polarization of additional modes, which enables the subsequent writing of additional modes to the ENSS. It allows for a typewriter style of the NS polarization.
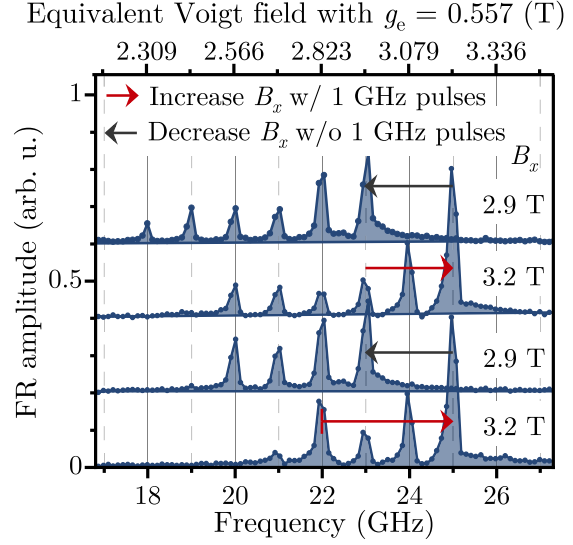
the limits of the typewriting protocol with a fixed optical pump probe detuning, multiple lines are written in sequence, as shown in Fig. 6.13. The 75 MHz laser is blocked during the typewriting protocol and only opened to trace the ESP dynamics after ten lines. Twelve ES precession modes show up in the FFT. Each written line adds two modes as depicted by the range of the arrows (driven external field range) in Fig. 6.13. Although the cycle is repeated ten times, only modes corresponding to 6 lines are written. The built up OF of $-1.4\,\text{T}$ corresponds to the limit discussed in Sec. 6.2.1. The pump probe detuning, which allows the maximal OF, depends on the built up OF and the external field [Eve21a]. In contrast to the build-up by mode dragging, the typewriting protocol does not require a large change in the external field and does, thus, promise to optimize the optical detuning to the built up OF alone. Moreover, it could be implemented in fixed large field devices with an additional, small electromagnet like in widely available NMR cryostats.

---

drag only a single mode and to avoid the polarization of additional modes for the same reason: The NSP does not increase without illumination and the ES precession frequency ends up on the closest mode. The ENSS is not dragged.
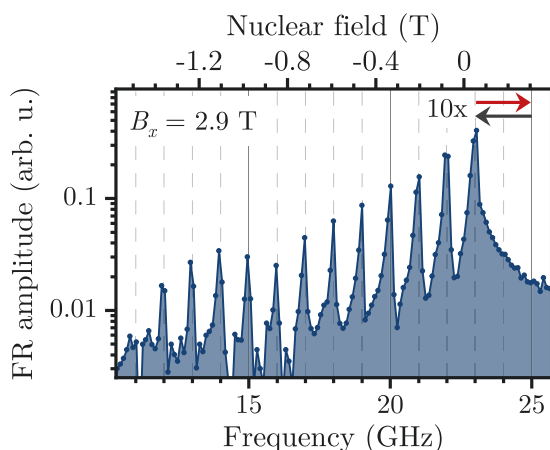
Figure 6.13: Typewriting eleven ES precession modes and a nuclear field of $-1.4\,\text{T}$ by cycling the external field between $2.9\,\text{T}$ and $3.2\,\text{T}$ ten times up under pulsed, $1\,\text{GHz}$ illumination (red arrow) and down in darkness (black arrow). The curve is an FFT spectrum of the PP spectrum by the $75.76\,\text{MHz}$ laser with underlying illumination of the $1\,\text{GHz}$ laser at a final external field of $B_x = 2.9\,\text{T}$. Note the logarithmic scale of the y axis and the ten-fold difference in amplitude of the lowest and highest ES precession mode.

6.3 Additional Findings

The observations of the studied $1\,\text{GHz}$ PRF excitation presented so far show the results under optimized experimental conditions. These conditions, however, are chosen after exploring the parameter space. Some of these explorations are shown in the following to consolidate the experimental observations.

6.3.1 Decreasing the External Field under Illumination

Previous studies of the spin dragging effect unanimously report dragging in both external field [Kre10] or spectral dragging [Lat09; Hög12] directions[22]. As already hinted at in Sec. 6.2.2, driving the external field down also adds additional precession modes by locking the ES precession to a PRF. A full mode dragging picture by decreasing the external field is given in Fig. 6.14 by using a $1\,\text{GHz}$ PP setup. The optical detuning is set such that it fits setup 5 in Fig. 6.15(a). The average powers right in front of the cryostat are set to $P_{\text{Pu}} = 7\,\text{mW}$ (power density $D_{\text{Pu}} = 350\,\text{W/cm}^2$) and $P_{\text{Pr}} = 120\,\text{µW}$ ($D_{\text{Pr}} = 7.5\,\text{W/cm}^2$). Selected PP traces from the starting field $B_{\text{S}} = 4.49\,\text{T}$ to $B_x = 3.697\,\text{T}$ are shown in Fig. 6.14(a). All PP traces are fitted with a number of cosine functions, which reveals the constituent ES precession modes. The mode amplitudes to the selected PP traces are depicted in the right panel. One can spot that, at the starting field (which is exactly at the external field for mode $K = 35$), the starting mode dominates, but that the next lower mode is marginally excited as well. With decreasing external field, additional precession modes appear when the corresponding external field is overswept (see Fig. 6.14(b) for the constituent frequencies). The mode amplitudes and their decay

---

[22]Positive and negative optical detuned excitation from the trion resonance, however, do not both show dragging equally [Hög12]. This is investigated for the NS polarization scheme used here in the next section.
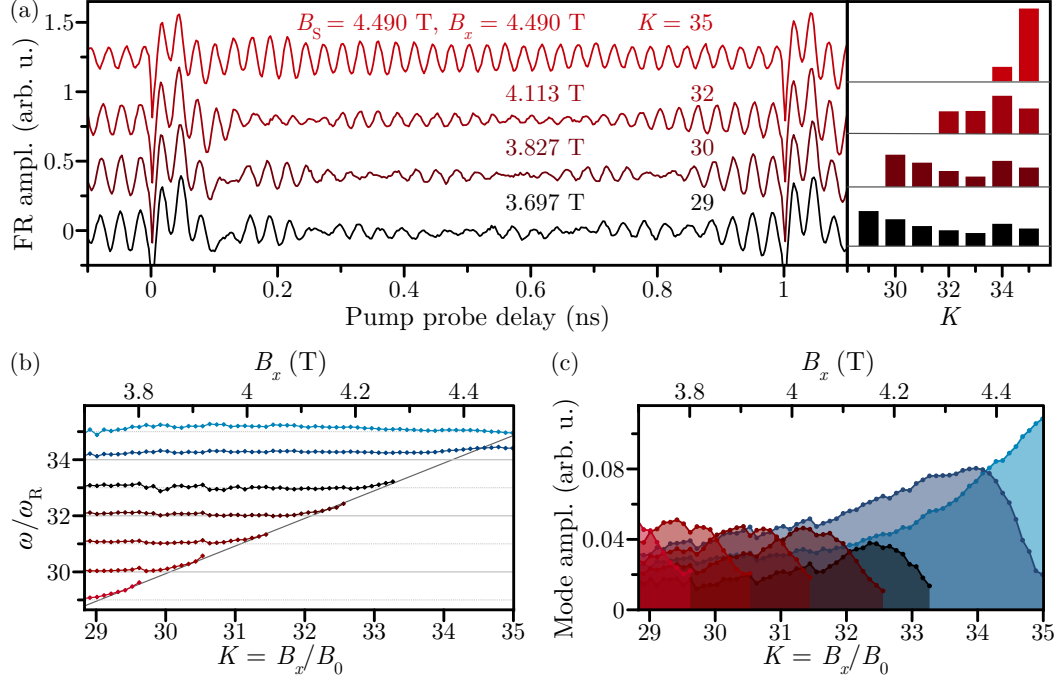
Figure 6.14: Mode dragging and pick-up by decreasing the external field B_x and illumination with a 1 GHz PRF. (a) PP traces from a starting field $B_S = 4.49\,\mathrm{T}$, mode number $K = 35$. Decreasing the external field adds all overswept modes to the final PP trace. The right panel shows the amplitude of the constituent modes in each trace. The amplitudes are derived by a fit of multiple cosines to the PP traces. (b) The ES precession frequencies settle on multiples of the mode frequencies ω_R. (c) Amplitudes of the constituent modes with decreasing external field. The starting field exactly corresponds to the mode number $K = 35$.

with decreasing external field is shown in Fig. 6.14(c). The modes $K = 35$ and $K = 34$ show a decay constant of $\beta_N = 0.2\,\mathrm{T}$ and $\beta_N = 0.6\,\mathrm{T}$, respectively. The stark contrast to the mode dragging with increasing external field ($\beta_N = 1.1\,\mathrm{T}$ for the starting mode) could be caused by starting the external field sweeping on a mode field. Neither mode can reach its full NIFF and as such not the full reduction of the NSF. The decay constant of the lower modes are similar to the case of the higher modes with increasing external field.

6.3.2 Influence of the Pump Probe Detuning

To clarify the role of the pump probe detuning on the observed single mode ES precession on the one hand, and the mode dragging and the mode pick-up on the other hand, data which is already discussed partly is presented here from a different perspective. The optical energy of the pump and probe pulses as well as the detuning between the two has several additional implications on the measured FR signal: (i)

the number of optically active QDs varies for different optical energies, (ii) the FR amplitude varies depending on the optical PP detuning, and (iii) the build-up of the OF depends on the optical detuning both in achievable OF and direction, as discussed in Sec. 6.2.1.
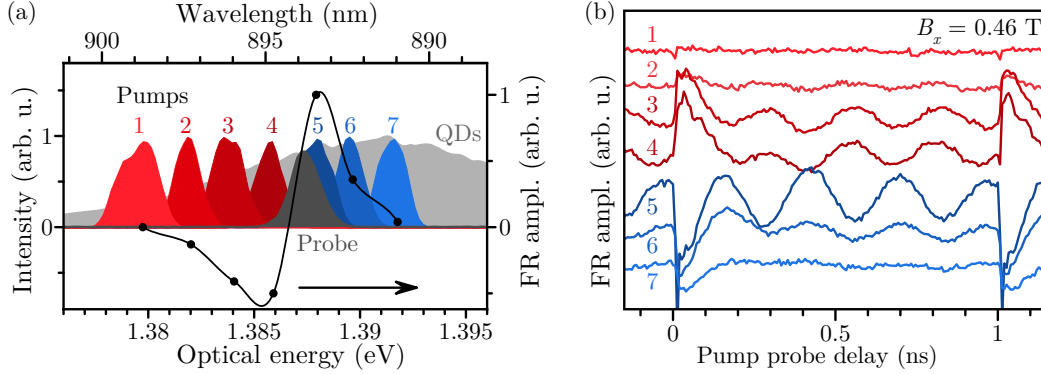

Figure 6.15: FR amplitude dependence on the optical detuning between pump and probe pulse energy using a 1 GHz PP setup. (a) Pump and probe pulse spectra with respective FR amplitude. The probe central energy (dark gray) is fixed on the low energy flank of the QD ensemble (light gray, at 5.2 K and an external field of $B_x = 0$ T). Pump pulses with different central energies (labeled with arabic numerals) excite the respective QDs. The resulting FR amplitude at an external field of $B_x = 0.46$ T is given in black. The sign reflects the inverted ES precession phases. The FR amplitude shows a dispersive profile on the optical pump probe detuning. The line is a guide to the eye. (b) PP traces for different optical detunings at an external field of $B_x = 0.46$ T. The ES precession phase inverts between positive detunings (red) and negative detunings (blue).

(i) The energy distribution of the number of QDs with a given trion excitation energy can be elucidated by measuring the PL of the QD ensemble. It is shown for the sample used (#11955-945) in Fig. 6.15(a) by the gray area at a temperature of $T = 5.2$ K in an external field of $B_x = 0$ T. The optically active QDs follow a Gaussian distribution around the central energy 1.3908 eV, with a FWHM of 17 meV. The FWHM of the pump and probe pulse spectra is tenfold smaller with approximately 1.5 meV.

(ii) To determine the FR of the probe pulses in dependence of the optical detuning from the pump energy, the probe energy is fixed and PP traces are taken for seven different pump energies at an external field of $B_x = 0.46$ T (see Fig. 6.15(b)). The average pump power amounts to $P_{\mathrm{Pu}} = 7$ mW (power density $D_{\mathrm{Pu}} = 350$ W/cm^2) and the average probe power to $P_{\mathrm{Pr}} = 200$ µW ($D_{\mathrm{Pr}} = 12.6$ W/cm^2). By fitting a single cosine function to each of the traces, the FR amplitude as well as the phase is determined. A clear phase shift of π occurs between positive and negative optical detuning (positions 4 and 5), which is interpreted as a change of the FR amplitude sign. The resulting dependence of the FR amplitude on the optical energy is given

in Fig. 6.15(a) by the black dots. It follows the known dispersive profile [Gla10], only distorted by the larger number of optically active QDs towards the blue-shifted central pump energies.
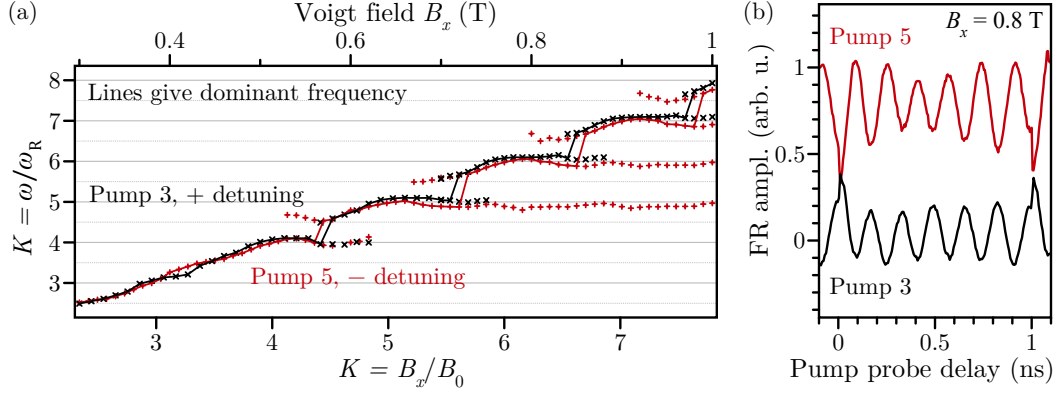

Figure 6.16: Build-up of the OF for positive and negative optical detuning. Pump 3 (black) and Pump 5 (red) are denoted according to 6.15(a). (a) ES precession frequencies in the PP trace after driving the external field (top axis) under $1\,\mathrm{GHz}$ illumination. Both detunings show a step-like behavior of the dominant ES precession frequency, seen by the plateaus of it around integer mode number fields. For a negative detuning, however, starting from a field corresponding to mode $K = 5$, the mode is dragged to higher fields while higher modes are dominant. For a negative detuning, the lower mode vanishes close to the next mode. (b) PP traces using the $1\,\mathrm{GHz}$ laser only for the different detunings at an external field of $B_x = 0.8\,\mathrm{T}$. Apart from the inverted oscillation phase, the red trace shows a superposition of two modes while it is absent in the black trace.

(iii) To add to the discussion of the role of the pump probe detuning direction, a series of $1\,\mathrm{GHz}$ PP traces is registered for a positive detuning (pump position 3 in Fig. 6.15(a)) and for a negative detuning (pump position 5). To evaluate the constituent ES precession frequencies, a number of cosine functions is fitted to the resulting PP traces. All fits are carried out with initially four independent cosine functions, but whenever the amplitude of one drops below 10^{-4}, the fitting procedure is repeated with three cosine functions, and so forth. The frequencies of all constituent cosine functions are plotted against the external field B_x (mode field k) in Fig. 6.16(a).

For the positive detuning (black crosses), a single cosine function mostly suffices to describe the PP traces. Up to an external field of $B_x = 0.5\,\mathrm{T}$, the ES precession frequency follows the linear dependence $\omega_\mathrm{L} = g_\mathrm{e}\mu_\mathrm{B}B_x$. Above $0.5\,\mathrm{T}$, precession frequency plateaus form around mode fields with the corresponding mode frequency and no second cosine component coexists at the center of the plateaus (as discussed in Sec. 6.1.2). The OF only builds up to half the mode separation $B_\mathrm{N} < {}^{B_0}\!/_2$. The component with the highest amplitude (dominant frequency, give by the black line in Fig. 6.16(a)) jumps just in between the mode fields close to the next ES precession

mode frequency. As an example for the single mode precession, the PP trace at an external field of $B_x = 0.8\,\text{T}$ is shown in Fig. 6.16(b). A single ES precession frequency without a beating node is traced for an excitation at pump position 3.

For the negative detuning (red crosses), the ES precession frequency also linearly depends on the external field up to 0.5 T. Above, the dominant precession frequency also forms plateaus around mode fields (red line). Starting from mode $K = 5$, however, the lower precession modes persist in the signal up to at least $B_x = 1\,\text{T}$. The OF builds up larger than half the mode separation $B_N > {}^{B_0}/2$, and mode dragging as well as mode pick-up is observed. This can be spotted directly in the PP trace by a beating node at an external field of $B_x = 0.8\,\text{T}$ (see Fig. 6.16(b), red trace). The difference in the OF pick-up for red and blue detuned pump pulses is analog to the build-up of the OF using the red and the blue Zeeman transition in single QDs CPT experiments. Driving the red Zeeman transition, the OF does not build-up and only the blue Zeeman transition could be dragged [Hög12]. The common reasoning is that a red detuning leads to a focusing on half-integer modes (driving the precession frequency away from the mode frequency) while the blue detuning leads to a (de)focusing on integer modes both in cw CPT schemes [Onu16] as well as in pulsed excitation [Car09]. While this is indeed observed in Sec. 5.2.2 by excitation with a 75.76 MHz pulsed laser, the plateaus in Fig. 6.16(a), excited with 1 GHz PRF, lie on integer mode frequencies for red and blue detuned pump pulses[23]. This discrepancy remains an open question and asks for further studies.

6.3.3 Influence of the Field Sweeping Rate and the Field Angle

Several other parameters for the ES mode dragging can be investigated from which the external field sweeping rate and the external field angle deviation from Voigt geometry is presented here. For both investigations, 1 GHz PP traces are measured at $B_S = 2.0\,\text{T}$ and at $B_x = 2.6\,\text{T}$, with the external field increased under 1 GHz pulsed illumination. The average pump power is set to $P_{\text{Pu}} = 7\,\text{mW}$ (power density $D_{\text{Pu}} = 350\,\text{W/cm}^2$) and the average probe power to $P_{\text{Pr}} = 130\,\text{µW}$ ($D_{\text{Pr}} = 8.2\,\text{W/cm}^2$).

The sweeping rate measurements are carried out using pump position 5 in Fig. 6.15(a). The studied sweeping rates range from $\Gamma_{\text{Bx}} = 0.4\,\text{mT/s}$ to $\Gamma_{\text{Bx}} = 6.1\,\text{mT/s}$[24] and the constituent mode amplitudes at $B_x = 2.6\,\text{T}$ are depicted in Fig. 6.17(a). The mode dragging efficiency is evaluated by the amplitude ratio between the starting mode $K_S = 16$ (black) and the final mode $K_x = 21$ (red). No dependence of the mode dragging efficiency on the external field sweeping rate is observed in the

---

[23] The electronic g-factors for the pump position 3 and 5 are similar because the slope of the linear ES precession frequency increase below 0.5 T is similar.

[24] The sweeping rate of 6.1 mT/s is the maximum sweeping rate of 370 mT/min of the used magneto-cryostat.
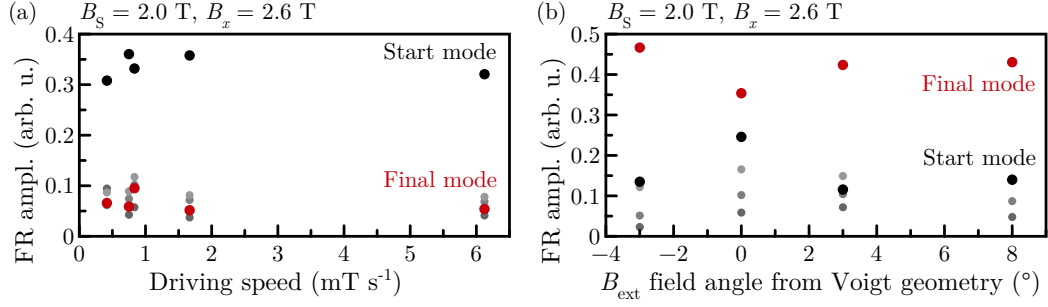
Figure 6.17: Dependency of the OF build-up on the external field sweeping rate (a) and on the B_{ext} field angle (b). (a) OF build-up independent of the investigated sweeping rates. The external field is increased from $B_{\mathrm{S}} = 2\,\mathrm{T}$ to $B_x = 2.6\,\mathrm{T}$ under $1\,\mathrm{GHz}$ illumination, using a field sweeping rate of up to $6.1\,\mathrm{mT/s}$ ($370\,\mathrm{mT/min}$). The amplitude of the start mode in the PP trace at the final field remains constant. (b) OF build-up optimized at pure Voigt field. Each measurement is carried out as in (a), only with a slightly different, negative detuning. The external field B_{ext} was varied by rotating the axis of the superconducting coil pair. The start mode is preserved best without a longitudinal field component.

investigated range. This is remarkable[25]. It does not contradict, that the sweeping rate is expected to be limited to the lower end by the NS depolarization time $T_{1,\mathrm{n}}$ and to the higher end by the NS polarization time due to electron-nuclear interaction $T_{1,\mathrm{ne}}$. As shown for the typewriter scheme (see Sec. 6.2.3), the polarization and dragging of modes only takes place when driving to the next mode field and it is safe to assume, that the NS polarization takes place over the dragging of a mode field B_0. Therefore the sweeping rate should be in the range

$$\frac{B_0}{T_{1,\mathrm{n}}} < \Gamma_{\mathrm{Bx}} < \frac{B_0}{T_{1,\mathrm{ne}}}$$

for efficient mode dragging. $T_{1,\mathrm{n}}$ is in the minutes to hours timescale and $T_{1,\mathrm{ne}}$ depends on the already built up OF [Ebl06] ranging from $T_{1,\mathrm{ne}} = 0.1\,\mathrm{s}$ to $1\,\mathrm{s}$ for no OF [Mal07][26] to $T_{1,\mathrm{ne}} = 0.1\,\mathrm{ms}$ for full NSP [Eve21a]. This needs experimental investigation, however, and could be achieved by either very slow or fast sweeping or by varying B_0 (as a NS inertia measurement, analog to the ES inertia experiments [Hei15; Zhu18b]).

The dependence of the dragging efficiency on the external field angle deviation from the Voigt geometry is measured using the optical detuning setup 6 in Fig. 6.15(a). The external field B_{ext} is increased with a speed of $0.4\,\mathrm{mT/s}$. To vary the external

---

[25]The fastest high OF dragging rate in CPT experiments known to the author amounts to an equivalent of 1.6 mT/s [Hög12].

[26]The value of $T_{1,\mathrm{ne}}$ also depends on the excitation power and the PRF and the range given here is valid for low power, cw excitation. However, in the experiments described here, the value seems to be in the same ballpark.

field angle, the cryostat is rotated by a given amount, while the sample surface is kept perpendicular to the ingoing pump beam[27]. As depicted in Fig. 6.17(b), the ratio of start to final mode (dragging efficiency) is largest for 0° i. e. for a pure Voigt configuration. Hereby, it is also shown that the OF by PRF locking is not induced with the help of an uncompensated longitudinal field.

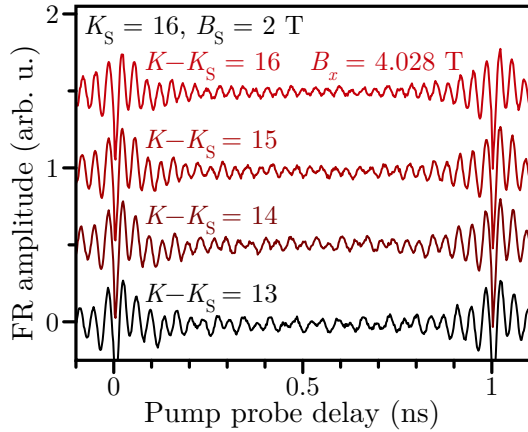### 6.3.4 Mode Dragging for Large Dragged Fields

Figure 6.18: Transition of the multimode precession to the precession with a decaying envelope of the FR. The 1 GHz PP traces are given at an external field B_x increased from $B_S = 2$ T by 13 to 16 B_0. While the PP trace to $K - K_S = 13$ (the external field is increased by $13B_0$ from B_S) shows a superposition pattern with beating nodes, the trace to $K - K_S = 16$ shows a decay of the FR envelope with a single (average) frequency.

Once the sweeping of the external field exceeds 1.5 T, the base mode can not be discerned anymore in the setup used as described in Sec. 6.2.1. Upon further increasing the external field, the multi-mode ES precession persists but the beating nodes disappear and a single (average) frequency oscillation with an exponentially decaying envelope is observed. The corresponding 1 GHz PP traces are shown in Fig. 6.18. The optical pump and probe energies as well as the average beam powers are set as in Sec. 6.2.1. Fitting an exponentially decaying cosine function to the PP trace for the external field corresponding to $K = 32$ ($K - K_S = 16$) reveals, that the average frequency is considerably lower than the corresponding frequency. To investigate the underlying ES precession mode structure by performing a FFT, a two laser PP trace is taken for an external field sweep of $B_x = 2$ T (see Fig. 6.19(a)). Here, the external field is swept from $B_S = 1$ T to $B_x = 3$ T. The optical energy of the 1 GHz PRF laser is set to the pump position 5, while the optical energies of the pump and the probe pulses lie on the probe position as given in Fig. 6.15(a). The average powers right before the cryostat amount to $P_{Pu} = 7$ mW (power density $D_{Pu} = 350$ W/cm^2), $P_{Pr} = 160$ µW ($D_{Pr} = 10$ W/cm^2),

---

[27]The cryostat rotation is carried out as follows: At 0°, the reflection of the cryostat entrance window and the reflection of the sample surface fall in the same direction, along the incident pump beam. A ruler with a hole is placed 15 cm in front of the cryostat with the pump beam and the reflections going through the hole. Then, the sample is rotated such that the reflected sample spot is deviated by a given distance on the ruler. Finally, the cryostat, as a whole, is rotated until the reflected sample spot goes through the hole in the ruler again.
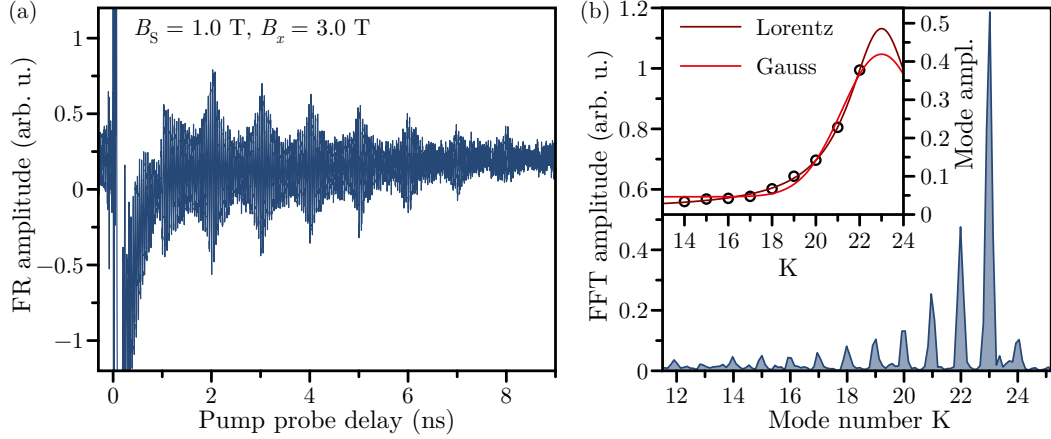
Figure 6.19: ES precession mode structure in a strongly dragged ENSS of an ensemble of QDs. (a) The PP trace in the two laser setup after sweeping the external field from $B_S = 1$ T to $B_x = 3$ T. A beating pattern each 1 ns forms. (b) FFT, plotted against the mode number K of the PP trace in (a), starting from 1 ns. Several precession modes, spaced by a frequency of 1 GHz, are present in the PP trace. The amplitude of each mode (except the final mode $K_x = 23$), as given by Lorentzian fits, is shown in the inset versus K. The mode amplitudes follow a Lorentzian rather than a Gaussian distribution, as evidenced by the two competing fits.

and $P_{GHz} = 11$ mW ($D_{GHz} = 560$ W/cm^2). The PP trace shows a beating pattern after the trion recombination starting from approximately 1 ns, with a constructive interference every 1 ns.

The decay of the single frequency oscillatory signal in between the constructive interferences resembles the ML presented in Sec. 2.5.1. The envelope of the constituent ES precession mode amplitudes is a symmetric Gaussian distribution, originating from the Gaussian distributed electron g-factor spread and the Gaussian distributed NSF [Gre06b]. To investigate similarities between the two phenomena, a FFT of the beating pattern is performed, and reveals a mode structure as in Sec. 6.2.1. The FFT spectrum is shown in Fig. 6.19(b). The starting mode $K_S = 8$, corresponding to an external field of $B_x = 1.03$ T, however, is not present. According to the model cited beforehand (see Sec. 6.2.1), the fixed optical detuning for the QDs does not allow a dragging of the OF to this magnitude. The lowest recognizable mode is mode $K = 14$. To determine the envelope of the mode structure, each peak in Fig. 6.19(b) is fitted by a Lorentzian distribution in order to extract each mode's amplitude.

A Lorentzian and a Gaussian distribution is fitted to the mode amplitudes, as shown in the inset in Fig. 6.19(b)[28]. The mode amplitude envelope is best described by a

---

[28]The modes $K_x = 23$ (the mode corresponding to the final field $B_x = 3$ T) and $K_x + 1$ are not considered, as they fall into the direct excitation of the 75.76 MHz PRF laser and their

Lorentzian distribution, as the Gaussian fit's residual sum of squares is an order of magnitude larger. One would expect a Gaussian distribution as the maximal OF is expected to depend on the Gaussian distributed optical detuning[29]. This requires clarification by further experiments.

6.4 Conclusions

The findings in this chapter highlight the potential of the 1 GHz PRF illumination on the ENSS of an inhomogeneous QD ensemble. The high PRF allows one to project the ESP in the ensemble onto a single precession mode. The NSP acts as OF on the ES and homogenizes a large proportion of the ESs Zeeman splittings. This enables the investigation of the inhomogeneity in the ensemble down to the NSF in a large transverse magnetic field range, with minimal influence of the inhomogeneous g factor. It is found that the NSF is reduced in illumination with 1 GHz PRF 5.8 times to $\delta B_{\mathrm{N}} = 1.2\,\mathrm{mT}$ or $\delta\omega_{\mathrm{N}} = 12\,\mathrm{MHz}$, compared to the NSF observed in barely excited (In,Ga)As/GaAs QDs [Zhu18b] and under pulsed illumination with a PRF of 75.76 MHz. Moreover, a positive optical pump probe detuning leads to the formation of precession frequency steps with plateaus of constant frequencies over the range of $B_0 = 128\,\mathrm{mT}$, which in turn indicates the build-up of a maximal OF of $B_0/2$.

Varying the transverse external field under 1 GHz pulsed excitation using a negative optical pump probe detuning, leads to an ES precession with several modes with frequencies equally spaced by the PRF. Above an external field of 0.6 T, the modes build up starting from the mode corresponding to the external field the illumination is applied first. This allows a dragging of the Zeeman splitting of up to 1.5 T (48 µeV). The appearance of the additional modes is traced to the optical pump trion detuning of individual QDs, which leads to individual maximal OFs. This mode pick-up is therefore considered an ensemble effect of the mode dragging for each single QD. By exploiting the long NS depolarization time, a polarization scheme is developed that allows one to add up the NSP from incremental external field sweeps to the maximal OF, as lines written in a typewriter add up to a page of text.

The findings place the pulsed excitation locking of an inhomogeneous QD ensemble on an equal footing with CPT in a tuned single QD [Hög12]. The PRF locking is also applicable to single QDs and provides an additional path of NS state preparation.

---

amplitude is thus increased.

[29] A hand-waving argument could be given by taking into account the repeated build-up of the OF in some QDs: The amplitude of each mode does not only consist of ESs in QDs with a maximal OF fitting to the external field difference $B_{\mathrm{N}} = B_x - KB_0$, but also of QDs with a larger maximal OF, whose OF broke down and builds up again.

Finally, the fast initialization of a considerable NSP in a transverse magnetic field paves the way for a detailed analysis of the NSP in optically-detected NMR setups. As an example, it could allow one to determine the isotope resolved NS coherence time for different degrees of the NSP. Moreover, the simultaneous existence of different magnitudes of the NSP in the ensemble enables to perform a detailed investigation of the NSP dependent polarization time $T_{1,\text{ne}}$ and depolarization time $T_{1,\text{n}}$ in a single experiment as function of the external field. Lastly, one could investigate the improved coherence of the ES as a function of the NSP and the external field B_x by making use of the ES ML [Gre06b]. This would be facilitated by the synchronization of the two lasers, as the ENSS would be trained such, that both the NSP and ESP fit to the low PRF originally thereby preventing an additional loss of ESP when measuring with the low PRF laser only.

Appendix A. Implementation of the Broadband RF Application

Two different broadband RF application patterns are programmed in order to take spectra of contributing NSs with different widths[1]. The application of resonant RF with random phase or longer than the coherent Rabi oscillations leads to the equalization of the level population [Che17]. Therefore, two different RF protocols are used as shown in Fig. A.1(a): the normal mode and the inverse mode. In normal mode, a sharp frequency distribution with a full width w around an isotopes NS central transition in a given external field B_x is employed in order to annihilate the contribution of these NSs. In inverse mode, the frequency distribution is set to zero only in the desired width around the isotopes NS central transition. This nullifies the contribution of all other transitions and isotopes [Che12]. Both modes can be set up to determine the contribution of two or more isotopes or transitions simultaneously by defining two or more frequency ranges.

To realize these schemes in the experiment, the spectra need to be transformed into time traces which are applied to the sample as RF fields. This conversion is implemented in National Instruments LABVIEW following the sketch presented in Fig. A.1(b). Each data point of the chosen frequency distribution is given a random phase and converted to a complex number. The random phase leads to a non-coherent time trace and the broadband RF application is therefore only used to record the NMR spectra. An inverted Fourier transform is performed on the set of complex numbers. The resulting real part (see Fig. A.1(c)) is then taken as the voltage (time) trace saved in the memory of the arbitrary function generator. The saved trace is played and applied to the sample via the RF amplifier repeatedly (see Fig. A.1(d)).

Note that two scaling parameters are involved which need to be defined when calculating the voltage waveform and set at the function generator. (i) The amplitude of the RF signal after the amplifier should not lead to reflections on the cable back into the amplifier such that it is overloaded. To be on the safe side, one takes it already into account when setting up the frequency distribution in the beginning. The integral over the whole frequency range should be equal to a known maximum in order to set the maximal level of the output voltage after the inverse Fourier

---

[1]The implementation shown here has been conceived by DR. TOMASZ KAZIMIERCZUK, now at University of Warsaw.
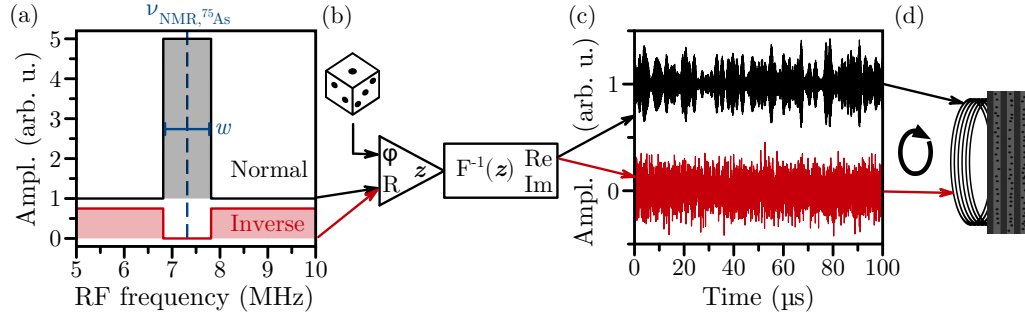
Figure A.1: Implementation of broadband RF field application using National Instruments LABVIEW and an arbitrary function generator. (a) A sharp amplitude distribution around the central frequency with the desired width is generated (shown for ^{75}As, $\nu_{\mathrm{NMR},^{75}\mathrm{As}} = 7.315\,\mathrm{MHz}$ [Hay12] with a full width of $w = 0.5\,\mathrm{MHz}$). For the normal mode, only the amplitude inside the chosen width differs from zero while the opposite distribution is generated for the inverse mode. The integral over both curves should be equal in order to ensure the maximal (equal) output voltage by the function generator. (b) Each data point from (a) is given a random phase and an inverted Fourier transform is executed on the set of complex numbers. (c) The real part of the Fourier transformed frequency distribution is stored in the waveform memory of the arbitrary function generator as voltage (time) trace. (d) The saved waveform is played repeatedly by the function generator and transmitted to the coil via the RF amplifier (not shown).

transform[2]. This leads to the scaling of the maximal amplitude between the normal and the inverse mode depicted in Fig. A.1(a) but also to an amplitude scaling between different widths w. The amplitude scaling can be tuned as well by setting the output power of the arbitrary function generator. (ii) The arbitrary function generator only has a limited number of available data points for one waveform. The time resolution of the waveform is therefore depending on the frequency with which the waveform is repeated (for cw or long pulse application). This is now programmed to $1\,\mathrm{kHz}$ and should be taken into account when altering the LABVIEW implementation as changing this frequency also scales the applied frequency. Lastly, it is necessary to set the repetition frequency $1\,\mathrm{kHz}$ explicitly at the function generator.

---

[2] The amplifier shuts itself of if it is overloaded but keep in mind that this might occur unnoticed. Keep moreover in mind that the reflectivity of the cable, resistance, and coil system depends on the RF frequency.

Abbreviations

AOM Acusto-optic modulator
As Arsenic

CB Conduction band
CCD Charge-coupled device
Cd Cadmium
CdTe Cadmium telluride
CPT Coherent population trapping
cw continuous wave

DL Mechanical delay line
DNP Dynamical nuclear polarization

ENSS Electron-nuclear spin system
EOM Electro-optic modulator
EPP Extended pump probe
ES Electron spin
ESP Electron spin polarization

fcc face-centered cubic
FFT Fast Fourier transform
FE Faraday ellipticity
FR Faraday rotation
FWHM Full width at half maximum

Ga Gallium
GaAs Gallium arsenide

HH Heavy hole
HWHM Half width at half maximum

In Indium
InAs Indium arsenide
IR infra-red

LH Light hole
LI Lock-in amplifier

MBE Molecular beam epitaxy

Mg Magnesium
ML Mode locking

NIFF Nuclei-induced frequency focusing
NMR Nuclear magnetic resonance
NS Nuclear spin
NSF Nuclear spin fluctuation
NSP Nuclear spin polarization
NSS Nuclear spin system

OF Overhauser field

PEM Photo-elastic modulator
PL Photoluminescence spectrum
PP Pump probe
PRC Polarization recovery curve
PRF Laser pulse repetition frequency
PRP Laser pulse repetition period
PSC Phase synchronization condition

QD Quantum dot
QKD Quantum key distribution
QW Quantum well

RF Radio frequency
RSA Resonant spin amplification

Si Silicon
SO Spin orbit
STM Scanning tunneling microscope

Te Tellurium
TRFR Time resolved Faraday rotation

VB Valence band
VTI Variable Temperature Insert

Symbols

a Lattice parameter of a cubic Bravais lattice

A Hyperfine constant of a nucleus which is specific for each isotope and depends on the overlap of the wave function ξ of a charge carrier with the nucleus

a_{nat} Natural abundance of a specific isotope

$\mathbf{B}$ External magnetic field vector

B_{ext} External magnetic field magnitude applied in any direction

B_x External magnetic field applied in x direction, transversal to the light propagation (Voigt geometry)

B_z External magnetic field applied in z direction, along the light propagation (Faraday geometry)

B_{RF} Radio frequency magnetic field for nuclear magnetic resonance experiments

B_{N} Overhauser field (OF) exerted by the nuclear spins (NSs) on the electron spin (ES) by hyperfine interaction

$B_{\mathrm{N,max}}$ Maximal Overhauser field (OF) exerted by the fully polarized nuclear spins (NSs) on the electron spin (ES) by hyperfine interaction

B_{K} Knight field exerted by the electron spin (ES) on the nuclear spin (NS)

B_0 Magnetic field corresponding to an electron spin (ES) precession period equal to the laser pulse repetition period (PRP); magnetic field separation between two ES precession modes

B_{S} External field at the start of a field sweep

β_{N} Diminishing constant of an electron spin (ES) precession mode amplitude with increasing varied external field B_x magnitude

D_{GHz} Average power density of the $1\,\mathrm{GHz}$ pump beam directly in front of the cryostat, given in relation to the FWHM spot size on the sample

D_{Pr}	Average power density of the probe beam directly in front of the cryostat, given in relation to the FWHM spot size on the sample
D_{Pu}	Average power density of the pump beam directly in front of the cryostat, given in relation to the FWHM spot size on the sample
δB	Full width at half maximum (FWHM) of the central minimum in a polarization recovery curve (PRC); for an interpolated zero laser excitation power P_{Pu}, it equals two times the nuclear spin fluctuation (NSF) δB_{N}
δB_{N}	Half width at half maximum (HWHM) of the nuclear spin fluctuation (NSF) acting on the electron spin (ES) by hyperfine interaction
ΔB_{N}	Change of the Overhauser field (OF) after the application of radio frequency (RF) fields
$\Delta\phi$	Phase shift of the electron spin polarization (ESP) precession due to the change in Overhauser field (OF) ΔB_{N} after the application of radio frequency (RF) fields
Δg_{e}	Spread of the electron g factor g_{e}
$\delta\omega_{\mathrm{e}}$	Knight field fluctuations acting on the nuclear spin (NS) caused by the arbitrarily oriented and precessing electron spin (ES)
$\Delta\omega_{g_{\mathrm{e}}}$	Spread of the electron spin (ES) precession frequency ω caused by the g-factor spread Δg_{e}
$\delta\omega_{\mathrm{N}}$	Spread of the electron spin (ES) precession frequency ω caused by the nuclear spin fluctuation (NSF)
$\Delta E_{\mathrm{Z,e}}$	Electron Zeeman splitting of states with different total angular momentum magnitudes J by interaction of the magnetic moment with an external field
$\Delta E_{\mathrm{Z,n}}$	Nuclear Zeeman splitting of states with different total angular momentum magnitudes J by interaction of the magnetic moment with an external field
$\Delta_{\mathrm{HH\text{-}LH}}$	Heavy hole (HH)-light hole (LH) splitting in the valence band (VB); vanishes in the center of the Brillouin zone ($\mathbf{k}=0$) for bulk zinc blende crystals but split in strained nanostructures
Δ_{SO}	Splitting of the bands with different total angular momentum magnitudes J in the valence band (VB)
E_{F}	Fermi energy up to which electrons occupy the bands in a crystal
E_{g}	Band gap energy from the highest point in the valence band (VB) to the lowest point of the conduction band (CB); to excite an exciton, the band gap energy reduced by the exciton binding energy is required

Symbols

E_{Tr}	Central optical energy of the trion excitation
E_{GHz}	Central optical energy of the 1 GHz pump laser pulses
E_{Pr}	Central optical energy of the probe laser pulses
E_{Pu}	Central optical energy of the pump laser pulses
E_{Drag}	Dragging energy as change of the trion Zeeman energy when slowly shifting the optical excitation energy; used in coherent population trapping (CPT) experiments to quantify the additional nuclear spin polarization (NSP) which compensates the spectral shift
F	The filling factor describes the relative occupation time of a nucleus location by a charge carrier
f_{N}	Leakage factor which quantifies the steady state nuclear spin polarization (NSP) by comparing the concurring nuclear spin (NS) (de)polarization rate by electrons $1/T_{1,\mathrm{ne}}$ and the NS lattice relaxation rate $1/T_{1,\mathrm{n}}$
θ_{F}	Faraday rotation (FR) angle of the probe beam after transmission through an electron spin (ES) polarized sample
Γ_{Bx}	Sweeping rate of the external field B_x
g_{e}	Electron g factor in z direction transversal to the applied external field; depends negatively linear on the trion excitation energy E_{Tr}
g_{N}	Nuclear g factor
γ	Gyromagnetic ratio which relates an angular momentum (nuclear spin (NS)) of a nucleus to its magnetic moment
$\hbar$	Reduced Planck constant which relates the energy of a photon or transition to its (angular) frequency
H_{Z}	Hamiltonian describing the Zeeman interaction (energy) between a magnetic moment and an external magnetic field
$\mathbf{I}$	Nuclear spin (NS)
$\mathbf{J}$	Total angular momentum of a given state or band; the total angular momentum equals the vectorial sum of the orbital momentum and the spin
J	Magnitude of the total angular momentum of a given state or band; the magnitude of the total angular momentum equals the sum of the magnitude of the orbital momentum and the magnitude of the spin
J_z	Component of the total angular momentum $\mathbf{J}$ of an electron state or band along the light propagation; resident electrons are excited into the

trion state following the selection rules defined by this component of the total angular momentum

k   Wave vector in a crystal; directly proportional to the crystal momentum

k_B Boltzmann constant which links the temperature of a free particle to its thermal energy

K Electron spin (ES) precession mode number as multiplier to the laser pulse repetition frequency (PRF) ω_R; integer values fulfill the phase synchronization condition (PSC)

K_S Electron spin (ES) precession mode which corresponds to the external field B_S at the start of a field sweep

K_x Electron spin (ES) precession mode which corresponds to the current external field B_x

L   Orbital angular momentum of a given state or band

m^* Reduced mass of a charge carrier in an energy band; the reduced mass depends on the band curvature

m_e Electron mass

μ_B Bohr magneton which relates an electron angular momentum to its magnetic moment

μ_N Nuclear magneton which relates a nuclear angular momentum to its magnetic moment

n_e Electron density in a semiconductor quantum well (QW)

$\nu_{Mod,Pr}$ Modulation frequency of the probe beam amplitude modulation

$\nu_{Mod,Pu}$ Modulation frequency of the pump and 1 GHz pump beam modulation; the modulation is between σ^+ and σ^- within one period

$\nu_{NMR,^{75}As}$ Nuclear magnetic resonance (NMR) frequency for the central ^{75}As (arsenic-75) nuclear spin (NS) transition

$\nu_{NMR,^{111}Cd}$ Nuclear magnetic resonance (NMR) frequency for the ^{111}Cd (cadmium-111) nuclear spin (NS) transition

$\nu_{NMR,^{113}Cd}$ Nuclear magnetic resonance (NMR) frequency for the ^{113}Cd (cadmium-113) nuclear spin (NS) transition

$\nu_{NMR,^{125}Te}$ Nuclear magnetic resonance (NMR) frequency for the ^{125}Te (tellurium-125) nuclear spin (NS) transition

Symbols

P_{GHz}	Average power of the 1 GHz pump beam directly in front of the cryostat; the transmission through the entrance windows of the cryostat reduces the average power by approximately 20 %
P_{Pr}	Average power of the probe beam directly in front of the cryostat; the transmission through the entrance windows of the cryostat reduces the average power by approximately 20 %
P_{Pu}	Average power of the pump beam directly in front of the cryostat; the transmission through the entrance windows of the cryostat reduces the average power by approximately 20 %
$\mathcal{S}(\mathbf{r})$	Bloch amplitude, amplitude of the electron wave function inside a primitive cell
$\mathbf{S}$	Electron spin (ES)
S_x	Component (projection) of the electron spin polarization (ESP) along the external field B_x in Voigt geometry
S_z	Component (projection) of the electron spin polarization (ESP) along the light propagation and along the external field B_z in Faraday geometry; this component is measured by Faraday rotation (FR) or Faraday ellipticity (FE)
σ^+, σ^-	Circular polarization of a photon or laser beam
$T_{2,\mathrm{e}}^*$	Electron spin polarization (ESP) dephasing time which quantifies the time until which an ensemble of electron spins (ESs) interferes constructively; also gives the rise time of the ES mode locking (ML) amplitude
$T_{2,\mathrm{f}}^*$	Electron spin polarization (ESP) dephasing time contribution resulting from the hyperfine interaction with fluctuating nuclear spins (NSs)
$T_{2,\mathrm{g}}^*$	Electron spin polarization (ESP) dephasing time contribution resulting from the *g*-factor spread in the individual quantum dots (QDs)
$T_{2,\mathrm{n}}^*$	Nuclear spin polarization (NSP) dephasing time which quantifies the time until which an ensemble of nuclear spins (NSs) interferes constructively
$T_{2,\mathrm{e}}$	Electron spin (ES) coherence time (transversal ES relaxation time) until which an ES precesses about an external field with a well-defined phase
$T_{2,\mathrm{n}}$	Nuclear spin (NS) coherence time (transversal NS relaxation time) until which a NS precesses about an external field with a well-defined phase
$T_{1,\mathrm{e}}$	Longitudinal electron spin (ES) relaxation time which gives the timescale up to which the electron spin polarization (ESP) (along an external field) is out of thermal equilibrium

$T_{1,\mathrm{n}}$ — Longitudinal nuclear spin (NS) relaxation time which gives the timescale up to which the nuclear spin polarization (NSP) is out of thermal equilibrium with the crystal lattice; in other publications referred to as T_{d}

$T_{1,\mathrm{ne}}$ — Longitudinal nuclear spin (NS) (de)polarization time caused by the interaction with electron spins (ESs); in other publications referred to as $T_{1\mathrm{e}}$

T_{R} — Laser pulse repetition period (PRP) as time between two pump pulses, either multiples of $13.2\,\mathrm{ns}$ or $1\,\mathrm{ns}$ throughout this work

Δt — Time delay between the (last) pump and the next probe pulse

τ_{π} — Radio frequency (RF) pulse with a frequency resonant to a given nuclear spin (NS) Zeeman transition which tilts the nuclear spin polarization (NSP) by an angle $\vartheta = \pi$

$\tau_{\pi/2}$ — Radio frequency (RF) pulse with a frequency resonant to a given nuclear spin (NS) Zeeman transition which tilts the nuclear spin polarization (NSP) by an angle $\vartheta = \pi/2$

τ_{12} — Time between two $\tau_{\pi/2}$ nuclear magnetic resonance (NMR) pulses for the application of Ramsey fringes

τ_{13} — Time between two $\tau_{\pi/2}$ nuclear magnetic resonance (NMR) pulses including a τ_{π} pulse in the middle between them for the measurement of Hahn echoes

τ_{Tr} — Trion recombination time

ϑ — Tilt angle of the nuclear spin (NS) caused by the application of (resonant) radio frequency (RF) fields; an angle of 2π corresponds to a full Rabi oscillation period

Θ — Pulse area by which a Rabi oscillation is driven and is a product of the power and application time; applies both to the coherent excitation of a trion by a pump pulse and to the coherent tilting of the nuclear spin polarization (NSP) by an radio frequency (RF) pulse

v_0 — Volume of the primitive cell of a semiconductor crystal

w — Full width of the radio frequency (RF) spectrum applied to record the nuclear magnetic resonance (NMR) spectrum of contributing nuclei

ω — Total electron spin (ES) precession frequency which includes all possible contributions (B_{ext} and B_{N})

ω_{L} — Larmor frequency as electron spin (ES) precession frequency caused by the interaction of the electron or nucleus magnetic moment with the external field (Zeeman interaction with B_{ext})

Symbols

ω_N	Electron spin (ES) precession frequency due to the Overhauser field (OF) exerted by the nuclear spins (NSs) on the ES by hyperfine interaction
ω_R	Laser pulse repetition frequency (PRF) which defines the resonant total electron spin (ES) precession frequencies ω and the corresponding (effective) magnetic field B_0
Ω_Rabi	Rabi frequency which describes the driven, coherent oscillatory transfer between two states; the application of (resonant) radio frequency (RF) fields leads to a tilting of the nuclear spin polarization (NSP) transversal to the external field
X^0	Exciton as electron-hole pair bound by Coulomb interaction which decreases its formation energy by the exciton binding energy from the band gap energy E_g
X^-	Negative trion as electron-hole-electron complex bound by Coulomb interaction which decreases its formation energy even further than the exciton binding energy from the band gap energy E_g
$\lvert\uparrow\rangle, \lvert\downarrow\rangle$	Spin eigenstates in the basis defined by an external field in x direction
$\lvert\rightarrow\rangle, \lvert\leftarrow\rangle$	Spin states as a coherent superposition of the $\lvert\uparrow\rangle, \lvert\downarrow\rangle$ eigenstates; these composed spin states point along the light propagation axis z and can serve as eigenstates for the excitation with circularly polarized light
$\xi(\mathbf{r})$	Wave function envelope of an electron
$\lvert\Psi\rangle$	Quantum mechanical state in a Bloch sphere defined by the spin eigenstates $\lvert\uparrow\rangle, \lvert\downarrow\rangle$
$\lvert\psi\rangle$	Quantum mechanical state in a Bloch sphere with the $\lvert\leftarrow\rangle$ and X^- eigenstates

Bibliography

[Abr83a]   A. Abragam, "Dipolar line width in a rigid lattice," in *Principles of nuclear magnetism* (Clarendon Press, Oxford, 1983) Chap. 4, pp. 97–132.

[Abr83b]   A. Abragam, "Electron-nucleus interactions," in *Principles of nuclear magnetism* (Clarendon Press, Oxford, 1983) Chap. 6, pp. 159–215.

[Abr83c]   A. Abragam, "Motion of free spins," in *Principles of nuclear magnetism* (Clarendon Press, Oxford, 1983) Chap. 2, pp. 19–38.

[Abr83d]   A. Abragam, "Spin temperature," in *Principles of nuclear magnetism* (Clarendon Press, Oxford, 1983) Chap. 5, pp. 133–158.

[Abr83e]   A. Abragam, "Thermal relaxation and dynamic polarization in solids," in *Principles of nuclear magnetism* (Clarendon Press, Oxford, 1983) Chap. 9, pp. 354–423.

[Aru19]   F. Arute, K. Arya, R. Babbush, D. Bacon, J. C. Bardin, R. Barends, R. Biswas, S. Boixo, F. G. S. L. Brandao, D. A. Buell, B. Burkett, Y. Chen, et al., "Quantum supremacy using a programmable superconducting processor," Nature **574**, 505–510 (2019).

[Ast08]   G. V. Astakhov, M. M. Glazov, D. R. Yakovlev, E. A. Zhukov, W. Ossau, L. W. Molenkamp, and M. Bayer, "Time-resolved and continuous-wave optical spin pumping of semiconductor quantum wells," Semicond. Sci. Technol. **23**, 114001 (2008).

[Ata06]   M. Atatüre, J. Dreiser, A. Badolato, A. Hoegele, K. Karrai, and A. Imamoglu, "Quantum-dot spin-state preparation with near-unity fidelity," Science **312**, 551 (2006).

[AZ11]   R. Augulis and D. Zigmantas, "Two-dimensional electronic spectroscopy with double modulation lock-in detection: Enhancement of sensitivity and noise resistance," Opt. Express **19**, 13126 (2011).

[BAP75]   G. L. Bir, A. G. Aronov, and G. E. Pikus, "Spin relaxation of electrons due to scattering by holes," J. Exp. Theor. Phys. **42**, 705–712 (1975).

[Bau94]   J. J. Baumberg, S. A. Crooker, D. D. Awschalom, N. Samarth, H. Luo, and J. K. Furdyna, "Ultrafast Faraday spectroscopy in magnetic semiconductor quantum structures," Phys. Rev. B **50**, 7689 (1994).

[Bay02]   M. Bayer, G. Ortner, O. Stern, A. Kuther, A. A. Gorbunov, A. Forchel, P. Hawrylak, S. Fafard, K. Hinzer, T. L. Reinecke, S. N. Walck, J. P. Reithmaier, et al., "Fine structure of neutral and charged excitons in self-assembled In(Ga)As/(Al)GaAs quantum dots," Phys. Rev. B **65**, 195315 (2002).

[Bay95]   M. Bayer, A. Schmidt, A. Forchel, F. Faller, T. L. Reinecke, P. A. Knipp, A. A. Dremin, and V. D. Kulakovskii, "Electron-hole transitions between states with nonzero angular momenta in the magnetoluminescence of quantum dots," Phys. Rev. Lett. **74**, 3439 (1995).

[BB84]   C. H. Bennett and G. Brassard, "Quantum cryptography: Public key distribution and coin tossing," in Proc. IEEE Int. conf. computers, Systems and signal processing, Bangalore, India (Jan. 1, 1984), p. 175.

[Bec15]   A. Bechtold, D. Rauch, F. Li, T. Simmet, P.-L. Ardelt, A. Regler, K. Müller, N. A. Sinitsyn, and J. J. Finley, "Three-stage decoherence dynamics of an electron spin qubit in an optically active quantum dot," Nat. Phys. **11**, 1005 (2015).

[Bel16]   V. V. Belykh, E. Evers, D. R. Yakovlev, F. Fobbe, A. Greilich, and M. Bayer, "Extended pump-probe Faraday rotation spectroscopy of the submicrosecond electron spin dynamics in n-type GaAs," Phys. Rev. B **94**, 241202 (2016).

[Ber08]   J. Berezovsky, M. H. Mikkelsen, N. G. Stoltz, L. A. Coldren, and D. D. Awschalom, "Picosecond coherent optical manipulation of a single electron spin in a quantum dot," Science **320**, 349–352 (2008).

[BES74]   V. L. Berkovits, A. I. Ekimov, and V. I. Safarov, "Optical orientation in a system of electrons and lattice nuclei in semiconductors. Experiment," J. Exp. Theor. Phys. **38**, 169–176 (1974).

[BGK08]   A. S. Bracker, D. Gammon, and V. L. Korenev, "Fine structure and optical pumping of spins in individual semiconductor quantum dots," Semicond. Sci. Technol. **23**, 114004 (2008).

[Blo46]   F. Bloch, "Nuclear induction," Phys. Rev. **70**, 460–474 (1946).

[Blo54]   N. Bloembergen, "Nuclear magnetic relaxation in semiconductors," Physica **20**, 1130–1133 (1954).

[Blü19]   B. Blümich, "Hyperpolarization," in *Essential NMR: For scientists and engineers*, 2nd ed. (Springer International Publishing, Cham, 2019) Chap. 6, pp. 143–158.

[Bri98]   H.-J. Briegel, W. Dür, J. I. Cirac, and P. Zoller, "Quantum repeaters: The role of imperfect local operations in quantum communication," Phys. Rev. Lett. **81**, 5932–5935 (1998).

[BS40]   F. Bloch and A. Siegert, "Magnetic resonance for nonrotating fields," Phys. Rev. **57**, 522 (1940).

[BS66]   A. D. Buckingham and P. J. Stephens, "Magnetic optical activity," Annu. Rev. Phys. Chem. **17**, 399–432 (1966).

[BUA17]   W. Beugeling, G. S. Uhrig, and F. B. Anders, "Influence of the nuclear Zeeman effect on mode locking in pulsed semiconductor quantum dots," Phys. Rev. B **96**, 115303 (2017).

[Buh95]   H. Buhmann, L. Mansouri, J. Wang, P. H. Beton, N. Mori, L. Eaves, M. Henini, and M. Potemski, "Electron-concentration-dependent quantum-well luminescence: Evidence for a negatively charged exciton," Phys. Rev. B **51**, 7969–7972 (1995).

[Car09]   S. G. Carter, A. Shabaev, S. E. Economou, T. A. Kennedy, A. S. Bracker, and T. L. Reinecke, "Directing nuclear spin flips in InAs quantum dots using detuned optical pulse trains," Phys. Rev. Lett. **102**, 167403 (2009).

[Cas15]   B. Casabone, K. Friebe, B. Brandstätter, K. Schüppert, R. Blatt, and T. E. Northup, "Enhanced quantum interface with collective ion-cavity coupling," Phys. Rev. Lett. **114**, 023602 (2015).

[Che12]   E. A. Chekhovich, K. V. Kavokin, J. Puebla, A. B. Krysa, M. Hopkinson, A. D. Andreev, A. M. Sanchez, R. Beanland, M. S. Skolnick, and A. I. Tartakovskii, "Structural analysis of strained quantum dots using nuclear magnetic resonance," Nat. Nanotechnol. **7**, 646 (2012).

[Che15]   E. Chekhovich, M. Hopkinson, M. Skolnick, and A. Tartakovskii, "Suppression of nuclear spin bath fluctuations in self-assembled quantum dots induced by inhomogeneous strain," Nat. Commun. **6**, 6348 (2015).

[Che17]   E. A. Chekhovich, A. Ulhaq, E. Zallo, F. Ding, O. G. Schmidt, and M. S. Skolnick, "Measurement of the spin temperature of optically cooled nuclei and GaAs hyperfine constants in GaAs/AlGaAs quantum dots," Nat. Mater. **16**, 982 (2017).

[DDP76]   V. D. Dymnikov, M. I. Dyakonov, and N. I. Perel, "Anisotropy of momentum distribution of photoexcited electrons and polarization of hot luminescence in semiconductors," J. Exp. Theor. Phys. **44**, 1252–1256 (1976).

[DK07]   R. I. Dzhioev and V. L. Korenev, "Stabilization of the electron-nuclear spin orientation in quantum dots by the nuclear quadrupole interaction," Phys. Rev. Lett. **99**, 037401 (2007).

[DM10]   L.-M. Duan and C. Monroe, "Colloquium: Quantum networks with trapped ions," Rev. Mod. Phys. **82**, 1209–1224 (2010).

[DN08]   J. Danon and Y. V. Nazarov, "Nuclear tuning and detuning of the electron spin resonance in a quantum dot: Theoretical consideration," Phys. Rev. Lett. **100**, 056603 (2008).

[DP71]   M. I. Dyakonov and V. I. Perel, "Spin orientation of electrons associated with the interband absorption of light in semiconductors," J. Exp. Theor. Phys. **33**, 1053–1059 (1971).

[DP84]   M. I. Dyakonov and V. I. Perel, "Theory of optical spin orientation of electrons and nuclei in semiconductors," in *Optical orientation*, Vol. 8, edited by F. Meier and B. P. Zakharchenya, Modern Problems in Condensed Matter Sciences (North-Holland, Amsterdam, 1984) Chap. 2, pp. 11–71.

[Dua01]   L.-M. Duan, M. D. Lukin, J. I. Cirac, and P. Zoller, "Long-distance quantum communication with atomic ensembles and linear optics," Nature **414**, 413–418 (2001).

[Dya17]   M. I. Dyakonov, "Basics of semiconductor and spin physics," in *Spin physics in semiconductors*, edited by M. I. Dyakonov, 2nd ed. (Springer International Publishing, Cham, 2017) Chap. 1, pp. 1–37.

[Ebl06]   B. Eble, O. Krebs, A. Lemaître, K. Kowalik, A. Kudelski, P. Voisin, B. Urbaszek, X. Marie, and T. Amand, "Dynamic nuclear polarization of a single charge-tunable InAs/GaAs quantum dot," Phys. Rev. B **74**, 081306 (2006).

[Eis08]   H. Eisele, A. Lenz, R. Heitz, R. Timm, M. Dähne, Y. Temko, T. Suzuki, and K. Jacobi, "Change of InAs/GaAs quantum dot shape and composition during capping," J. Appl. Phys. **104**, 124301 (2008).

[Eke91]   A. K. Ekert, "Quantum cryptography based on Bell's theorem," Phys. Rev. Lett. **67**, 661–663 (1991).

[Ell54]   R. J. Elliott, "Theory of the effect of spin-orbit coupling on magnetic resonance in some semiconductors," Phys. Rev. **96**, 266–279 (1954).

[Éth17]   G. Éthier-Majcher, D. Gangloff, R. Stockill, E. Clarke, M. Hugues, C. Le Gall, and M. Atatüre, "Improving a solid-state qubit through an engineered mesoscopic environment," Phys. Rev. Lett. **119**, 130503 (2017).

[Eve18]   E. Evers, V. V. Belykh, N. E. Kopteva, I. A. Yugova, A. Greilich, D. R. Yakovlev, D. Reuter, A. D. Wieck, and M. Bayer, "Decay and revival of electron spin polarization in an ensemble of (In,Ga)As quantum dots," Phys. Rev. B **98**, 075309 (2018).

[Eve19]   E. Evers, T. Kazimierczuk, F. Mertens, D. R. Yakovlev, G. Karczewski, T. Wojtowicz, J. Kossut, M. Bayer, and A. Greilich, "Nuclear spin dynamics influenced and detected by electron spin polarization in CdTe/(Cd,Mg)Te quantum wells," Phys. Rev. B **99**, 045303 (2019).

[Eve21a]   E. Evers, N. E. Kopteva, I. A. Yugova, D. R. Yakovlev, M. Bayer, and A. Greilich, "Shielding of external magnetic field by dynamic nuclear polarization in (In,Ga)As quantum dots," Phys. Rev. B **104**, 075302 (2021).

[Eve21b]   E. Evers, N. E. Kopteva, I. A. Yugova, D. R. Yakovlev, D. Reuter, A. D. Wieck, M. Bayer, and A. Greilich, "Suppression of nuclear spin fluctuations in an InGaAs quantum dot ensemble by GHz-pulsed optical excitation," npj Quantum Inf. **7**, 60 (2021).

[Far46]   M. Faraday, "On the magnetization of light and the illumination of magnetic lines of force," Philos. Trans. Roy. Soc. London **136**, 1–20 (1846).

[Fli90]   G. P. Flinn, R. T. Harley, M. J. Snelling, A. C. Tropper, and T. M. Kerr, "Optically detected nuclear magnetic resonance of nuclei within a quantum well," Semicond. Sci. Technol. **5**, 533–537 (1990).

[FLS17]   B. Friess, Y. Q. Li, and J. H. Smet, "Electron-nuclear spin interactions in the quantum hall regime," in *Spin physics in semiconductors*, edited by M. I. Dyakonov, 2nd ed. (Springer International Publishing, Cham, 2017), pp. 431–475.

[FM84]   V. G. Fleisher and I. A. Merkulov, "Optical orientation of the coupled electron–nuclear spin system of a semiconductor," in *Optical orientation*, Vol. 8, edited by F. Meier and B. P. Zakharchenya, Modern Problems in Condensed Matter Sciences (North-Holland, Amsterdam, 1984) Chap. 5, pp. 173–258.

[Gam01]   D. Gammon, A. L. Efros, T. A. Kennedy, M. Rosen, D. S. Katzer, D. Park, S. W. Brown, V. L. Korenev, and I. A. Merkulov, "Electron and nuclear spin interactions in the optical spectra of single GaAs quantum dots," Phys. Rev. Lett. **86**, 5176–5179 (2001).

[Gam97]   D. Gammon, S. W. Brown, E. S. Snow, T. A. Kennedy, D. S. Katzer, and D. Park, "Nuclear spectroscopy in single quantum dots: Nanoscopic Raman scattering and nuclear magnetic resonance," Science **277**, 85–88 (1997).

[Gan19]   D. A. Gangloff, G. Éthier-Majcher, C. Lang, E. V. Denning, J. H. Bodey, D. M. Jackson, E. Clarke, M. Hugues, C. Le Gall, and M. Atatüre, "Quantum interface of an electron and a nuclear ensemble," Science **364**, 62–66 (2019).

[Gao21]   Q. Gao, G. O. Jones, M. Motta, M. Sugawara, H. C. Watanabe, T. Kobayashi, E. Watanabe, Y. Ohnishi, H. Nakamura, and N. Yamamoto, "Applications of quantum computing for investigations of electronic transitions in phenylsulfonyl-carbazole TADF emitters," npj Comput. Mater. **7**, 70 (2021).

[GKB10a]   O. Gywat, H. J. Krenner, and J. Berezovsky, "Introduction," in *Spins in optically active quantum dots* (John Wiley & Sons, Ltd, 2010) Chap. 1, pp. 1–14.

[GKB10b]   O. Gywat, H. J. Krenner, and J. Berezovsky, "Theory of confined states in quantum dots," in *Spins in optically active quantum dots* (John Wiley & Sons, Ltd, 2010) Chap. 3, pp. 39–66.

[Gla10]   M. M. Glazov, I. A. Yugova, S. Spatzek, A. Schwan, S. Varwig, D. R. Yakovlev, D. Reuter, A. D. Wieck, and M. Bayer, "Effect of pump-probe detuning on the Faraday rotation and ellipticity signals of mode-locked spins in (In,Ga)As/GaAs quantum dots," Phys. Rev. B **82**, 155325 (2010).

[Gla18a]   M. M. Glazov, "Electron spin relaxation beyond the hyperfine interaction," in *Electron & nuclear spin dynamics in semiconductor nanostructures* (Oxford University Press, Oxford, 2018) Chap. 8, pp. 165–187.

[Gla18b]   M. M. Glazov, "Hyperfine interaction of electron and nuclear spins," in *Electron & nuclear spin dynamics in semiconductor nanostructures* (Oxford University Press, Oxford, 2018) Chap. 4, pp. 61–81.

[Gla18c]   M. M. Glazov, "Spin systems in semiconductor nanostructures," in *Electron & nuclear spin dynamics in semiconductor nanostructures* (Oxford University Press, Oxford, 2018) Chap. 2, pp. 5–36.

[Got98]   H. Gotoh, H. Ando, H. Kamada, A. Chavez-Pirson, and J. Temmyo, "Spin relaxation of excitons in zero-dimensional InGaAs quantum disks," Appl. Phys. Lett. **72**, 1341–1343 (1998).

[Gra09]   S. Gražulis, D. Chateigner, R. T. Downs, A. F. T. Yokochi, M. Quirós, L. Lutterotti, E. Manakova, J. Butkus, P. Moeck, and A. Le Bail, "Crystallography Open Database – an open-access collection of crystal structures," J. Appl. Crystallogr. **42**, 726–729 (2009).

[Gra16]   L. B. Gravert, P. Lorenz, C. Nase, J. Stolze, and G. S. Uhrig, "Increased coherence time in narrowed bath states in quantum dots," Phys. Rev. B **94**, 094416 (2016).

[Gre06a]   A. Greilich, R. Oulton, E. A. Zhukov, I. A. Yugova, D. R. Yakovlev, M. Bayer, A. Shabaev, A. L. Efros, I. A. Merkulov, V. Stavarache, D. Reuter, and A. Wieck, "Optical control of spin coherence in singly charged (In,Ga)As/GaAs quantum dots," Phys. Rev. Lett. **96**, 227401 (2006).

[Gre06b]   A. Greilich, M. Schwab, T. Berstermann, T. Auer, R. Oulton, D. R. Yakovlev, M. Bayer, V. Stavarache, D. Reuter, and A. Wieck, "Tailored quantum dots for entangled photon pair creation," Phys. Rev. B **73**, 045323 (2006).

[Gre06c]   A. Greilich, D. R. Yakovlev, A. Shabaev, A. L. Efros, I. A. Yugova, R. Oulton, V. Stavarache, D. Reuter, A. Wieck, and M. Bayer, "Mode locking of electron spin coherences in singly charged quantum dots," Science **313**, 341 (2006).

[Gre07]   A. Greilich, A. Shabaev, D. R. Yakovlev, A. L. Efros, I. A. Yugova, D. Reuter, A. D. Wieck, and M. Bayer, "Nuclei-induced frequency focusing of electron spin coherence," Science **317**, 1896 (2007).

[Gre09]   A. Greilich, S. Spatzek, I. A. Yugova, I. A. Akimov, D. R. Yakovlev, A. L. Efros, D. Reuter, A. D. Wieck, and M. Bayer, "Collective single-mode precession of electron spins in an ensemble of singly charged (In,Ga)As/GaAs quantum dots," Phys. Rev. B **79**, 201305 (2009).

[Gre12]   A. Greilich, A. Pawlis, F. Liu, O. A. Yugov, D. R. Yakovlev, K. Lischka, Y. Yamamoto, and M. Bayer, "Spin dephasing of fluorine-bound electrons in ZnSe," Phys. Rev. B **85**, 121303 (2012).

[GT07]   N. Gisin and R. Thew, "Quantum communication," Nat. Photonics **1**, 165–171 (2007).

[GYB09]   A. Greilich, D. R. Yakovlev, and M. Bayer, "Optical tailoring of electron spin coherence in quantum dots," Solid State Commun. **149**, 1466–1471 (2009).

[Hah50]   E. L. Hahn, "Spin echoes," Phys. Rev. **80**, 580 (1950).

[Hal21]   B. Hall, A. Roggero, A. Baroni, and J. Carlson, "Simulation of collective neutrino oscillations on a quantum computer," Phys. Rev. D **104**, 063009 (2021).

[Har98]   S. Haroche, "Entanglement, decoherence and the quantum/classical boundary," Phys. Today **51**, 36–42 (1998).

[Hay12]   W. Haynes, ed., *CRC Handbook of chemistry and physics*, 93rd ed. (Taylor & Francis, Boca Raton, 2012).

[Heb17]   M. Hebenstreit, D. Alsina, J. I. Latorre, and B. Kraus, "Compressed quantum computation using a remote five-qubit quantum computer," Physical Review A **95**, 052339 (2017).

[Hei15]   F. Heisterkamp, E. A. Zhukov, A. Greilich, D. R. Yakovlev, V. L. Korenev, A. Pawlis, and M. Bayer, "Longitudinal and transverse spin dynamics of donor-bound electrons in fluorine-doped ZnSe: Spin inertia versus Hanle effect," Phys. Rev. B **91**, 235432 (2015).

[Hei16]   F. Heisterkamp, E. Kirstein, A. Greilich, E. A. Zhukov, T. Kazimierczuk, D. R. Yakovlev, A. Pawlis, and M. Bayer, "Dynamics of nuclear spin polarization induced and detected by coherently precessing electron spins in fluorine-doped ZnSe," Phys. Rev. B **93**, 081409 (2016).

[Her08]   F. G. G. Hernandez, A. Greilich, F. Brito, M. Wiemann, D. R. Yakovlev, D. Reuter, A. D. Wieck, and M. Bayer, "Temperature-induced spin-coherence dissipation in quantum dots," Phys. Rev. B **78**, 041303 (2008).

[HH10]   C.-W. Huang and X. Hu, "Theoretical study of nuclear spin polarization and depolarization in self-assembled quantum dots," Phys. Rev. B **81**, 205304 (2010).

[HO17]   J. Hübner and M. Oestreich, "Time-resolved spin dynamics and spin noise spectroscopy," in *Spin physics in semiconductors*, edited by M. I. Dyakonov, 2nd ed. (Springer International Publishing, Cham, 2017) Chap. 5, pp. 131–154.

[Hög12]   A. Högele, M. Kroner, C. Latta, M. Claassen, I. Carusotto, C. Bulutay, and A. Imamoglu, "Dynamic nuclear spin polarization in the resonant laser excitation of an InGaAs quantum dot," Phys. Rev. Lett. **108**, 197403 (2012).

[HW04]   H. Haken and H. C. Wolf, "Atome im Magnetfeld, Experimente und deren halbklassische Beschreibung," in *Atom- und Quantenphysik: Einführung in die experimentellen und theoretischen Grundlagen*, 8th ed. (Springer Berlin Heidelberg, Berlin, Heidelberg, 2004) Chap. 13, pp. 211–227.

[Ivc05]   E. L. Ivchenko, "Photoluminescence spectroscopy," in *Optical spectroscopy of semiconductor nanostructures* (Alpha Science, Harrow, 2005) Chap. 5, pp. 203–285.

[Jäs17]   N. Jäschke, A. Fischer, E. Evers, V. V. Belykh, A. Greilich, M. Bayer, and F. B. Anders, "Nonequilibrium nuclear spin distribution function in quantum dots subject to periodic pulses," Phys. Rev. B **96**, 205419 (2017).

[KA98]   J. M. Kikkawa and D. D. Awschalom, "Resonant spin amplification in n-type GaAs," Phys. Rev. Lett. **80**, 4313 (1998).

[Kal17]   V. K. Kalevich, K. V. Kavokin, I. Merkulov, and M. R. Vladimirova, "Dynamic nuclear polarization and nuclear fields," in *Spin physics in semiconductors*, edited by M. I. Dyakonov, 2nd ed. (Springer International Publishing, Cham, 2017) Chap. 12, pp. 387–430.

[Kap38]   P. Kapitza, "Viscosity of liquid helium below the λ-point," Nature **141**, 74 (1938).

[Kim08]   H. J. Kimble, "The quantum internet," Nature **453**, 1023–1030 (2008).

[Kle18]   I. Kleinjohann, E. Evers, P. Schering, A. Greilich, G. S. Uhrig, M. Bayer, and F. B. Anders, "Magnetic field dependence of the electron spin revival amplitude in periodically pulsed quantum dots," Phys. Rev. B **98**, 155318 (2018).

[KLG02]   A. V. Khaetskii, D. Loss, and L. Glazman, "Electron spin decoherence in quantum dots due to interaction with nuclei," Phys. Rev. Lett. **88**, 186802 (2002).

[Kli07]   C. F. Klingshirn, "Electrons in a periodic crystal," in *Semiconductor optics*, 3rd ed. (Springer, Berlin, Heidelberg, 2007) Chap. 8, pp. 163–242.

[KN01]   A. V. Khaetskii and Y. V. Nazarov, "Spin-flip transitions between Zeeman sublevels in semiconductor quantum dots," Phys. Rev. B **64**, 125316 (2001).

[Kop19]   N. E. Kopteva, I. A. Yugova, E. A. Zhukov, E. Kirstein, E. Evers, V. V. Belykh, V. L. Korenev, D. R. Yakovlev, M. Bayer, and A. Greilich, "Theoretical modeling of the nuclear-field induced tuning of the electron spin precession for localized spins," Phys. Status Solidi B **256**, 1800534 (2019).

[Kor11]   V. L. Korenev, "Multiple stable states of a periodically driven electron spin in a quantum dot using circularly polarized light," Phys. Rev. B **83**, 235429 (2011).

[Kou04]   A. V. Koudinov, I. A. Akimov, Y. G. Kusrayev, and F. Henneberger, "Optical and magnetic anisotropies of the hole states in Stranski-Krastanov quantum dots," Phys. Rev. B **70**, 241305 (2004).

[Kre10]   O. Krebs, P. Maletinsky, T. Amand, B. Urbaszek, A. Lemaître, P. Voisin, X. Marie, and A. Imamoglu, "Anomalous Hanle effect due to optically created transverse Overhauser field in single InAs/GaAs quantum dots," Phys. Rev. Lett. **104**, 056603 (2010).

[Krö56]   A. Krönig, "Grundzüge einer Theorie der Gase," Ann. Phys. **175**, 315–322 (1856).

[KRW04]   J. Kainz, U. Rössler, and R. Winkler, "Temperature dependence of Dyakonov-Perel spin relaxation in zinc-blende semiconductor quantum structures," Phys. Rev. B **70**, 195322 (2004).

[Kuh93]   B. Kuhn-Heinrich, W. Ossau, H. Heinke, F. Fischer, T. Litz, A. Waag, and G. Landwehr, "Optical investigation of confinement and strain effects in CdTe/(CdMg)Te quantum wells," Appl. Phys. Lett. **63**, 2932–2934 (1993).

[Lat09]   C. Latta, A. Högele, Y. Zhao, A. N. Vamivakas, P. Maletinsky, M. Kroner, J. Dreiser, I. Carusotto, A. Badolato, D. Schuh, W. Wegscheider, M. Atature, et al., "Confluence of resonant laser excitation and bidirectional quantum-dot nuclear-spin polarization," Nat. Phys. **5**, 758 (2009).

[Loo20]   P. van Loock, W. Alt, C. Becher, O. Benson, H. Boche, C. Deppe, J. Eschner, S. Höfling, D. Meschede, P. Michler, F. Schmidt, and H. Weinfurter, "Extending quantum links: Modules for fiber- and memory-based quantum repeaters," Adv. Quantum Technol. **3**, 1900141 (2020).

[Luo16]   D. Luong, L. Jiang, J. Kim, and N. Lütkenhaus, "Overcoming lossy channel bounds using a single quantum repeater node," Appl. Phys. B **122**, 96 (2016).

[Mad96]   O. Madelung, "Physical data," in *Semiconductors — Basic data*, edited by O. Madelung, 2nd ed. (Springer Berlin Heidelberg, Berlin, Heidelberg, 1996) Chap. 2, pp. 5–298.

[Mal07]   P. Maletinsky, C. W. Lai, A. Badolato, and A. Imamoglu, "Nonlinear dynamics of quantum dot nuclear spins," Phys. Rev. B **75**, 035409 (2007).

[MBI07]   P. Maletinsky, A. Badolato, and A. Imamoglu, "Dynamics of quantum dot nuclear spin polarization controlled by a single electron," Phys. Rev. Lett. **99**, 056804 (2007).

[MER02]   I. A. Merkulov, A. L. Efros, and M. Rosen, "Electron spin relaxation by nuclei in semiconductor quantum dots," Phys. Rev. B **65**, 205309 (2002).

[MI11]   K. Momma and F. Izumi, "VESTA3 for three-dimensional visualization of crystal, volumetric and morphology data," J. Appl. Crystallogr. **44**, 1272–1276 (2011).

[Moc17]   R. W. Mocek, V. L. Korenev, M. Bayer, M. Kotur, R. I. Dzhioev, D. O. Tolmachev, G. Cascio, K. V. Kavokin, and D. Suter, "High-efficiency optical pumping of nuclear polarization in a GaAs quantum well," Phys. Rev. B **96**, 201303 (2017).

[Mor19]   O. Morin, M. Körber, S. Langenfeld, and G. Rempe, "Deterministic shaping and reshaping of single-photon temporal wave functions," Phys. Rev. Lett. **123**, 133602 (2019).

[Neu17]   F. Neukart, G. Compostella, C. Seidel, D. von Dollen, S. Yarkoni, and B. Parney, "Traffic flow optimization using a quantum annealer," Front. ICT **4**, 29 (2017).

[Ngu19]   C. T. Nguyen, D. D. Sukachev, M. K. Bhaskar, B. Machielse, D. S. Levonian, E. N. Knall, P. Stroganov, R. Riedinger, H. Park, M. Lončar, and M. D. Lukin, "Quantum network nodes based on diamond qubits with an efficient nanophotonic interface," Phys. Rev. Lett. **123**, 183602 (2019).

[Onu16]   A. R. Onur, J. P. de Jong, D. O'Shea, D. Reuter, A. D. Wieck, and C. H. van der Wal, "Stabilizing nuclear spins around semiconductor electrons via the interplay of optical coherent population trapping and dynamic nuclear polarization," Phys. Rev. B **93**, 161204 (2016).

[OW18]   A. R. Onur and C. H. van der Wal, "Two-laser dynamic nuclear polarization with semiconductor electrons: Feedback, suppressed fluctuations, and bistability near two-photon resonance," Phys. Rev. B **98**, 165304 (2018).

[PAK08]   D. Paget, T. Amand, and J.-P. Korb, "Light-induced nuclear quadrupolar relaxation in semiconductors," Phys. Rev. B **77**, 245201 (2008).

[Pau25]   W. Pauli, "Über den Zusammenhang des Abschlusses der Elektronengruppen im Atom mit der Komplexstruktur der Spektren," Z. Physik **31**, 765–783 (1925).

[Pet08] M. Y. Petrov, I. V. Ignatiev, S. V. Poltavtsev, A. Greilich, A. Bauschulte, D. R. Yakovlev, and M. Bayer, "Effect of thermal annealing on the hyperfine interaction in InAs/GaAs quantum dots," Phys. Rev. B **78**, 045315 (2008).

[Pro21] M. Proietti, J. Ho, F. Grasselli, P. Barrow, M. Malik, and A. Fedrizzi, "Experimental quantum conference key agreement," Sci. Adv. **7**, eabe0395 (2021).

[Rab37] I. I. Rabi, "Space quantization in a gyrating magnetic field," Phys. Rev. **51**, 652 (1937).

[Ram50] N. F. Ramsey, "A molecular beam resonance method with separated oscillating fields," Phys. Rev. **78**, 695 (1950).

[Rei10] D. J. Reilly, J. M. Taylor, J. R. Petta, C. M. Marcus, M. P. Hanson, and A. C. Gossard, "Exchange control of nuclear spin diffusion in a double quantum dot," Phys. Rev. Lett. **104**, 236802 (2010).

[RLZ59] L. M. Roth, B. Lax, and S. Zwerdling, "Theory of optical magneto-absorption effects in semiconductors," Phys. Rev. **114**, 90 (1959).

[Roz19] F. Rozpędek, R. Yehia, K. Goodenough, M. Ruf, P. C. Humphreys, R. Hanson, S. Wehner, and D. Elkouss, "Near-term quantum-repeater experiments with nitrogen-vacancy centers: Overcoming the limitations of direct transmission," Phys. Rev. A **99**, 052330 (2019).

[RRS54] I. I. Rabi, N. F. Ramsey, and J. Schwinger, "Use of rotating coordinates in magnetic resonance problems," Rev. Mod. Phys. **26**, 167 (1954).

[San06] H. Sanada, Y. Kondo, S. Matsuzaka, K. Morita, C. Y. Hu, Y. Ohno, and H. Ohno, "Optical pump-probe measurements of local nuclear spin coherence in semiconductor quantum wells," Phys. Rev. Lett. **96**, 067602 (2006).

[San11] N. Sangouard, C. Simon, H. de Riedmatten, and N. Gisin, "Quantum repeaters based on atomic ensembles and linear optics," Rev. Mod. Phys. **83**, 33–80 (2011).

[Sca09] V. Scarani, H. Bechmann-Pasquinucci, N. J. Cerf, M. Dušek, N. Lütkenhaus, and M. Peev, "The security of practical quantum key distribution," Rev. Mod. Phys. **81**, 1301–1350 (2009).

[Sch21] P. Schering, E. Evers, V. Nedelea, D. S. Smirnov, E. A. Zhukov, D. R. Yakovlev, M. Bayer, G. S. Uhrig, and A. Greilich, "Resonant spin amplification in Faraday geometry," Phys. Rev. B **103**, L201301 (2021).

[Sch35] E. Schrödinger, "Die gegenwärtige Situation in der Quantenmechanik," Naturwissenschaften **23**, 807–812 (1935).

[SGR20] M. A. Semina, A. A. Golovatenko, and A. V. Rodina, "Electron, hole and exciton effective g-factors in semiconductor nanocrystals," Preprint available at arXiv:2011.11041 [cond-mat.mes-hall] (2020).

[Sha03]   A. Shabaev, A. L. Efros, D. Gammon, and I. A. Merkulov, "Optical readout and initialization of an electron spin in a single quantum dot," Phys. Rev. B **68**, 201305 (2003).

[Shi07]   A. J. Shields, "Semiconductor quantum light sources," Nat. Photonics **1**, 215–235 (2007).

[Sir97]   A. A. Sirenko, T. Ruf, M. Cardona, D. R. Yakovlev, W. Ossau, A. Waag, and G. Landwehr, "Electron and hole g factors measured by spin-flip Raman scattering in $CdTe/Cd_{1-x}Mg_xTe$ single quantum wells," Phys. Rev. B **56**, 2114–2119 (1997).

[SK03]   Y. G. Semenov and K. W. Kim, "Effect of an external magnetic field on electron-spin dephasing induced by hyperfine interaction in quantum dots," Phys. Rev. B **67**, 073301 (2003).

[Spa11]   S. Spatzek, A. Greilich, S. E. Economou, S. Varwig, A. Schwan, D. R. Yakovlev, D. Reuter, A. D. Wieck, T. L. Reinecke, and M. Bayer, "Optical control of coherent interactions between electron spins in InGaAs quantum dots," Phys. Rev. Lett. **107**, 137402 (2011).

[SPH61]   P. L. Sagalyn, A. Paskin, and R. J. Harrison, "Contribution of strain to nuclear quadrupole interactions in dilute alloys of copper," Phys. Rev. **124**, 428–437 (1961).

[SRU14]   D. Stanek, C. Raas, and G. S. Uhrig, "From quantum-mechanical to classical dynamics in the central-spin model," Phys. Rev. B **90**, 064301 (2014).

[SUS19]   P. Schering, G. S. Uhrig, and D. S. Smirnov, "Spin inertia and polarization recovery in quantum dots: Role of pumping strength and resonant spin amplification," Phys. Rev. Research **1**, 033189 (2019).

[Syp11]   M. Syperek, D. R. Yakovlev, I. A. Yugova, J. Misiewicz, I. V. Sedova, S. V. Sorokin, A. A. Toropov, S. V. Ivanov, and M. Bayer, "Long-lived electron spin coherence in CdSe/Zn(S,Se) self-assembled quantum dots," Phys. Rev. B **84**, 085304 (2011); "Erratum: Long-lived electron spin coherence in CdSe/Zn(S,Se) self-assembled quantum dots," Phys. Rev. B **84**, 159903 (2011).

[Tar84]   S. Tarucha, H. Okamoto, Y. Iwasa, and N. Miura, "Exciton binding energy in GaAs quantum wells deduced from magneto-optical absorption measurement," Solid State Commun. **52**, 815–819 (1984).

[Tes09]   C. Testelin, F. Bernardot, B. Eble, and M. Chamarro, "Hole-spin dephasing time associated with hyperfine interaction in quantum dots," Phys. Rev. B **79**, 195440 (2009).

[UG25]   G. E. Uhlenbeck and S. Goudsmit, "Ersetzung der Hypothese vom unmechanischen Zwang durch eine Forderung bezüglich des inneren Verhaltens jedes einzelnen Elektrons," Naturwissenschaften **13**, 953–954 (1925).

[Urb07]   B. Urbaszek, P.-F. Braun, T. Amand, O. Krebs, T. Belhadj, A. Lemaítre, P. Voisin, and X. Marie, "Efficient dynamical nuclear polarization in quantum dots: Temperature dependence," Phys. Rev. B **76**, 201301 (2007).

[Urb13]   B. Urbaszek, X. Marie, T. Amand, O. Krebs, P. Voisin, P. Maletinsky, A. Högele, and A. Imamoglu, "Nuclear spin physics in quantum dots: An optical investigation," Rev. Mod. Phys. **85**, 79 (2013).

[Var14a]   S. Varwig, A. Greilich, D. R. Yakovlev, and M. Bayer, "Spin mode locking in quantum dots revisited," Phys. Status Solidi B **251**, 1892 (2014).

[Var14b]   S. Varwig, "Optical electron spin tomography and hole spin coherence studies in (In,Ga)As/GaAs quantum dots," PhD thesis (TU Dortmund University, 2014) Chap. 2.

[Waa93]   A. Waag, H. Heinke, S. Scholl, C. Becker, and G. Landwehr, "Growth of MgTe and $Cd_{1-x}Mg_x$Te thin films by molecular beam epitaxy," J. Cryst. Growth **131**, 607–611 (1993).

[Wae19]   A. Waeber, G. Gillard, G. Ragunathan, M. Hopkinson, P. Spencer, D. A. Ritchie, M. S. Skolnick, and E. A. Chekhovich, "Pulse control protocols for preserving coherence in dipolar-coupled nuclear spin baths," Nat. Commun. **10**, 3157 (2019).

[War13]   R. J. Warburton, "Single spins in self-assembled quantum dots," Nat. Mater. **12**, 483 (2013).

[WEH18]   S. Wehner, D. Elkouss, and R. Hanson, "Quantum internet: A vision for the road ahead," Science **362**, eaam9288 (2018).

[Wüs16]   G. Wüst, M. Munsch, F. Maier, A. V. Kuhlmann, A. Ludwig, A. D. Wieck, D. Loss, M. Poggio, and R. J. Warburton, "Role of the electron spin in determining the coherence of the nuclear spins in a quantum dot," Nat. Nanotechnol. **11**, 885 (2016).

[Wyc63]   R. W. G. Wyckoff, "Structures of the compounds rx," in *Crystal structures*, 2nd ed. (Interscience Publishers, Berlin, Heidelberg, 1963) Chap. 3, pp. 85–237.

[WZ82]   W. K. Wootters and W. H. Zurek, "A single quantum cannot be cloned," Nature **299**, 802–803 (1982).

[Xu08]   X. Xu, B. Sun, P. R. Berman, D. G. Steel, A. S. Bracker, D. Gammon, and L. J. Sham, "Coherent population trapping of an electron spin in a single negatively charged quantum dot," Nat. Phys. **4**, 692–695 (2008).

[Xu09]   X. Xu, W. Yao, B. Sun, D. G. Steel, A. S. Bracker, D. Gammon, and L. J. Sham, "Optically controlled locking of the nuclear field via coherent dark-state spectroscopy," Nature **459**, 1105–1109 (2009).

[Yaf63]   Y. Yafet, "*g* factors and spin-lattice relaxation of conduction electrons," in *Solid state physics*, Vol. 14, edited by F. Seitz and D. Turnbull, Solid State Physics (Academic Press, 1963), pp. 1–98.

[YB17]   D. R. Yakovlev and M. Bayer, "Coherent spin dynamics of carriers," in *Spin physics in semiconductors*, edited by M. I. Dyakonov, 2nd ed. (Springer International Publishing, Cham, 2017) Chap. 6, pp. 155–206.

[YFI10]   S. T. Yılmaz, P. Fallahi, and A. Imamoğlu, "Quantum-dot-spin single-photon interface," Phys. Rev. Lett. **105**, 033601 (2010).

[Yug07]   I. A. Yugova, A. Greilich, E. A. Zhukov, D. R. Yakovlev, M. Bayer, D. Reuter, and A. D. Wieck, "Exciton fine structure in InGaAs/GaAs quantum dots revisited by pump-probe Faraday rotation," Phys. Rev. B **75**, 195325 (2007).

[Yug09]   I. A. Yugova, M. M. Glazov, E. L. Ivchenko, and A. L. Efros, "Pump-probe Faraday rotation and ellipticity in an ensemble of singly charged quantum dots," Phys. Rev. B **80**, 104436 (2009).

[Yug12]   I. A. Yugova, M. M. Glazov, D. R. Yakovlev, A. A. Sokolova, and M. Bayer, "Coherent spin dynamics of electrons and holes in semiconductor quantum wells and quantum dots under periodical optical excitation: Resonant spin amplification versus spin mode locking," Phys. Rev. B **85**, 125304 (2012).

[Zee97]   P. Zeeman, "The effect of magnetisation on the nature of light emitted by a substance," Nature **55**, 347 (1897).

[Zho15]   M. Zhong, M. P. Hedges, R. L. Ahlefeldt, J. G. Bartholomew, S. E. Beavan, S. M. Wittig, J. J. Longdell, and M. J. Sellars, "Optically addressable nuclear spins in a solid with a six-hour coherence time," Nature **517**, 177–180 (2015).

[Zhu06]   E. A. Zhukov, D. R. Yakovlev, M. Bayer, G. Karczewski, T. Wojtowicz, and J. Kossut, "Spin coherence of two-dimensional electron gas in CdTe/(Cd,Mg)Te quantum wells," Phys. Status Solidi B **243**, 878 (2006).

[Zhu07]   E. A. Zhukov, D. R. Yakovlev, M. Bayer, M. M. Glazov, E. L. Ivchenko, G. Karczewski, T. Wojtowicz, and J. Kossut, "Spin coherence of a two-dimensional electron gas induced by resonant excitation of trions and excitons in CdTe/(Cd,Mg)Te quantum wells," Phys. Rev. B **76**, 205310 (2007).

[Zhu09]   E. A. Zhukov, D. R. Yakovlev, M. Gerbracht, G. V. Mikhailov, G. Karczewski, T. Wojtowicz, J. Kossut, and M. Bayer, "Spin coherence of holes and electrons in undoped CdTe/(Cd,Mg)Te quantum wells," Phys. Rev. B **79**, 155318 (2009).

[Zhu10]   E. A. Zhukov, D. R. Yakovlev, M. M. Glazov, L. Fokina, G. Karczewski, T. Wojtowicz, J. Kossut, and M. Bayer, "Optical control of electron spin coherence in CdTe/(Cd,Mg)Te quantum wells," Phys. Rev. B **81**, 235320 (2010).

[Zhu12]   E. A. Zhukov, O. A. Yugov, I. A. Yugova, D. R. Yakovlev, G. Karczewski, T. Wojtowicz, J. Kossut, and M. Bayer, "Resonant spin amplification of resident electrons in CdTe/(Cd,Mg)Te quantum wells subject to tilted magnetic fields," Phys. Rev. B **86**, 245314 (2012).

[Zhu18a]   E. A. Zhukov, E. Kirstein, N. E. Kopteva, F. Heisterkamp, I. A. Yugova, V. L. Korenev, D. R. Yakovlev, A. Pawlis, M. Bayer, and A. Greilich, "Discretization of the total magnetic field by the nuclear spin bath in fluorine-doped ZnSe," Nat. Commun. **9**, 1941 (2018).

[Zhu18b]   E. A. Zhukov, E. Kirstein, D. S. Smirnov, D. R. Yakovlev, M. M. Glazov, D. Reuter, A. D. Wieck, M. Bayer, and A. Greilich, "Spin inertia of resident and photoexcited carriers in singly charged quantum dots," Phys. Rev. B **98**, 121304 (2018).

[Zur03]   W. H. Zurek, "Decoherence, einselection, and the quantum origins of the classical," Rev. Mod. Phys. **75**, 715 (2003).

Publications

1. V. V. Belykh, E. Evers, D. R. Yakovlev, F. Fobbe, A. Greilich, and M. Bayer, "Extended pump-probe Faraday rotation spectroscopy of the submicrosecond electron spin dynamics in n-type GaAs," Phys. Rev. B **94**, 241202 (2016).

2. S. Varwig, E. Evers, A. Greilich, D. R. Yakovlev, D. Reuter, A. D. Wieck, T. Meier, A. Zrenner, and M. Bayer, "Advanced optical manipulation of carrier spins in (In,Ga)As quantum dots," Appl. Phys. B **122**, 17 (2016).

3. D. V. Azamat, V. V. Belykh, D. R. Yakovlev, F. Fobbe, D. H. Feng, E. Evers, L. Jastrabik, A. Dejneka, and M. Bayer, "Electron spin dynamics of Ce^{3+} ions in YAG crystals studied by pulse-EPR and pump-probe Faraday rotation," Phys. Rev. B **96**, 075160 (2017).

4. N. Jäschke, A. Fischer, E. Evers, V. V. Belykh, A. Greilich, M. Bayer, and F. B. Anders, "Nonequilibrium nuclear spin distribution function in quantum dots subject to periodic pulses," Phys. Rev. B **96**, 205419 (2017).

5. E. Evers, V. V. Belykh, N. E. Kopteva, I. A. Yugova, A. Greilich, D. R. Yakovlev, D. Reuter, A. D. Wieck, and M. Bayer, "Decay and revival of electron spin polarization in an ensemble of (In,Ga)As quantum dots," Phys. Rev. B **98**, 075309 (2018).

6. I. Kleinjohann, E. Evers, P. Schering, A. Greilich, G. S. Uhrig, M. Bayer, and F. B. Anders, "Magnetic field dependence of the electron spin revival amplitude in periodically pulsed quantum dots," Phys. Rev. B **98**, 155318 (2018).

7. A. Fischer, E. Evers, S. Varwig, A. Greilich, M. Bayer, and F. B. Anders, "Signatures of long-range spin-spin interactions in an (In,Ga)As quantum dot ensemble," Phys. Rev. B **98**, 205308 (2018).

8. E. Evers, T. Kazimierczuk, F. Mertens, D. R. Yakovlev, G. Karczewski, T. Wojtowicz, J. Kossut, M. Bayer, and A. Greilich, "Nuclear spin dynamics influenced and detected by electron spin polarization in CdTe/(Cd,Mg)Te quantum wells," Phys. Rev. B **99**, 045303 (2019).

9. N. E. Kopteva, I. A. Yugova, E. A. Zhukov, E. Kirstein, E. Evers, V. V. Belykh, V. L. Korenev, D. R. Yakovlev, M. Bayer, and A. Greilich, "Theoretical modeling of the nuclear-field induced tuning of the electron spin precession for localized spins," Phys. Status Solidi B **256**, 1800534 (2019).

10. E. Evers, N. E. Kopteva, I. A. Yugova, D. R. Yakovlev, D. Reuter, A. D. Wieck, M. Bayer, and A. Greilich, "Suppression of nuclear spin fluctuations in an InGaAs quantum dot ensemble by GHz-pulsed optical excitation," npj Quantum Inf. **7**, 60 (2021).

11. P. Schering, E. Evers, V. Nedelea, D. S. Smirnov, E. A. Zhukov, D. R. Yakovlev, M. Bayer, G. S. Uhrig, and A. Greilich, "Resonant spin amplification in Faraday geometry," Phys. Rev. B **103**, L201301 (2021).

12. E. Evers, N. E. Kopteva, I. A. Yugova, D. R. Yakovlev, M. Bayer, and A. Greilich, "Shielding of external magnetic field by dynamic nuclear polarization in (In,Ga)As quantum dots," Phys. Rev. B **104**, 075302 (2021).

13. E. Kirstein, D. R. Yakovlev, M. M. Glazov, E. Evers, E. A. Zhukov, V. V. Belykh, N. E. Kopteva, D. Kudlacik, O. Nazarenko, D. N. Dirin, M. V. Kovalenko, and M. Bayer, "Lead-dominated hyperfine interaction impacting the carrier spin dynamics in halide perovskites," Adv. Mater., 2105263 (2021).

Acknowledgments